UNIVERSITY OF RWTH AACHEN

Faculty of Mechanical Engineering

Shock Wave Laboratory

Bachelor Thesis

RECOVERY SYSTEM DESIGN FOR LOWER STAGES OF ROCKETS

Author: David Soriano Pascual

Degree: Aerospace Engineering

Tutor: Prof. Herbert Olivier

Aachen, September 2017

Contents

Index of Tables VI

Nomenclature VII

CHAPTER 1. Introduction

1.1. Abstract 1

1.2. Brief historical review of parachutes 1

CHAPTER 2. Units, mathematical models and important parameters

2.1. Units of measurement 3

2.1.1. Basic units 3

2.1.2. Derived units 3

2.1.2. Conversion to English units 3

2.2. Earth's atmosphere 4

2.2. Important parameters 5

CHAPTER 3. Parachute recovery system and general considerations

3.1. Parachute system boundaries 7

3.2. Parachute design considerations 8

3.3. Parachute structural analyses 9

3.3.1. Basic description of High-performance Parachutes 9

3.3.2. Parachute Deployment 11

3.3.3. Pilot Chutes 13

3.3.4. Parachute Stress Analysis 14

3.3.5. Textile Materials 14

3.3.6. Parachute Recovery System Weight and Volume 15

3.4. Parachute aerodynamic analyses 18

3.4.1. Stability of parachute systems 18

3.4.2. Parachute inflation process 20

3.4.3. Altitude effects 27

3.4.4. Porosity effects 28

3.4.5. Canopy shape and pressure distribution 29

3.5. Clustering of parachutes 30

3.5.1. Loss of Drag in Cluster Applications 30

3.5.2. Synchronization problems 31

3.6. Supersonic parachutes 32
CHAPTER 4: Application. Parachute design for the recovery of a rocket's first-stage
4.1. Ares I-X: Overview and General data 35
4.1.1. Flight Performance 36
4.2. Parachute Recovery System Design 41
4.2.1. Main Parachute System Design 41
4.2.2. Drogue Chute Design 50
CHAPTER 5: Impact Attenuation System. General Design Considerations
5.1. Landing Analysis 53
5.1.1. Crushable Impact Attenuators: 54
5.1.2. Air Bags 55
5.1.3. Retrorocket Landing Attenuation System 56
5.2. Airbag Impact Dynamics Modelling 56
5.2.1. Thermodynamics Analysis 57
5.2.2. System Dynamics Equation 60
5.2.3. Shape Function Equations 61
5.2.4. Gas Dynamics Equation 62
5.2.5. Orifice Flow Equations 63
5.2.6. The Integrated Single Airbag Impact Model 66
CHAPTER 6: Application: Airbag design for the recovery of a rocket's first-stage
6.1. Airbag Sizing 69
6.2. Airbag performance 70
CHAPTER 7. Conclusions 77
Appendix A 78
Appendix B 87
References 88

Index of figures

Figure 3.1. Parachute Performance Envelopes.

Figure 3.2. Principal Components of a Parachute.

Figure 3.3 Geometric Parameters of a Parachute.

Figure 3.4. Uncontrolled Deployment.

Figure 3.5. Pilot Chute Deployment.

Figure 3.6. Parachute Static-Line Deployment.

Figure 3.7. Controlled Parachute Deployment Concpet.

Figure 3.8. Parachute Recovery System Weight as Percentage of Air Vehicle Weight.

Figure 3.9. Parachute Weight vs NP_sD_0.

Figure 3.10. Static Stability of Different Parachute Types.

Figure 3.11. Relationship of Ariflow and Stability depending on Porosity.

Figure 3.12. Parachute Canopy Inflation Process.

Figure 3.13. Filling Distance of a Parachute Canopy.

Figure 3.14. Typical Drag-Area-Versus-Time Increase for Various Parachute Types.

Figure 3.15. Typical Drag-Area-Versus-Time Increase for Reefed Parachutes.

Figure 3.16. Force-versus-Time Diagrams for Infinite and Finite Mass Conditions.

Figure 3.18. Parachute Opening Forces as Function of Altitude for Various Types of Parachutes.

Figure 3.19. Drag Coefficient and Oscillation as a function of Total Porosity for 3.5 foot-diameter Flat and Conical Ribbon Parachutes.

Figure 3.20. Parachute Canopies with Constant Suspension-line Ratio and Porosities from 15 to 30%.

Figure 3.21. Parachute with Constant Porosity and Suspension line ratios of 1.0, 1.5 and 2.0.

Figure 3.22. Airflow and pressure distribution around a parachute canopy.

Figure 3.23. Typical Parachute Cluster Arrangement.

Figure 3.24. Drag Loss in Parachute Clusters.

Figure 3.25. Supersonic Flow around a Vehicle-Parachute System.

Figure 3.26. Instability at Mach 2.0, 2.2 and 2.5 for a 26-ft-Disk-Gap-Band Parachute.

Figure 3.27. Progression of Fluid Interaction of a Disk-Gap-Band Parachute.

Figure 3.28. Drag Coefficient of several Parachutes as Function of Mach Number.

Figure 4.1. Elements of Ares I Rocket.

Figure 4.2. Recovery Trajectory of the First Stage.

Figure 4.3. Altitude vs Velocity curve of Ares I-X performance data from Table 4.2.

Figure 4.4. Dynamic Pressure vs Time curve of performance data from Table 4.2.

Figure 4.5. Velocity vs Time curve of Ares I-X performance data from Table 4.2.

Figure 4.6. Enlargement of Altitude vs Velocity curve of Ares I-X performance.

Figure 4.7. Typical Drag Coefficient versus Nominal Diameter for different Sizes of Ringsail Parachutes.

Figure 4.8. Drag loss in Parachute Clusters.

Figure 4.9. Variation of Drag Coefficient with Suspension Line Ratio.

Figure 4.10. Altitude vs Velocity of the Main Parachutes.

Figure 4.11. Inflation Sequence profile for a 72.8 ft-diameter Parachtue.

Figure 4.12. Opening-Force reduction factor versus Ballistic Parameter.

Figure 4.13. Sequence of images of the deployment of the main parachutes of the first stage of the Ares I-X.

Figure 4.14. Canopy Weight versus Nominal Diameter for different sizes Ringsail Parachutes.

Figure 5.1. Deceleration Stroke vs Rate of Descent and Allowable Impact Deceleration.

Figure 5.2. Typical Honeycomb Structure.

Figure 5.3. Airbag Pressure vs Stroke Characteristics.

Figure 5.4. Initial Condition for Thermodynamic Analysis.

Figure 5.5. System State Transition between Initial Contact weight the Surface and Maximum Airbag Compression.

Figure 5.6. System during the Venting Phase.

Figure 5.7. Single Airbag Impact Model Initial Condition.

Figure 5.8. Shape Function used in Single Airbag Impact Model.

Figure 5.9. Definition of Upstream and Downstream Pressure as used by the Single Airbag Impact Model.

Figure 5.10. Data used to model the Discharge Coefficient within the Single Airbag Impact Model.

Figure 5.11. Single Airbag Impact Model Functional Flow Block Diagram.

Figure 6.1. Orion CEV Airbag System Design.

Figure 6.2. Proposal of simplified Airbag System Design.

Figure 6.3. Airbag cross-sectional Sketch at time t and time t+1.

Figure 6.4. Airbag Pressure vs effective Stroke.

Figure 6.5. Airbag Pressure vs Time.

Figure 6.6. Enlargement Airbag Pressure vs Time.

Figure 6.7. Air Mass within the Airbag vs Time.

Index of Tables

Table 2.1. Basic Units.

Table 2.2. Derived Units.

Table 2.3. Conversion to English units.

Table 2.4. Examples of Reynolds numbers for different air vehicles.

Table 3.1. Parachute Design Criteria.

Table 3.2. Comparative Rating of Performance Characteristics for Various Parachute Systems Applications.

Table 3.3. Pilot Chute Drag and Opening-Force Coefficients.

Table 4.1. Dimensions and Mass properties.

Table 4.2. Events based on predicted Nominal Performance, unless otherwise noted.

Table 5.1. Allowable Impact Decelerations.

Table 6.1. Values assumed for the Thermodynamics Analysis.

Nomenclature

m_{FS}	First Stage Mass.
p_0	Atmospheric Pressure.
ρ_0	Atmospheric Density.
T_0	Atmospheric Temperature.
a_0	Speed of Sound at Standard Conditions.
μ_0	Viscosity of Air at Standard Conditions.
g_0	Gravitational Acceleration at Sea level
C_D	Drag Coefficient.
c_S	Speed of Sound
R_m	Mass Ratio
W_P	Weight of the Parachute.
D_v	Vent Diameter.
D_p	Projected Diameter.
D_0	Nominal Diameter.
S_0	Nominal Surface.
D_c	Constructed Diameter.
l_e	Suspension Line Length.
w_c	Specific Canopy Weight.
N_G	Number of Radials in the Canopy.
w_{RT}	Specific Weight of the radial Tape.
F_{RT}	Strength of the radial Tape.
N_{SL}	Number of Suspension Lines.
w_{SL}	Specific Weight of Suspension Lines.
F_{SL}	Strength of Suspension Lines.
P_s	Rated ultimate Strength of Suspension Lines.
M_G	Pitch Moment.
C_m	Pitch Coefficient.
s_f	Filling Distance.
t_f	Filling Time.
F_X	Peak Opening Force.
F_S	Snatch Force.
F_C	Steady-state Force.
C_X	Opening Force Coefficient.
X_1	Opening Force Reduction Factor.
q_e	Equilibrium Dynamic Pressure.
D_{FB}	Drag Force of the Forebody.
C_f	Friction Coefficient.
SF	Shape Factor.
S_{wet}	Wet Surface.
A_{FP}	Footprint Area.
$L_{A_{FP}}$	Footprint Area Length.
A_{Xs}	Cross Section Area.
A_{th}	Orifice Area.
Cd	Discharge Coefficient.

Roman Symbols

z, h	Altitude.
p	Pressure.
g	Gravitational Acceleration.
T	Temperature.
v, u	Velocity
m	Mass.
l	Length.
D	Diameter.
M	Mach Number
Re	Reynolds Number
Fr	Froude Number
W	Weight.
V	Volume.
S	Surface.
q	Dynamic Pressure.
F	Force.
t	Time.
A	Ballistic Parameter.
E	Energy.
PE	Potential Energy.
KE	Kinetic Energy
U	Internal Energy.
$\ddot{x}$	Acceleration.

Greek Symbols

δ	Relative Pressure.
σ	Relative Density.
θ	Relative Temperature.
μ	Dynamic Viscosity.
ρ	Density.
π	Pi Number.
α	Angle of Attack.
λ_T	Total Canopy Porosity.
γ	Coefficient of adiabatic Dilatation.

CHAPTER 1. Introduction

1.1. Abstract

The only way that mankind has to explore the space is with the use of space launch vehicles, commonly known as rockets. Although the first space flight took place more than fifty years ago and despite the great technological advances achieved, this field of the Aerospace Industry has developed very slowly due mainly to an economic matter. It turns out that the construction of rockets is too expensive to use a rocket once. That is why the reuse of the rocket or part of it has become one of the major concerns to allow the future advancement of Space Transport Systems as it ensures to save production costs. This reuse is possible with the integration of Recovery Systems in the rockets.

Among the various methods that have been investigated for rocket recovery, in this project we will focus on the most used, which are the parachute system and the airbag system. In the recovery process, the parachutes are the first to be used to decelerate the vehicle in its final descent, and then the airbag is used to attenuate the impact with the surface.

The main objective of this study is to find an appropriate design of a parachute system as well as to propose the design of an airbag system for allowing the recovery of the lower stages of a rocket. In order to do this, we will study the main concepts of both recovery subsystems, such as their structure and performance and what methods are used to make a preliminary design. With this we will be able to apply a design proposal for a real rocket case, from which we will be able to verify if the estimated values are adjusted to the reality and therefore if the methods used are consistent.

1.2. Brief historical review of parachutes

Etymologically, the word *parachute* is derived from the French words *parare* (meaning to protect), and *chute* (meaning fall). Therefore the word parachute refers to "any device capable of controlling a free fall and thereby sustaining or supporting a certain charge in the air".

In the field of engineering a parachute is considered as a type of aerodynamic decelerator that uses the drag force that generates to decelerate people or equipment from a high speed until a low speed and until a safe landing.

There is evidence of devices similar to parachutes found in China that dates back to the 12^{th} Century, in addition to some sketches by Leonardo da Vinci in 1514. However, the first authenticated parachute descent was executed in October 1797 when André-Jacques Ganerin jumped from a balloon in Paris.

At the beginning of the 19th Century the first applications of the parachutes were simple spectacles of entertainment of specialists who exhibited their descents, until in 1808 a parachute served to save a human life.

Thus, at the outbreak of World War I they already used cotton parachutes to save the observers whose hydrogen balloons were exploited.

With the entry into use of aircrafts, new techniques were developed to improve the parachutes systems, such as the packaging technique, the extraction technique or the materials of such parachutes.

After the outbreak of World War II there was already considerable experience in the use of the parachute, used in roles as decelerator of aircrafts, falling of supplies or stabilization of war loads.

When the war was over, Parachute Research Centres were established and many types of parachute designs appeared, depending on the different characteristics required. Some of these designs were the ribbon parachute (1930), the gliding parachute (1961), or spacecraft parachutes.

Ultimately for many years it was enough to rely on test data to build the base of the experience needed to reach the development of the technology of today's high performance parachute systems.

Until then the development of parachutes was evolving in small steps, but finally the technology of the parachutes was forced to advance much faster by various factors. Of great importance was the specification of much more restrictive parachute performance requirements needed for the flight of missiles, rockets, re-entry vehicles and spacecraft. These requirements were made possible by the development of electronics, computers and material science. At the same time, the payloads became much more expensive and because of that the recovery became an important objective.

However in contrast, the costs of flight tests increased by more than one order of magnitude, rendering the "design per test" method of a parachute unavailable. These restrictions forced the consideration of an alternative for the development of parachute technology, focused on modelling the complex aerodynamic behaviour of parachute inflation.

New design tools were developed to learn more about how parachutes interact with the air around them and although much has been learned, it has to be recognized that it is still possible to learn much more to design today's high performance parachutes.

CHAPTER 2. Units, mathematical models and important parameters

This chapter introduces some of the most basic aspects that will be used throughout this project. It includes units of measurement in both the international system and their conversions to English units of measurement, also used in engineering. In addition the standard atmosphere model and certain parameters of great relevance will be presented.

2.1. Units of measurement

2.1.1. Basic units

Units	Metric		English	
Quantity	Symbol	Name	Symbol	Name
Length	m	meter	ft or in	foot or inch
Mass	kg	kilogram	lb	pound
Time	s	second	s	second
Temperature	K	Kelvin	R	Rankine

Table 2.1. Basic Units.

2.1.2. Derived units

Units	Metric			English		
Quantity	Symbol	Name	Dimension	Symbol	Name	Dimension
Force	N	newton	$kg{\cdot}m/s^2$	lbf	pound force	$lb{\cdot}ft/s^2$
Pressure	Pa	pascal	N/m^2	psi or lb/ft	pound per square inch or pound per square foot	lb/in^2 or lb/ft^2
Work, energy	J	joule	N·m	ft-lb	foot-pound	N·m
Rate of energy	W	watt	J/s	HP or ft-lb/s	horsepower or foot-pounds per second	ft-lb/s

Table 2.2. Derived Units.

2.1.2. Conversion to English units

Quantity	Metric	English
Length	1 m	3.28 ft
Weight	1 kg	2.2 lb
Force	1 N	0.225 lbf
Pressure	1 kPa	0.145 psi
Power	1 kW	737.56 ft-lb/s or 1.34 HP
Temperature	1 ^oK	1.8 ^oR
Velocity	1 m/s	3.28 ft/s

Table 2.3. Conversion to English units.

2.2. Earth's atmosphere

Atmospheric characteristics such as temperature, pressure, density, air speed and humidity actually vary in a seemingly random way according to different time and space scales. For aerospace applications a statistic of these variations is used, based on meteorological data collected over many years.

In almost all atmospheric models the temperature distribution is specified in terms of segments of a defined and fixed variation of the temperature with altitude. These mathematical models don't search a detailed representation of reality (impossible thing), they are able to establish comparisons between different aircraft models.

Once the temperature gradient value has been defined constant with the altitude for each segment of the atmosphere $(\partial T(z)/\partial z = \beta)$, pressure and density can be deduced by assuming that the air behaves as an ideal gas.

The mathematical model employed in this case is the *International Standard Atmosphere* or *ISA* [1]:

Standard conditions at sea level

$$p_0 = 101325\,Pa \;\rightarrow\; Relative\ Pressure: \delta(z) = p(z)/p_0 \tag{2.1}$$

$$\rho_0 = 1.225\frac{kg}{m^3} \rightarrow\; Relative\ Density: \sigma(z) = \rho(z)/\rho_0 \tag{2.2}$$

$$T_0 = 288.15\,K \;\rightarrow\; Relative\ Temperature: \theta(z) = T(z)/T_0 \tag{2.3}$$

$$a_0 = 340.294\,m/s \;\;;\;\; \mu_0 = 17.894 \cdot 10^{-6} Kg/ms \;\;;\;\; g_0 = 9.8067\,m/s^2$$

Mathematical model in the Troposphere $(z < 11000\,m)$:

$$\theta(z)_{z<11000} = T(z)/T_0 = (1 - 22.57 \cdot 10^{-6} \cdot z) \tag{2.4}$$

$$\delta(z)_{z<11000} = p(z)/p_0 = (1 - 22.57 \cdot 10^{-6} \cdot z)^{5.256} \tag{2.5}$$

$$\sigma(z)_{z<11000} = \rho(z)/\rho_0 = (1 - 22.57 \cdot 10^{-6} \cdot z)^{4.256} \tag{2.6}$$

Model in the first layer of the Stratosphere $(11000\,m < z < 20000\,m)$:

$$\theta(z)_{11km<z<22km} = T(z)/T_0 = 0.751 = Constant \tag{2.7}$$

$$\delta(z)_{11km<z<22km} = p(z)/p_0 = 0.223\, e^{-0.15788\left(\frac{z}{1000} - 11\right)} \tag{1.8}$$

$$\sigma(z)_{11km<z<22km} = \rho(z)/\rho_0 = 0.296\, e^{-0.15788\left(\frac{z}{1000} - 11\right)} \tag{2.9}$$

2.2. Important parameters

In model testing of airplanes, missiles or ships in wind tunnels, Reynold's number, Froude number and Mach number are accepted scale factors because they contain the variables which affect parachute performance. The testing models of airplanes, missiles or ships are rigid bodies mounted in wind tunnels and the data are recorded at different constant velocities. However the geometry of a deploying parachute undergoes dramatic changes as compared to the constant geometry of the rigid models. Thereby these scale parameters (Reynold's number, Froude number and Mach number) are unsuitable for parachute deployments because they don't take into account the change of geometry, which affect parachutes performance.

Therefore, for any scale parameter to be valid, it must contain those variables that affect the behaviour of the system. In the case of parachutes, the aforementioned parameters can be considered suitable if the steady state is considered (with constant geometry). This parameters will be described below.

In other cases as the parachute deployment and its inflation, in addition to these parameters will be necessary to take into account other variables that affect the parachute behaviour. In this case these parameters will be described in subsequent sections.

- Reynolds Number (Re): defines the relationship of mass forces to viscous friction forces in liquids and gases. It is calculated as

$$Re = \frac{\rho \cdot \mathrm{v} \cdot D_0}{\mu} = \frac{velocity\ (m/s) \cdot characteristic\ length\ (m)}{kinematic\ viscosity\ (m^2/s)} \tag{2.10}$$

  Reynolds number is an important criterion of viscous effects and allows comparison of model tests with full-scale flight tests. Table 2.1 shows examples of Reynolds numbers of various air vehicles.

Reynolds	Insect	Glider	Aircraft DC-3	Aircraft B-747	Drogue chute	Main parachute
	$6{\cdot}10^3$	$2.5{\cdot}10^6$	$24{\cdot}10^6$	$100{\cdot}10^6$	$50{\cdot}10^6$	$2{\cdot}10^6$

Table 2.4. Examples of Reynolds numbers for different air vehicles [2].

- Mach Number (M): is an important parameter of supersonic flight; it states how much faster than the speed of sound the air vehicle travels.

$$M = \frac{v}{c_S} = \frac{flight\ velocity\ (m/s)}{speed\ of\ sound\ (m/s)} \tag{2.11}$$

Depending on the configuration of the body, supersonic compressibility effects may occur in the 0.75-0.85 Mach range, causing local supersonic flow, shock waves, flow separation, and changes in stability.

- Froude Number (Fr): relates the effect of the forces of inertia and the forces of gravity acting on a fluid.

$$Fr^2 = \frac{centripetal\ force}{gravitational\ force} = \frac{\frac{mv^2}{l}}{mg} = \frac{v^2}{D_0 g} \tag{2.12}$$

It is a very useful performance number, since it relates the descent speed in a given gravitational field to the required size of the parachute canopy.

- Mass Ratio (R_m): is a measure of the ratio of air mass enclosed in the inflated canopy to the payload mass:

$$R_m = \frac{\rho D_0^3}{m} \tag{2.13}$$

The mass ratio is an important parameter during parachute inflation, since the progressive increase of the parachute diameter increases the value of the mass ratio.

This parameter can be expressed as a function of the Froude number considering that a vehicle is being retarded by a parachute with a steady descent velocity, and the drag of the vehicle can be neglected compared to that of the parachute [3].

$$\frac{1}{2}\rho v^2 C_D S_0 = m\, g \quad \rightarrow \quad v^2 = \frac{mg}{\frac{1}{2}\rho C_D \frac{\pi}{4} D_0^2} = \frac{8\, mg}{\pi \rho C_D D_0^2} \tag{2.14}$$

Combining equation (2.14) into equation (2.12):

$$Fr^2 = \frac{m}{\rho D_0^3}\ \frac{8}{C_D \pi} = \frac{8}{\pi}\ \frac{1}{R_m C_D} \quad \rightarrow \quad R_m = \frac{8}{\pi}\ \frac{1}{Fr^2\ C_D} \tag{2.15}$$

With this, the speed required to recover a payload can be analysed from these parameters. Considering a type of parachute with a certain drag coefficient, if it is desired to have a high speed of descent, the Froude number will be high and therefore the mass ratio will be small, i.e. the air mass enclosed in the canopy must be small, and consequently it allows a smaller parachute diameter. On the other hand, if it is desired to have a low speed of descent, the Froude number will be low, the mass ratio will be high, and therefore the required air mass will be greater and a larger parachute diameter will be required.

CHAPTER 3. Parachute recovery system and general considerations

This chapter will discuss the study of the tools needed to evaluate, analyse, select and design parachute recovery systems. In particular we will focus on providing general state of the art procedures for high performance parachute design. This includes the use of aerodynamic and structural analyses to predict parachute inflation, deceleration forces, parachute stability, or the required weight/volume among other considerations.

First of all it should be mentioned that the term "high performance" parachute may seem subjective and therefore it is necessary to clarify to what type of parachutes are concerned. The term high performance parachute includes those that are deployed at Mach numbers above 0.7 or dynamic pressures above 24 kPa. Parachutes that recover very heavy payloads at any deployment velocity are also considered to have high performance. And those parachutes whose weight is small compared to their size and the drag they produce, are considered to be high performance parachutes.

3.1. Parachute system boundaries

The range of application of the parachutes with respect to speed and altitude is very wide, since these can be developed specifically for supersonic speeds exceeding Mach 4, and altitudes above the limits of the atmosphere with dynamic pressures up to 15,000 psi. Figure 3.1 gives an idea of the performance limits of the parachutes developed for different missions. These boundary limits can move both upward and outward as new materials and technological advances are introduced.

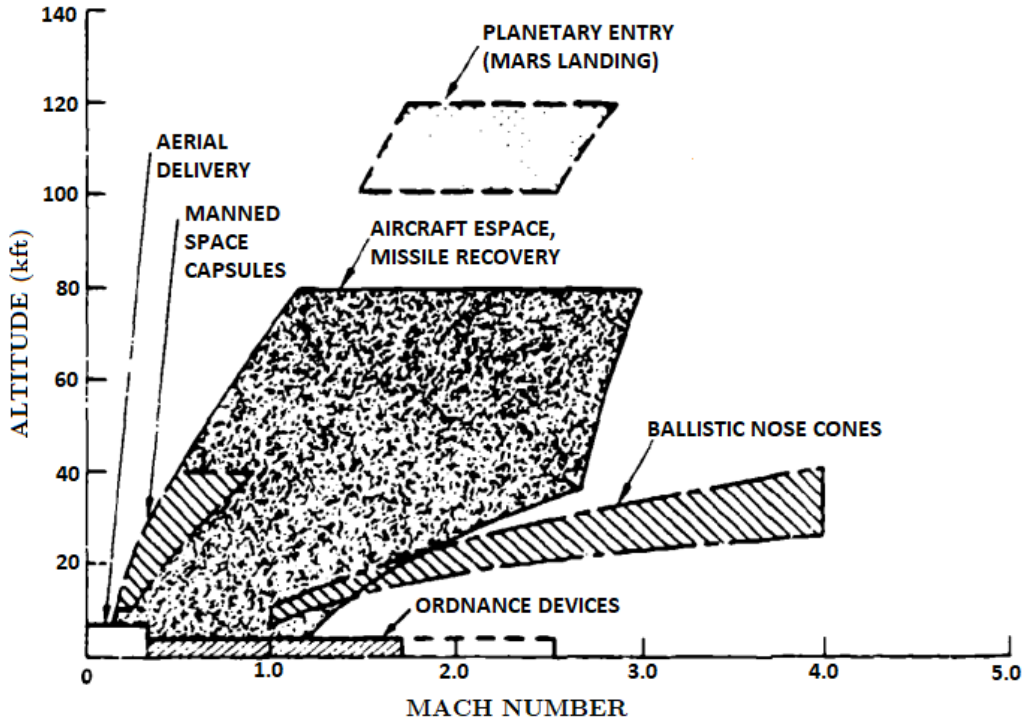

Figure 3.1. Parachute Performance Envelopes [2].

3.2. Parachute design considerations

To select and design a parachute system, the performance characteristics of such parachute must be considered and known. These performance characteristics can be many and varied, referring to different criteria such as economic, aerodynamic or structural scope. The importance of these performance characteristics is different according to the application of the parachute system and therefore it is not possible to find general guidelines for designing a parachute with a certain application.

The Table 3.1 lists some possible design criteria:

Reliability	Indifference to Damage
Stability	Simplicity of Design and Manufacturing
High Drag	Simplicity of Maintenance and Service
Low Opening Shock	Low Acquisition Cost
High Mach Capability	Low Life Cycle Cost
Low Weight and Volume	Weight Efficiency $(C_D \cdot S)_0/W_P$
Repeatability of Performance	Volume Efficiency $(C_D \cdot S)_0/V_P$
Environmental Adaptability	Cost Efficiency $(C_D \cdot S)_0/\$$

Table 3.1. Parachute Design Criteria [2].

Of all these criteria, one could say that *reliability* is always an important parameter, since a parachute with a high degree of reliability determines the success or failure of the mission. For this, it is necessary to analyse and thoroughly review the whole process that the parachute system performs.

Weight and *volume* are also very important considerations, which strongly influence the landing. Normally the structure of a parachute system constitutes 5% of the total weight of a light vehicle, or 3-4% for heavier vehicles.

Parachute selection frequently begins with the *stability* requirement. This requirement limits the oscillation of the parachute, so that a high level of stability automatically eliminates many types of high-drag parachutes or involves the use of parachute clusters.

The *drag coefficient* is an important parameter in the selection of the parachutes in the final descent. This parameter influences the weight-efficiency ratio criteria, which shows how much Drag area $(C_D \cdot S)_0$, is produced per kilogram of parachute W_p.

Repeatability and *maintenance* are factors that directly influence the cost of the parachute system.

Table 3.2 shows a guide to evaluate the importance of some parachute performance characteristics according to different applications. Each designer can use different rating values based on the specific requirements of a particular application.

PERFORMANCE CHARACTERISTICS	APPLICATION				
	Spacecraf landing	Airborne troops	Aircraft landing	Ordnance	Aerial resupply
Reliability of operation	3	3	3	3	2
Repeatability of performance	2	2	2	3	1
Reuse	0	3	0	0	3
Low weight and volume	3	2	3	2	1
Stability	2	2	2	3	2
High drag	2	2	2	2	3
Low opening forces	1	3	2	2	3
Low maintenance/service	1	3	2	2	3
Cost	1	2	2	2	3

3= high importance	1=low importance
2= medium importance	0= not applicable

Table 3.2. Comparative Rating of Performance Characteristics for Various Parachute Systems Applications [2].

3.3. Parachute structural analyses

3.3.1. Basic description of High-performance Parachutes

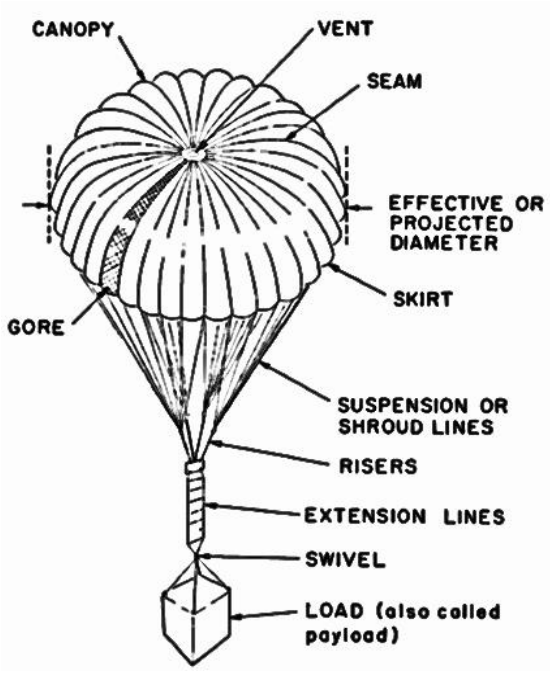

Figure 3.2. Principal components of a parachute [4]

Before discussing specific high-performance parachute configurations in detail, it is necessary to identify their principal parts and define the parameters and nomenclature used to measure their performance. Figure 3.2 illustrates the basic features of a parachute:

The canopy is the cloth surface that inflates to a developed aerodynamic shape to provide the lift, drag and stability needed to meet performance requirements. Canopies are formed from a number of gores bounded on each side by a radial seam (on the top edge by the vent band and on the bottom edge by the skirt band).

The suspension or shroud lines transmit the force form the canopy to the payload, either directly or through risers attached below the convergence point of the suspension lines to the body. This point of convergence of all suspension lines is called the confluence point.

The crown is the region of the canopy above the major diameter of the inflated shape, and the small circular opening at the centre of the crown is called the vent, which serves to simplify fabrication and provides flow-through relief for the initial surge of air when it impacts the canopy at the start of inflation.

The payload may be fastened directly to the lower end of the risers, but if there is reason to suspend it lower, extension lines are used. If it is desirable that the payload can be free to turn independently of the parachute, a swivel may be placed in the suspension system anywhere below the risers.

The open region at the apex of the canopy is the *vent* ($\boldsymbol{D_v}$). The portion that extends below the major diameter of the inflated canopy shape to the leading edge of the canopy is the *skirt*. On the skirt it can be measured the *projected diameter* ($\boldsymbol{D_p}$) of the inflated parachute, but since this latter is a function of the parachute's inflated shape and the load that it is carrying, parachutes are usually described by their *nominal diameter* ($\boldsymbol{D_0}$), which is the effective diameter of a circle whose area is the *nominal area* ($\boldsymbol{S_0}$). The nominal area is the actual three-dimensional canopy surface area, computed as the sum of the gore areas.

Another reference dimension of parachutes is the *constructed diameter* ($\boldsymbol{D_c}$), the diameter of the parachute measured along the radial seam when projected on a planar surface. Another important parameter that defines the parachute geometry is the *suspension line length* ($\boldsymbol{l_e}$), the distance from the canopy skirt to the confluence point.

In the Figure 3.3 it can be observed the different parameters mentioned:

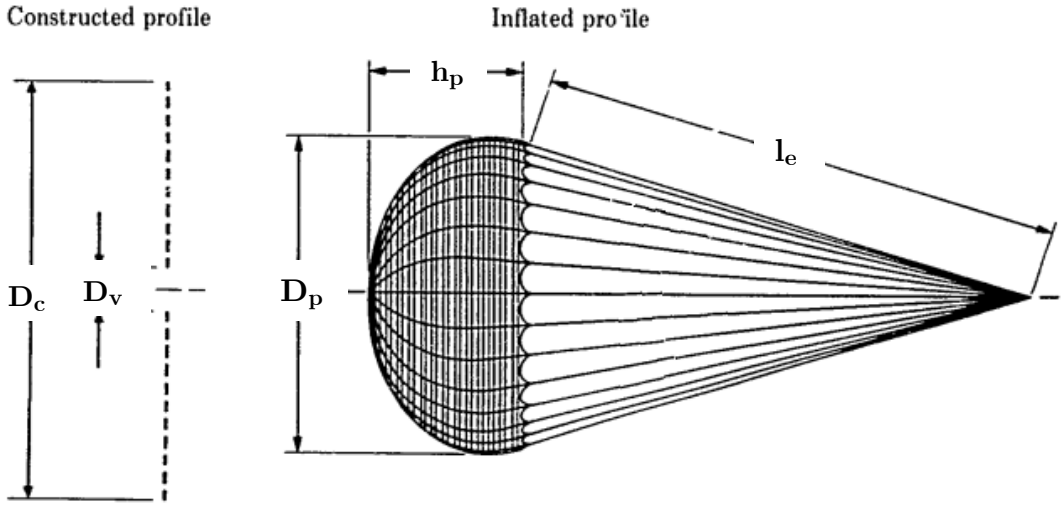

Figure 3.3 Geometric parameters of a parachute [4].

A Table with typical high-performance parachute with most of the shape factors, general aerodynamic characteristics and applications of the parachutes are listed in the Appendix A [5]. Numerical values for inflated shape factor (D_c/D_0) and drag coefficient (CD_0) represent a range of values influenced by geometric factors and fluid dynamic parameters such as: canopy size, canopy porosity, Mach number, suspension line length, material, air density or dynamic pressure. The influence of these factors will be discussed in subsequent sections.

3.3.2. Parachute Deployment

Parachute deployment denotes the sequence of events that begins with the opening of a parachute compartment attached to the body to be recovered and continues with extraction of the parachute until the canopy and suspension lines are stretched behind the body and the parachute is ready to start the inflation process.

This deployment is associated with a mass shock (snatch force) created by the acceleration of the mass of the parachute to the velocity of the body to be recovered. Therefore, the task of a good deployment system is to limit the mass shock by controlling the parachute deployment process and providing means for progressive incremental acceleration of all parts of the parachute.

Parachute and riser should be stored in a textile envelope for protection during deployment and to ensure a controlled deployment that keeps tension on all parts of the parachute and riser. The textile envelope, called the deployment bag, usually have separate compartment for the canopy, suspension lines and for the riser. These compartments allow an incremental deployment sequence, thereby maintaining order and tension on all parts of the deployment parachute assembly.

There are several deployment methods, that fit better or worse according to the needs required by the operation.

a) Uncontrolled deployment:

The parachute is ejected into the airstream without a pilot chute, drogue chute, or deployment bag. This can be acceptable for small parachute, but is unacceptable for larger parachutes because it results in high snatch forces and partial canopy inflation before line stretch.

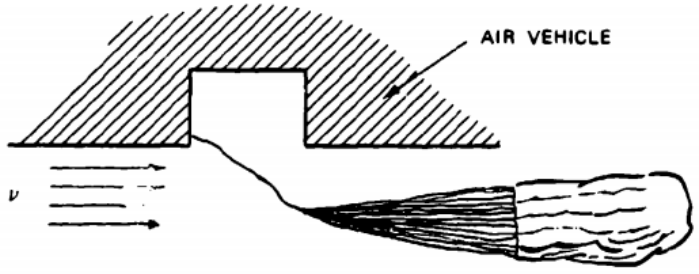

Figure 3.4. Uncontrolled Deployment [2].

b) Semicontrolled deployment:

Semicontrolled deployment uses a pilot chute for extracting the main parachute. It works with medium-sized parachutes at low velocities, but at high speeds, the pilot chute can be powerful enough to cause high snatch loads. Partial canopy inflation before canopy stretch can also occur with this deployment.

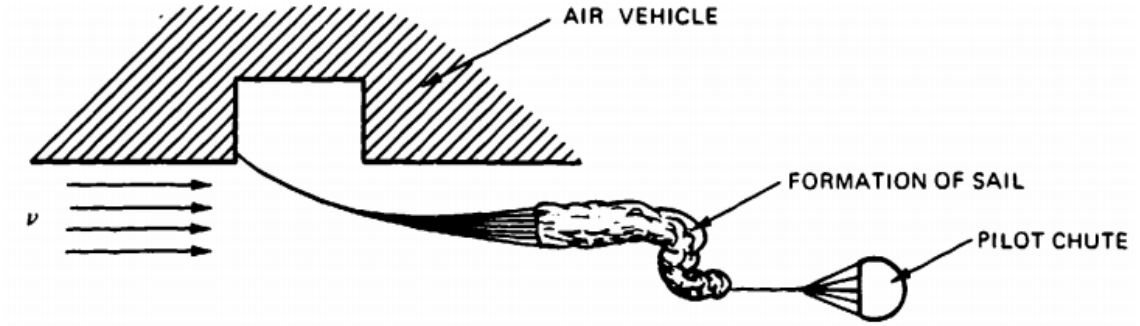

Figure 3.5. Pilot Chute Deployment [2].

c) Static-Line deployment:

A static line is attached on one side to the air vehicle and on the other side to the parachute assembly. First open the parachute pack and then pull the parachute out of its deployment bag. It is a typical method used by paratroopers and is limited to aircraft speeds of about 240 km/h.

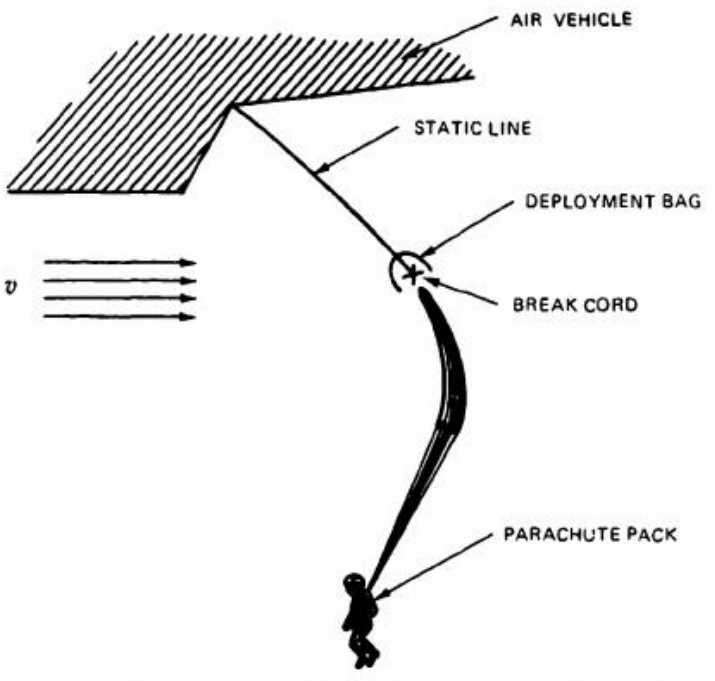

Figure 3.6. Parachute Static-Line Deployment [2].

d) Controlled deployment:

It is the basic deployment method for all parachute used for the recovery and retardation of air/space vehicles, ordnance items and high-speed payloads.

Controlled parachute deployment starts with the forced ejection of a parachute compartment cover that pulls a pilot chute away from the air vehicle. The sequence in the deployment of the parachute assembly is: riser, suspension lines and canopy. The deployment bag of the main parachute contains compartments that ensure a controlled deployment with tension on all parts of the parachute.

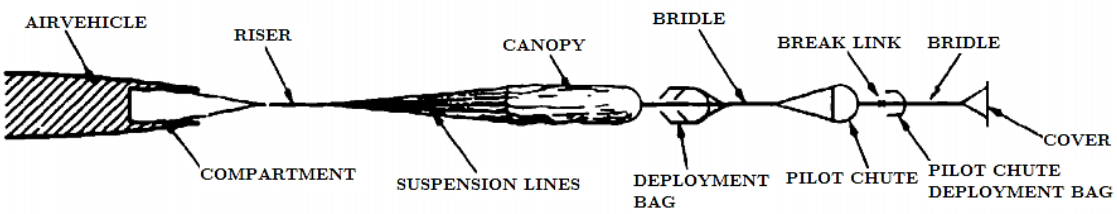

Figure 3.7. Controlled Parachute Deployment Concpet [2].

3.3.3. Pilot Chutes

Pilot chutes are used to deploy large parachutes from their storage packs or containers into good airflow behind the vehicle. Its task consists in first extracts the parachute pack from the vehicle compartment and then deploys the main parachute form its deployment bag. For achieve this, some requirements, based on experience, can be defined for pilot chutes:

- Pilot chutes must open quickly and reliably.
- Pilot chutes must be stable and must have sufficient drag to pull the main parachute pack away from the payload and extract the main parachute.
- The recommendation is to eject the pilot chute to a distance equivalent to at least four, and, if possible, six times the forebody diameter behind the vehicle.
- As a rule, the pilot chute extraction force should be equal to or larger than four times the weight of the parachute assembly to be extracted.

Values of drag coefficients and opening-force coefficients for typical pilot chutes are shown in Table 3.3:

Pilot Chute type	**Drag Coefficient,** C_{D0}	**Opening-force coefficient,** C_X
Square box	0.60	2.0
Ribbon, conical	0.52	1.3
Ringslot	0.60	1.4
Guide surface	0.42	2.0

Table 3.3. Pilot Chute Drag and Opening-Force Coefficients [2].

3.3.4. Parachute Stress Analysis

Since textiles are the primary materials used in parachutes, their characteristics must be considered in establishing design factors and in dimensioning the various elements of the parachute assembly. Textiles are used for cloth or ribbons of the parachute canopy; for webbings, lines and tapes for suspension lines and canopy reinforcements; and for some parts of deployment bags and related components. These textile components are affected much more than are metals by such environmental factor as temperature, humidity, radiation, chemicals or aging; and such mechanical factors as abrasion, handling and packing.

It is very difficult to determine the load and stress distribution for a variable-geometry, variable-velocity inflating canopy. Mullins and Reynolds developed a computerized system for calculation the stresses in ribbon parachutes. This method, called CANO program, was modified and improved by the University of Minnesota and the Sandia National Laboratories [6]. The improved version of the CANO program published by the Sandia National Laboratories was called Canopy Load Analysis (CALA) [7].

Prior to the CANO program, three methods were developed that give a good approximation for determining the maximum force that could experiences the canopy. Because this maximum force occurs during the canopy filling process, these three methods will be clarified in the section related to inflation of the canopy, since some concepts of this process should be explained before to understand the methods.

3.3.5. Textile Materials

It is not the purpose to provide a detailed analysis of the complex area of textiles and fabrics, but rather to provide a general overview of the textiles used in the design and manufacture of parachute assemblies.

The two primary groups of textiles are those of natural fibers and those of man-made fibers. Natural fibers include wool, cotton, silk, flax and many others, but only silk and cotton are of interest to parachute design. Man-made fibers are classified by their origins. Mineral fibers, the only nonorganic fibers, include glass fiber and metal thread used in woven metals. All other man-made fibers are based on cellulose, protein, or resin composites. The cellulose group includes rayon, and the protein and resin groups include nylon, dacron or Kevlar.

In the Appendix B [2] the main characteristics of the mentioned textile materials are listed in a table. Of all these textile materials, it is important to mention that Kevlar has become very used as high-tenacity material for parachute assemblies. Kevlar is about 2.5 to 3 times stronger than nylon and is considerably more heat resistant. Hybrid parachutes using nylon canopies and Kevlar suspension lines, risers and canopy tapes can reduce weight and volume by 25% to 40%, depending on the amount of Kevlar used.

3.3.6. Parachute Recovery System Weight and Volume

The relationship of weight and volume can be expressed by the amount of parachute weight that can be packed into 1 cubic foot of volume. This introduces the importance of pressure packing. The higher the pressure, the more weight can be stowed in a given space. Although nylon parachutes and all-Kevlar parachutes can be packed with similar pressures, Kevlar parachutes increase the pack density because of the 26% higher specific weight of Kevlar, as it can be seen in Appendix B.

There are mainly four methods for calculating the weight of a parachute recovery system: the preliminary design method [2]; the drawing method [2]; the TWK method [2]; and the Keneth E. French Method [8].

a) The preliminary design method:

This method uses data of weight of different types of parachute recovery systems. Figure 3.8 shows the percentage weight of a parachute recovery system and its various components as functions of the primary vehicle weight. As it can be seen in the graph, the percentage weight of the parachute recovery system components decreases with an increase in vehicle weight because of the relative weight decrease of the various components.

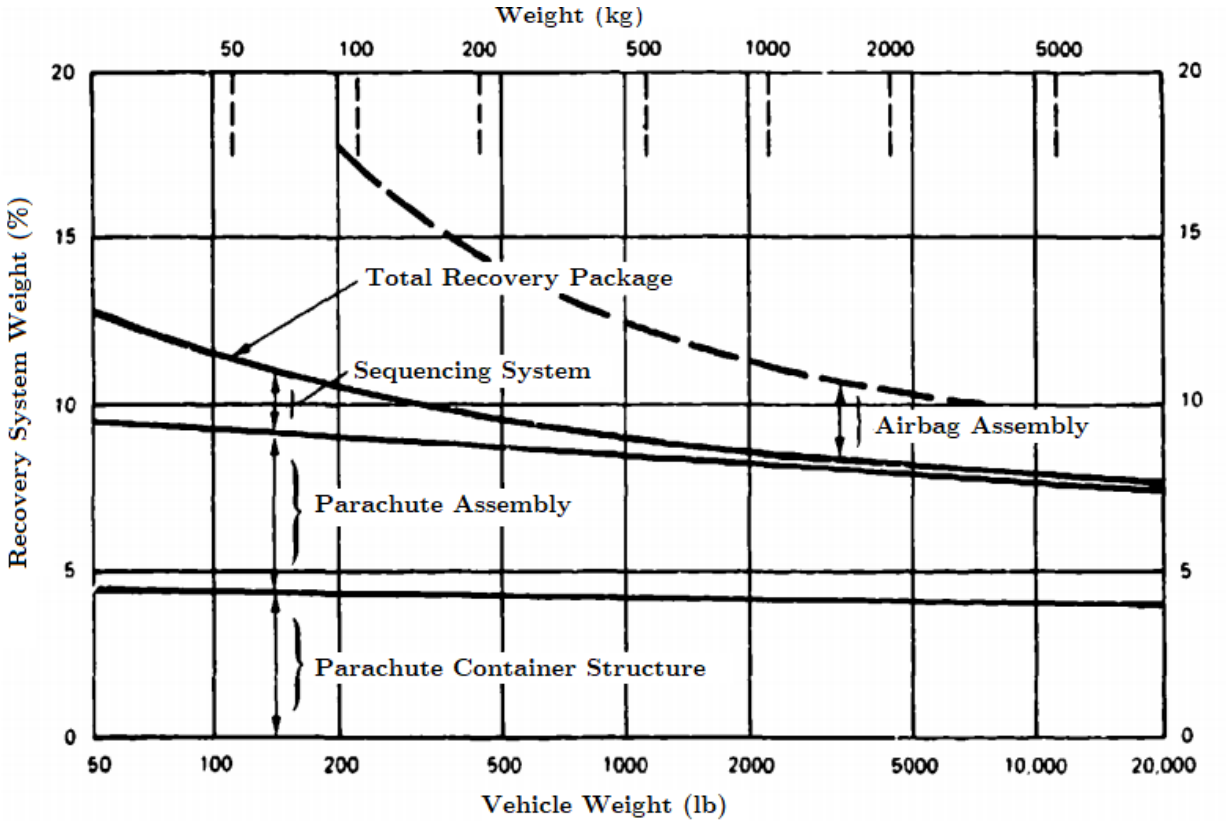

Figure 3.8. Parachute recovery system weight as percentage of air vehicle weight [2].

As a simple and quick general rule, deployment bags weigh 5 to 6% of the parachute system, and deployment bags plus pilot chute add 3 to 5%. First-stage drogue-chute assemblies will weigh from 25 to 40% of the main parachute weight depending on the deployment dynamic pressure and riser length. Parachute cluster have 5 to 10% higher weight than a single parachute of equal drag area because of the loss in drag caused by cluster interference.

This is not a very precise method, especially if the required parachute differs significantly from the parachutes considered in the graphs. In any case, it allows us to have an approximate idea of the weight of the parachute system.

b) The drawing method:

If detailed drawings with material lists are available, the weight of the parachute assembly can be determined from the material and hardware specifications. Experience shows that this method is usually precise because the estimated weight is frequently about 5% higher than the weight of the manufactured assembly.

c) The TKW method:

If no detailed drawing is available, but the primary dimensions of the parachute are known, the following method will give good weight data. The weight of a parachute can be written in following form:

$$W_P = S_0 \cdot w_c + D_0/2 \cdot N_G \cdot w_{RT} \cdot F_{RT}/1000 + N_{SL} \cdot L_S \cdot w_{SL} \cdot F_{SL}/1000 \qquad (3.1)$$

Where:

- W_P is the weight of the parachute (lb or kg).
- S_0 is the surface area of the finished canopy (ft^2 or m^2).
- w_c is the specific canopy weight (lb/ ft^2 or kg/m^2).
- N_G is the number of radials (gores) in the canopy.
- w_{RT} is the specific weight of the radial tape (lb/ft/1000-lb).
- F_{RT} is the strength of the radial tape (lb or kg).
- N_{SL} is the number of suspension lines.
- L_S is the length of suspension lines (ft or m).
- w_{SL} is the specific weight of suspension lines (lb/ft/1000-lb).
- F_{SL} is the strength of suspension lines (lb or kg).

In this formula $S_0, N_G, N_{SL}, L_S, F_{RT}, F_{SL}$ are known preliminary design data.

d) The Kenneth E. French method:

This method is only used to estimate the weight of the parachute canopy in a fast but effective way in preliminary design tasks, where the riser, deployment bag, and special attachment link weights are excluded. Kenneth E. French [8] collected the weight of 59 different parachutes with conventional materials as nylon, including different sizes of Flat solid, Ext. skirt, Ringslot, Flat ribbon and Conical ribbon. Most of them were of a relatively conventional construction with $L_S/D_0 \sim 1$ and $N_{SL} \sim D_0$. Figure 3.9 shows weight versus $N_{SL}P_sD_0$ on log-log scales for these parachutes, where P_s (Newtons), is the rated ultimate strength of suspension line.

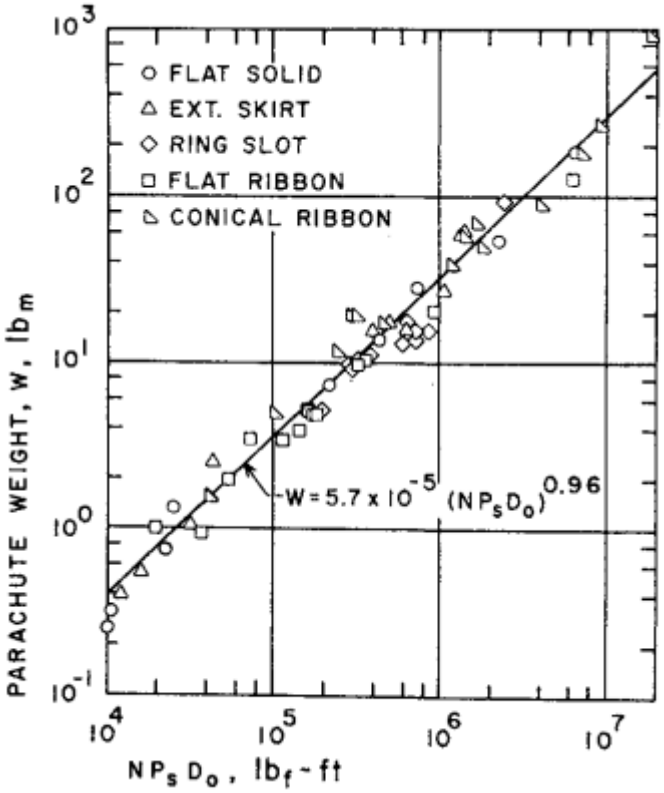

Figure 3.9. Parachute weight vs NP_sD_0 [8].

The straight line shown in Figure 3.9 is:

$$W(kg) = 1.9 \cdot 10^{-5}(N_{SL}P_sD_0)^{0.96} \tag{3.2}$$

The data scatter in Figure 3.9 appears due as much to variations within each specific type of chute as to type-to-type variations. Thus, the incorporation of all types of chute in one graph appears valid.

The nominal weight value of equation (3.2) multiplied by 1.21 should provide a fairly conservative maximum weight for estimating purposes. For most chute applications, if there are small changes in deployment conditions $N_{SL}P_s \propto F_X$. This relationship can be used to obtain the variation in W for small variations in q and D_0.

3.4. Parachute aerodynamic analyses

3.4.1. Stability of parachute systems

Stability is the tendency of a body to return to an equilibrium position after a displacement of that position. Such stability must be considered both from a static and from a dynamic point of view.

Thus, a system is considered to be "statically stable" when in that system a moment develops in the direction that allows restoring equilibrium. In addition, if a system presents static stability on one of its axis, it doesn't necessarily mean that it is stable on any other axis, and therefore it is important to define the axis on which the stability of the system is considered. The criterion that defines the static stability of a parachute in pitch can be expressed mathematically by the variation of the pitch moment with respect to the angle of attack:

$$\begin{gathered} \frac{\partial M_G}{\partial \alpha} < 0 \rightarrow stable \\ \frac{\partial M_G}{\partial \alpha} = 0 \rightarrow neutrally\ stable \\ \frac{\partial M_G}{\partial \alpha} > 0 \rightarrow unstable \end{gathered} \tag{3.3}$$

On the other part the "dynamic stability" refers to the damping of the continuous movement of a body as a consequence of the frictional forces and the gravitational component. But the fact that a body is dynamically stable is not enough, because it is really important that the time to reduce its oscillation to an external disturbance is adequate and thus avoid too high amplitudes of oscillation.

Figure 3.10 shows the static stability of various parachutes through the variation of pitch coefficient with respect to the angle of attack $(\partial C_m/\partial \alpha)$.

A negative $\partial C_m/\partial \alpha$ of the moment coefficient curve indicates that the parachute is stable and will return to its zero-angle-of-attack position after a disturbance. Therefore, as it can be observed, the solid, flat, circular canopy is a typically unstable parachute which oscillates between ± 25 dregrees. And the ribbon and guide surface parachutes will return to their zero-angle-of-attack attitude if they are displaced, as indicated by the negative slope of the $\partial C_m/\partial \alpha$. It can also be observed that the greater the porosity of the parachute, the smaller is its oscillation.

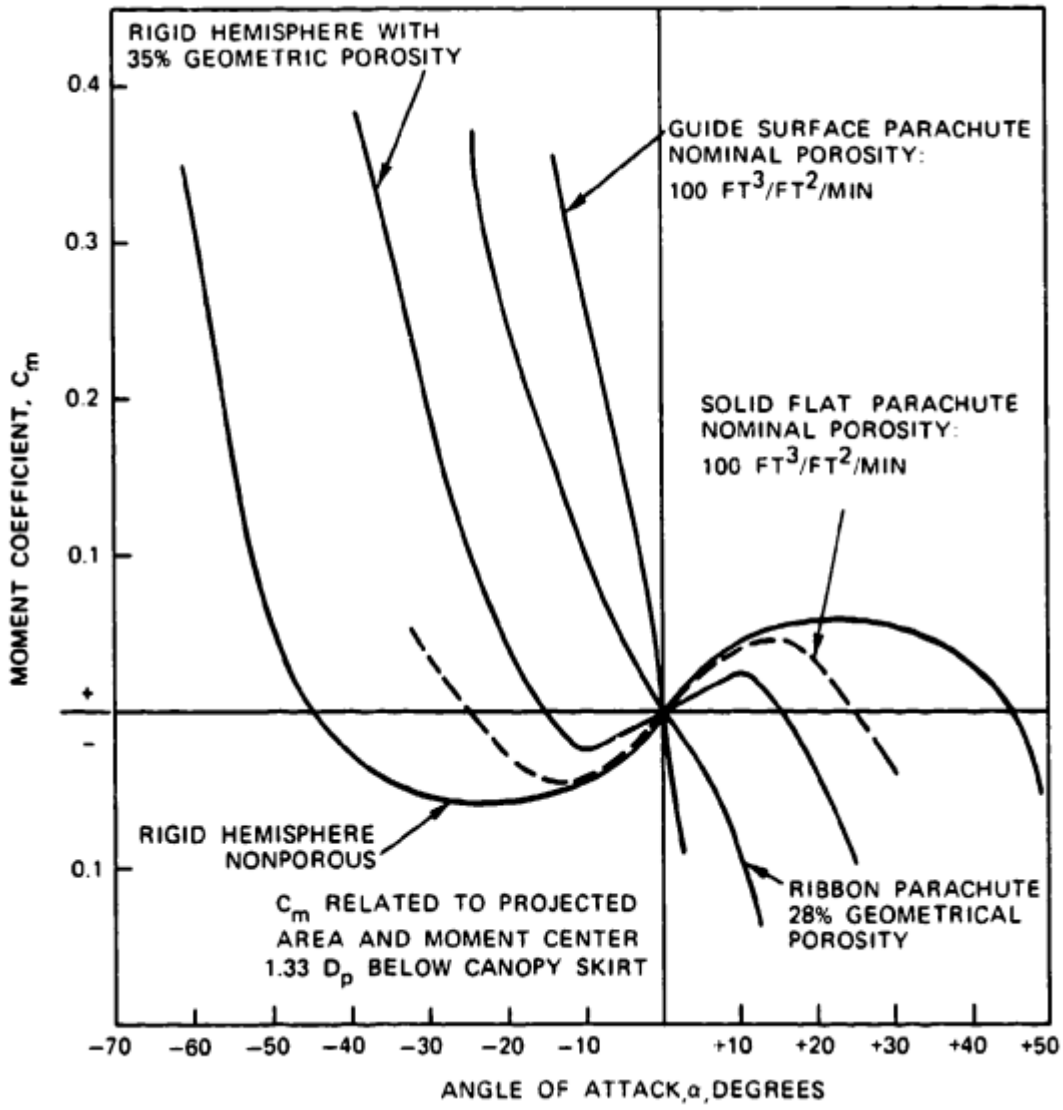

Figure 3.10. Static stability of different parachute types [2].

The stability characteristics of a parachute are strongly influenced by the porosity with which the parachute is made. Then in an imporous hemisphere (Figure 3.11.A), the airflow cannot get through the canopy but goes around and separates on the leading edge of the hemisphere in alternating vortexes, forming what is called the Karman Vortex Trail. This separation causes alternate pressure areas on opposite sides of the canopy, and these pressure areas produce the parachute's oscillations. But if the canopy includes openings (Figure 3.11.B), part of the air flows through the canopy and forms a uniform wake consisting of small vortexes. In addition, the airflow separates uniformly around the leading edge of the canopy, eliminating the destabilizing alternate flow separation of the Karman Vortex Trail.

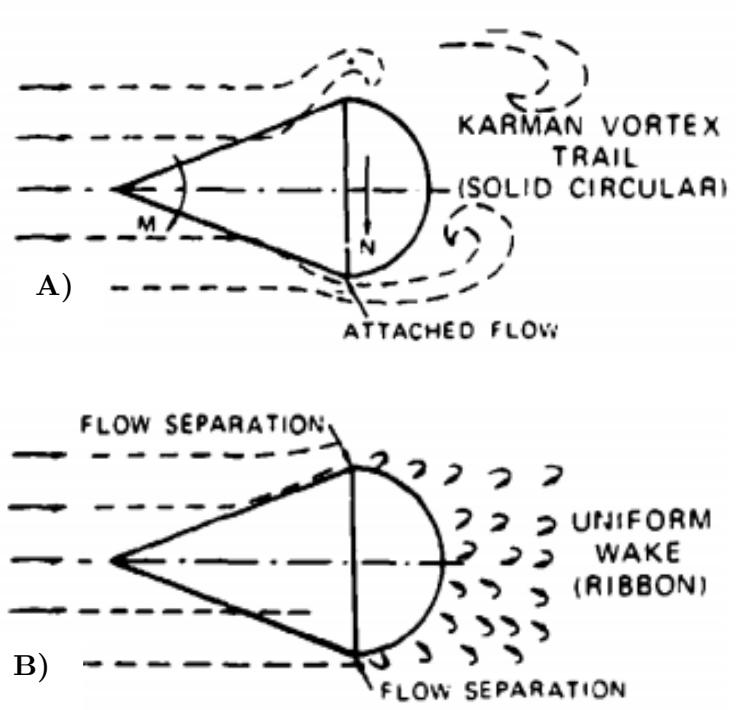

Case A) Imporous canopy, instability caused by side force N.

Case B) Porous canopy, no side force, no unstable moment.

Figure 3.11. Relationship of Ariflow and Stability depending on porosity [2].

3.4.2. Parachute inflation process

Parachute inflation is defined as the time interval from the instant the canopy and lines are stretched to the point when the canopy is first fully inflated. Figure 3.12 shows the phases of the canopy inflation.

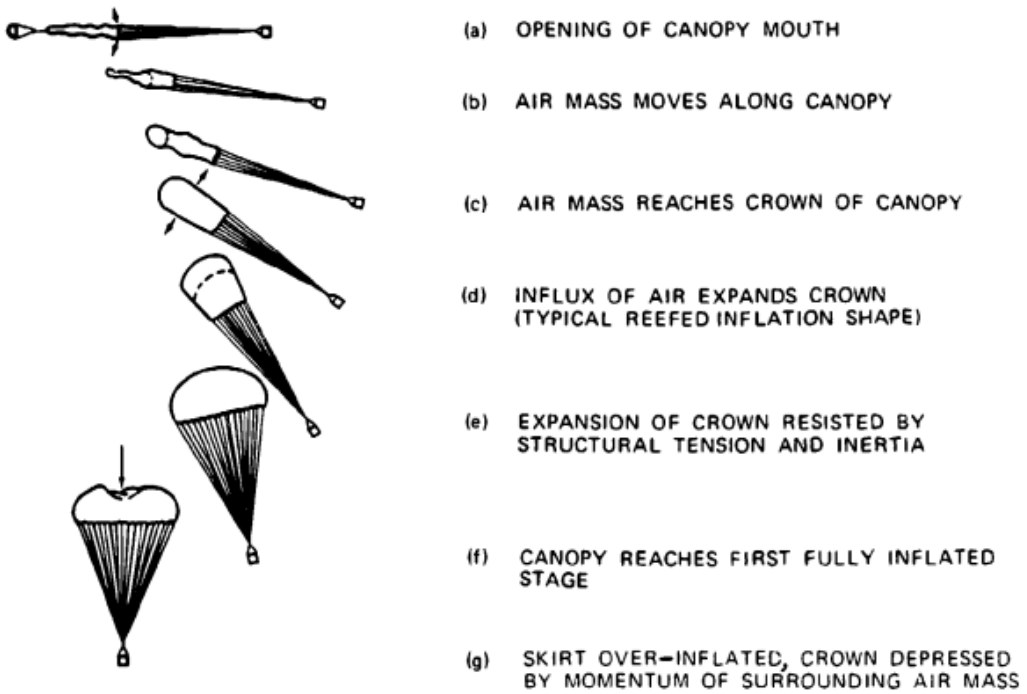

Figure 3.12. Parachute Canopy Inflation Process [2].

The canopy filling process begins when canopy and lines are stretched and when air begins entering the mouth of the canopy (a). After the initial mouth opening, a small ball of air rushes toward the crown of the canopy (b). As soon as this initial air mass reaches the vent (c), additional air starts to fill the canopy form the vent toward the skirt (d). The inflation process is governed by the shape, porosity, size of the canopy and by air density and velocity at the start of inflation. Inflation is slow at first but increases rapidly as the mouth inlet of the canopy enlarges (e) and the canopy reaches its first full inflation (f). And finally most solid textile canopies overinflate and partially collapse because of the momentum of the surrounding air (g).

During this process it is important to consider that the amount of air toward the canopy vent at point (b) should be small to avoid a high-mass shock when the air bubble hits the vent of the parachute. Furthermore, the inflation of the canopy should occur axisymmetrically to avoid overstressing of individual canopy parts. And the overinflation phenomena after the first initial opening should be limited to avoid delay in reaching a stable descent position.

Several methods have been developed to obtain quantitative values for opening time and force. These methods vary from easily usable empirical models to models whose comparison is as complex as they are almost useless for parachute designers.

a) Canopy inflation time

Knowledge of the canopy filling time, defined as the time from canopy stretch to the first full open canopy position, is important. Over the years many authors have developed numerous methods to calculate this filling time considering different types of parachutes.

Mueller [9] y Scheubel [10] assumed, based on the continuity law, parachutes should open within a fixed distance, because a given conical column of air in front of the canopy is required to inflate the canopy. This fixed distance is proportional to a parachute dimension such as the projected diameter, D_p. Therefore the *filling distance* for a specific parachute can be defined as:

$$s_f = n \cdot D_p \tag{3.4}$$

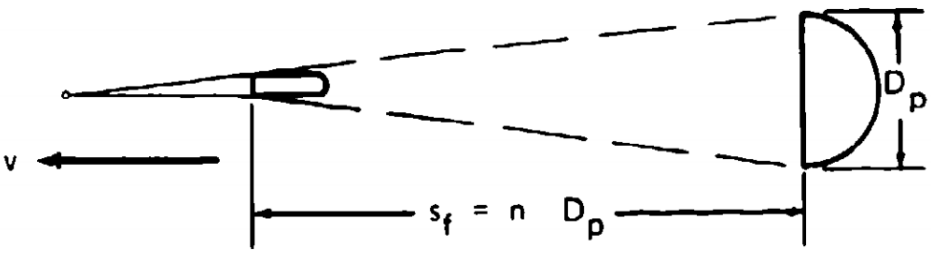

Figure 3.13. Filling distance of a parachute canopy [2].

Because the parachute diameter, D_p, is variable, the fixed nominal diameter, Do, is used to calculate canopy filling time [2]:

$$t_f = \frac{n \cdot D_0}{v} \tag{3.5}$$

Where:

- D_0 is the nominal parachute diameter.
- v is the velocity at line stretch.
- n is a constant typical for each parachute type, indicating the filling distance as a multiple of D_0.

This basic fillig-time equation was extended by Kancke, Fredette, Ludtke and others [11, 12], providing good results.

- Ribbon Parachute (Knacke)

$$t_f = \frac{n \cdot D_0}{0.9\, v} \;; \qquad \text{Where n = 8 for Ribbon parachutes} \tag{3.6}$$

- Ribbon Parachute in high-speed tests (Fredette)

$$t_f = \frac{0.65\, \lambda_T \cdot D_0}{v} \tag{3.7}$$

Where λ_T is the total canopy porosity expressed as a percent of the canopy surface area.

- Solid Flat Circular Parachute (Wright Field)

$$t_f = \frac{n \cdot D_0}{0.85\, v} \tag{3.8}$$

Where n=4 for standard porosity canopies, and n=2.5 for low porosity canopies.

- Cross Parachute (Silver Spring)

$$t_f = \frac{(C_D S)_p \cdot n}{v^{0.9}} \qquad \text{Where n=8.7} \tag{3.9}$$

- Reefed Parachutes: Parachute reefing is a method that permits the incremental opening of a parachute canopy, or restrains the parachute canopy form full inflation or overinflation. This method consists mainly of two stages: reefing the parachute provides a temporarily high rate of descent with a low drag area that permits a more accurate drop form high altitude; and disreefing the parachute provides a low-impact velocity.

$$t_{f1} = \frac{n_1 \cdot D_0}{v_s} \cdot \left[\frac{(C_D S)_R}{(C_D S)_0}\right]^{\frac{1}{2}} \quad and \quad t_{f2} = \frac{n_2 \cdot D_0}{v_R} \cdot \left[\frac{(C_D S)_0 - (C_D S)_R}{(C_D S)_0}\right]^{\frac{1}{2}} \tag{3.10}$$

Where:

- t_{f1} and t_{f2} are the reefed and disreefed filling times.
- v_s and v_R are the velocities at line stretch and at disreef.
- $(C_D S)_R$ and $(C_D S)_0$ are the reefed- and full-open drag areas.
- n_1 is 10 for ribbon parachutes or 8 for ringsail parachutes.
- n_2 is 6 for ribbon parachutes or 2 for ringsail parachutes.

Some types of ribbon parachutes have been opened in the velocity range of up to Mach 4, where the canopy filling time at supersonic speed can be considered constant, because the canopy operates behind a normal shock. In later sections, we will focus on the applications of these supersonic parachutes.

b) Parachute drag-area increase during inflation process

The parachute drag area, $(C_D S)_P$, increases from 0 to 100% during canopy inflation. This drag-area-versus-time curve normally has a specific shape for each canopy type and it may be drawn out or compressed by reefing, changes in porosity distribution or other means. However, the basic configuration of the curve is maintained for a particular type of parachute, as the Figure 3.14 and Figure 3.15 show:

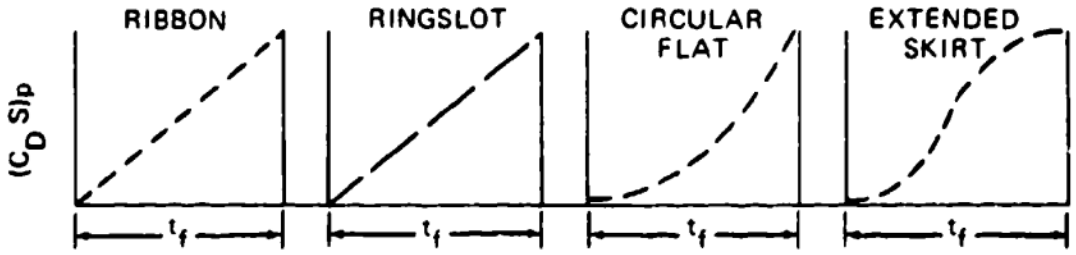

Figure 3.14. Typical Drag-Area-Versus-Time Increase for Various Parachute Types [2].

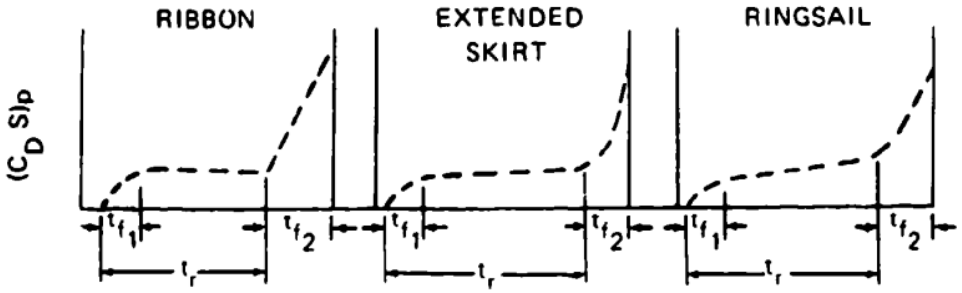

Figure 3.15. Typical Drag-Area-Versus-Time Increase for Reefed Parachutes [2].

This drag-area could be called more precisely "dynamic drag area", because it is obtained from the measured instantaneous force over the instantaneous dynamic pressure. Therefore it includes characteristics that affect the opening process, such as apparent mass and altitude density.

Data on drag-area-versus-time increase for the various parachute types are important for establishing the force-trajectory-time analysis of parachute recovery systems.

c) Effect of canopy loading, $W/(C_D S)_P$, on parachute opening forces

To analyse the effect of canopy loading, two general types of behaviour can be taken into account: parachutes opened under conditions of infinite mass and parachutes opened under finite mass conditions.

When infinite mass condition is considered, the velocity doesn't decay during parachute inflation and the parachute acts as if it were attached to an infinite mass. This condition is characteristic of high canopy loading. And when finite mass condition is considered, the velocity during the parachute opening decreases substantially and is representative of low canopy loading.

An additional typical difference between infinite and finite mass conditions is the location of the so called peak opening force, F_x. For a parachute opened under infinite mass conditions, or high canopy loading, the peak opening force occurs at the first full canopy inflation. But the peak opening force of a parachute opened at a finite mass condition will occur long before the parachute canopy is fully open. In the Figure 3.16 it is shown the different force-time diagrams.

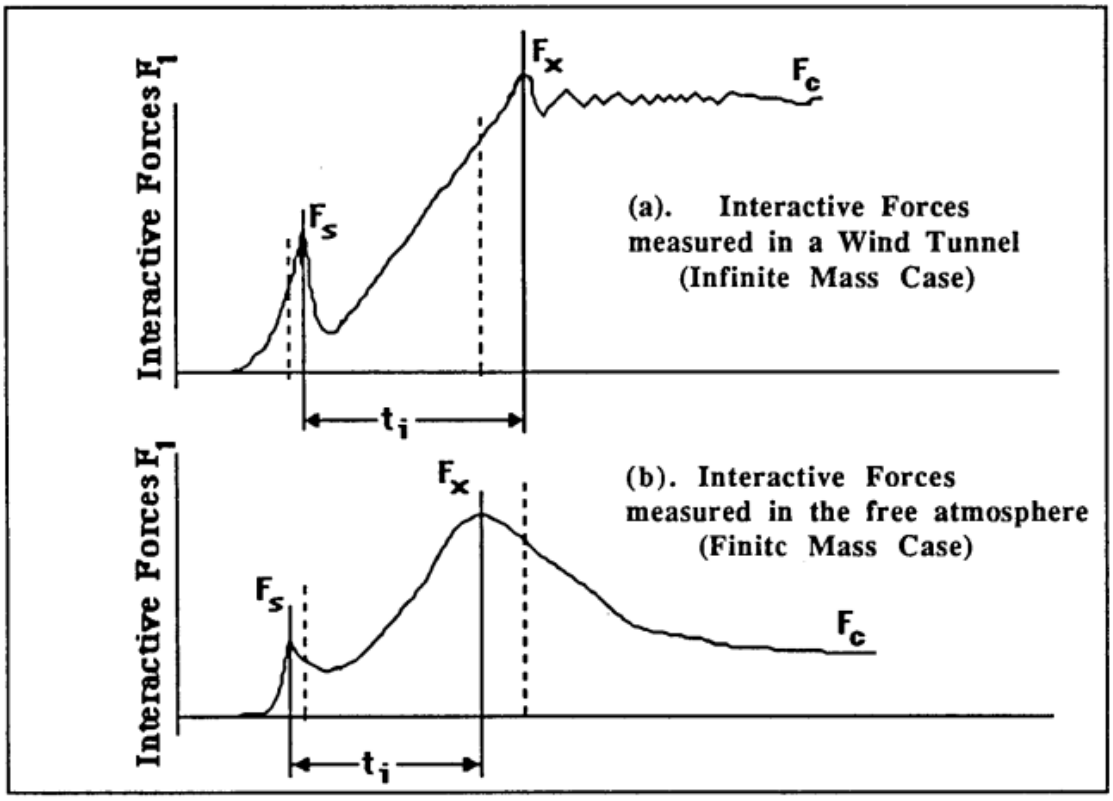

F_s: Snatch Force ; F_x: Peak Opening Force ; F_c: Steady-state Force ; t_i: Inflation Time

Figure 3.16. Force-versus-Time diagrams for infinite and finite mass conditions [3].

Defining the opening-force coefficient, $\boldsymbol{C_x}$, as the relationship of the peak opening force, F_x, to the steady-state drag force, F_C, the equation for the parachute force can be written:

$$F_x = F_c \cdot C_X \cdot X_1 = (C_D S)_P \, q \cdot C_X \cdot X_1 \tag{3.11}$$

Where:

- $(C_D S)_P$ is the drag area of the fully open parachute.
- q is the dynamic pressure.
- C_X is the opening force coefficient at infinite mass. Its value depends on each type of parachute.
- X_1 is the opening-force-reduction factor. Its value is 1.0 for a parachute opened at the infinite mass condition, and is as low as 0.02 for a low canopy loading.

d) Methods for calculating parachute opening forces

The most common methods for calculation parachute opening forces are three. The Method 1, the $W/(C_D S)_P$ *method* [20], is fast but should be used for preliminary calculations only. Method 2, the *Pflanz method* [23], is mathematically exact and provides good results within certain application limits. Method 3, the *computerized force-trajectory-time method* [24], gives good results with no limitations. However, all three methods require knowledge of certain parachute and opening-process characteristics.

In this case, of all these methods, the second one will be detailed below, since for a preliminary design it is considered more accurate than the first method and less complicated than the third method.

The *Pflanz method* is based on the following concept: a body of known fixed weight and velocity is decelerated along a vertical flight path by an aerodynamic drag device whose drag area increases form a small value to 100% in a known, mathematically definable form. This method is mathematically exact, however, no drag area overshoot is included at the start of the reefed or disreef inflation cycle.

In this method it is defined a dimensionless parameter, which is obtained from known data and is called *ballistic parameter*, $\boldsymbol{A}$.

$$A = \frac{2\,W}{(C_D S)_P \, \rho \, g \, v \, t_f} \tag{3.12}$$

Where:

- A is the ballistic parameter.
- W is the system weight.
- $(C_D S)_P$ is the drag area.
- g is the acceleration of gravity.
- ρ is the air density at altitude of parachute inflation.
- v is the velocity of descend.
- t_f is the canopy inflation time.

W, g and $(C_D S)_P$ are fixed values for each specific application. The filling time t_f can be calculated by the methods given in section 3.4.2.a, and the velocity of descend v can be measured. Before calculating the ballistic parameter, it is necessary to determine the shape of the drag-area-versus-time curve, that is denote by the letter n: the n=1 curve is a straight line, typical for ribbon and ringslot parachutes; the concave curve, n=2, is representative of solid cloth, flat circular, conical and extended-skirt parachutes; and the convex form is for reefed inflation of extended-skirt parachutes. Once the value of the ballistic parameter is calculated, the force factor X_1 can be obtained from the graph in Figure 3.17.

In the case of the opening-force coefficient, the table of the Appendix A presents values of C_X, for a variety of unreefed parachute types operating under infinite mass inflation conditions; these values range from a high of 1,8 for a solid flat canopy to a low of 1.0 for a hemisflo ribbon canopy. Since there is little drag overshoot for a reefed parachute, a value of C_X of 1.0 should be used for inflation to a reefed stage.

Finally, the opening force of the parachute can be calculated using the equation (3.11)

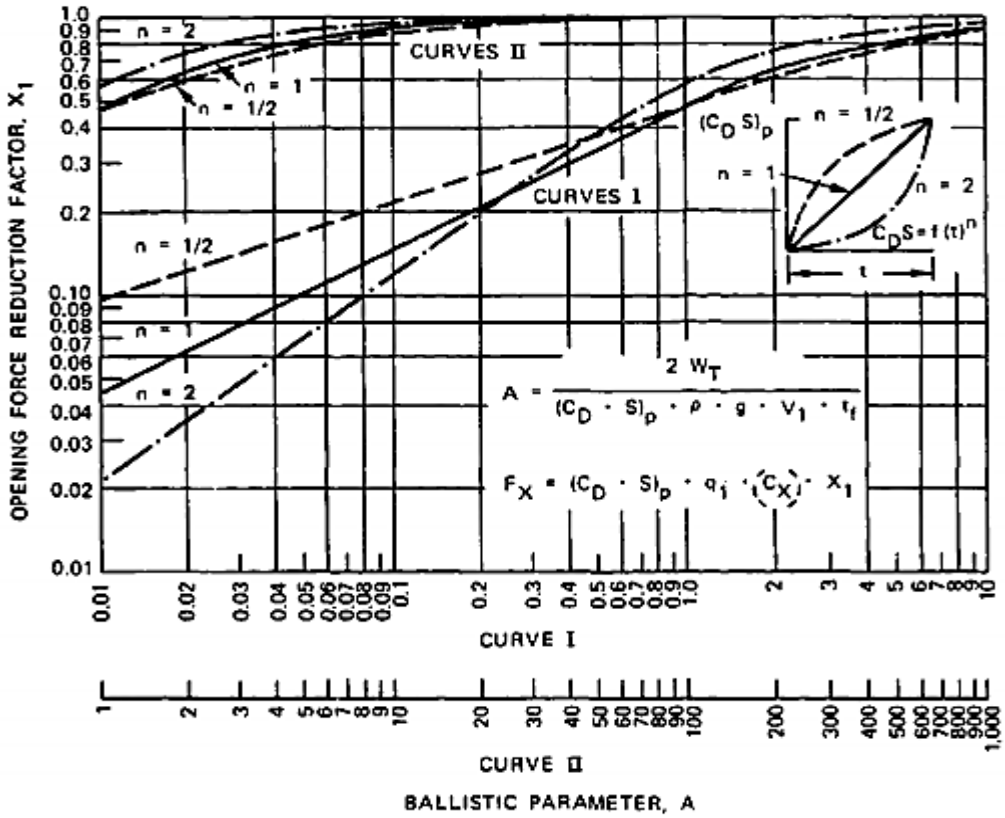

Figure 3.17. Opening-Force Reduction Factor versus Ballistic Parameter [2].

3.4.3. Altitude effects

A parachute dropped at a certain speed but different altitudes may have greater opening forces at higher altitudes than at low altitudes. This phenomenon occurs in particular when the parachute system has a low canopy loading, which causes the value of the ballistic parameter to take small values in the range between 0-10. As it can be seen in the graph of Figure 3.17, this range of values results in a highly variable opening force reduction factor, which can take lower values when the altitude is low or higher values when the altitude is higher. Consequently, as we saw in the equation (3.11), if the force reduction factor varies, the opening force also varies proportionally.

However, we can also observe in the graph of Figure 3.17 that for a range of values of the ballistic parameter between 10 and 1000, the value of the opening force reduction factor hardly varies with the altitude, and therefore the opening forces also do not vary. In this case, this phenomenon occurs when the loading canopy is high.

Figure 3.18 shows tests made by the Air Force in the 1950s at altitudes up to 6000 m with different canopy loadings and a high velocity of 102 knots (52.5 m/s) [13]:

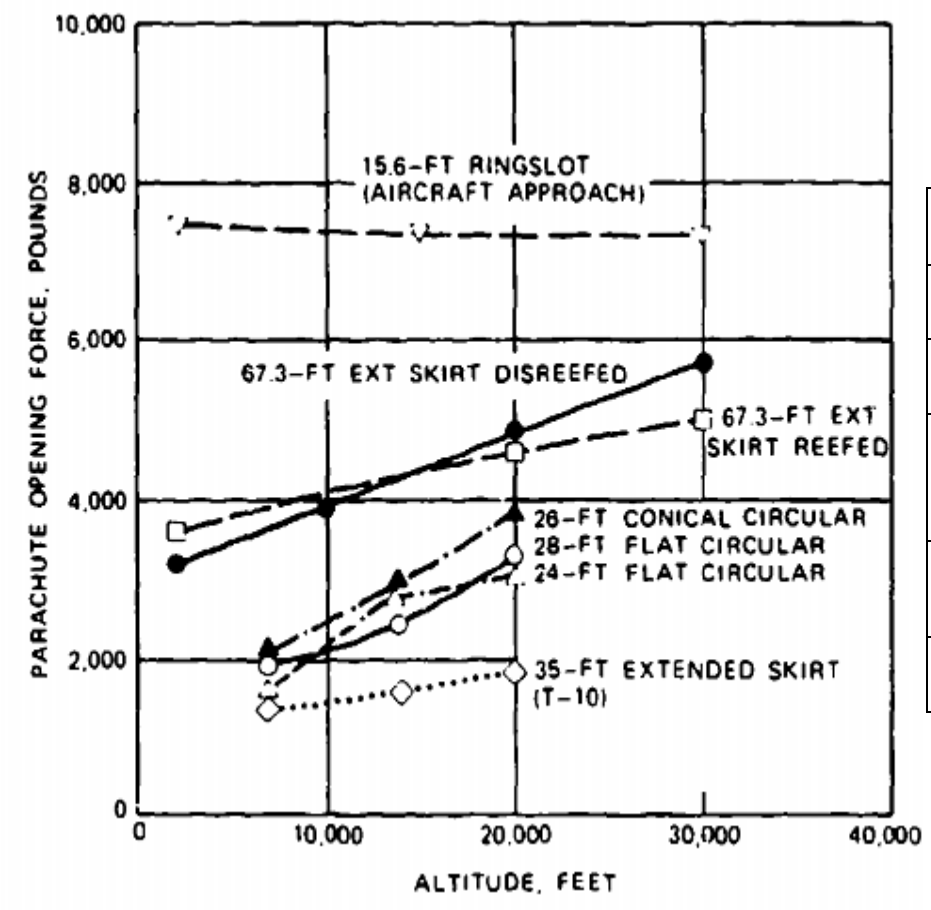

Parachute type	Canopy loading
Extended-skirt (Personnel)	~ 0.35
Flat circular (Personnel)	~ 0.5
Extended-skirt disreefed (Target drone recovery)	~ 0.6
Extended-skirt reefed (Target drone recovery)	~ 90
Ringslot (Aircraft approach)	~ 1200

Figure 3.18. Parachute Opening Forces as function of altitude for various types of Parachutes [13].

3.4.4. Porosity effects

The porosity of parachute canopies influences parachute characteristics and parachute performance. For parachute canopies manufactured form solid fabric, the nominal porosity was defined by Heinrich [27] as the volumetric airflow per unit area of material per unit of time ($ft^3/ft^2/s$ is commonly used). For slotted canopies such as ribbon, ringslot and ringsail parachutes, geometric porosity is defined in percent as the ratio of all open areas to the total canopy area (typical values are in the 10 to 35 % range).

Porosity affects parachute drag, stability and opening forces. The porosity increase makes the opening forces and oscillation smaller, that is desirable, but also makes the drag smaller, that is generally undesirable.

Figure 3.19 shows the effect of the porosity on drag coefficient of 3.5-foot-diameter flat and conical ribbon parachutes [14]. As it can be seen, the drag coefficient decreases and oscillation decreases when the porosity increases. Therefore, to maintain the proper performance of the parachute, it is necessary to reach a compromise between the required minimum drag and the accepted maximum oscillations.

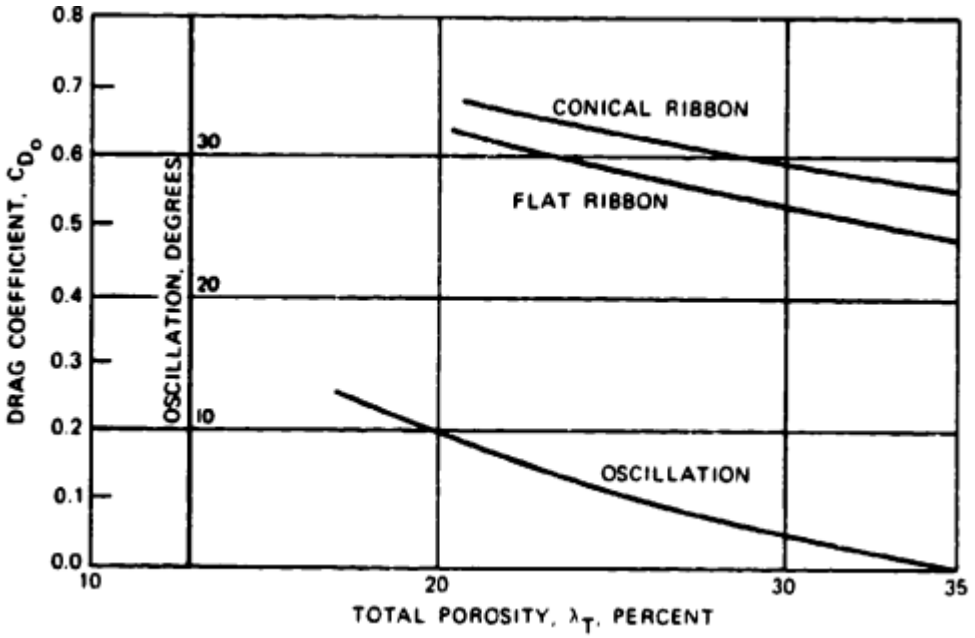

Figure 3.19. Drag Coefficient and Oscillation as a function of Total Porosity for 3.5 foot-diameter flat and conical ribbon parachutes [14].

3.4.5. Canopy shape and pressure distribution

The inflated shape of a parachute canopy depends on the type and geometric design of the canopy, on the canopy porosity, and on the suspension-line length. These factors are responsible for generating a certain balance of internal pressures forces and the tension in the suspension lines, which directly affects the instant shape of the canopy.

A decrease in canopy porosity and an increase in suspension-line length are the prime reasons for an increase in inflated canopy diameter and associated increase in drag coefficient. In Figure 3.20 it can be observed an example of the variation of the shape respect to the increase of canopy porosity and Figure 3.21 shows the canopy diameter variation respect to the line-ratio increase (l_e/D_0) .

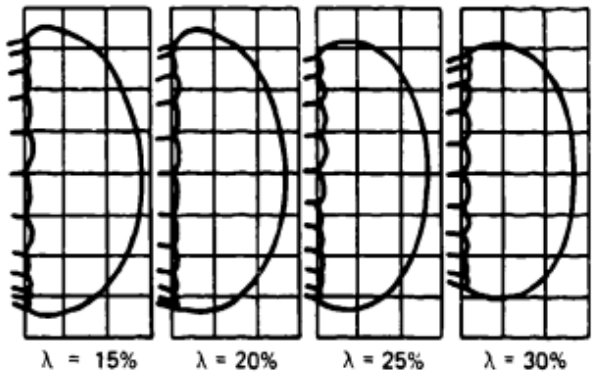

Figure 3.20. Parachute canopies with constant suspension-line ratio and porosities from 15 to 30%

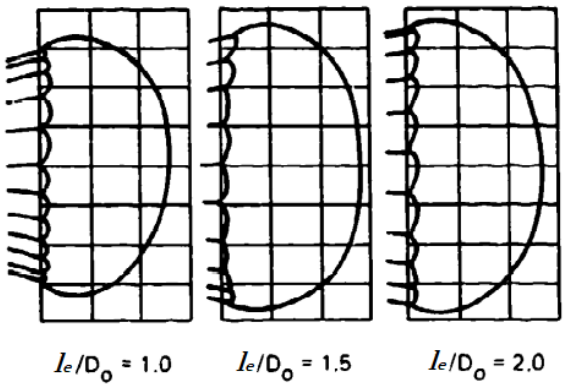

Figure 3.21. Parachute with constant porosity and Suspension line ratios of 1.0, 1.5 and 2.0 [2].

In regard to the pressure distribution over the parachute canopy is important to know the inflation characteristics of the canopy in order to determine canopy stresses. The desirable condition for parachutes is to keep a uniform airflow separation around the leading edge of the canopy and a uniform wake behind the canopy for obtaining high drag and good stability. As Figure 3.22 shows, the airflow in front of the canopy is decelerated to zero at the *stagnation point* (I) . Behind the stagnation point, turbulent airflow occurs, resulting in a high static pressure inside the parachute canopy compared to the static pressure in the undisturbed flow of the free airstream around the canopy. The airflow around the edge of the canopy is accelerated by the compression of the streamlines, causing a negative pressure difference on the outside of the canopy. The positive inside pressure difference and the negative outside pressure difference form a strong pressure gradient outwards that keeps the canopy inflated.

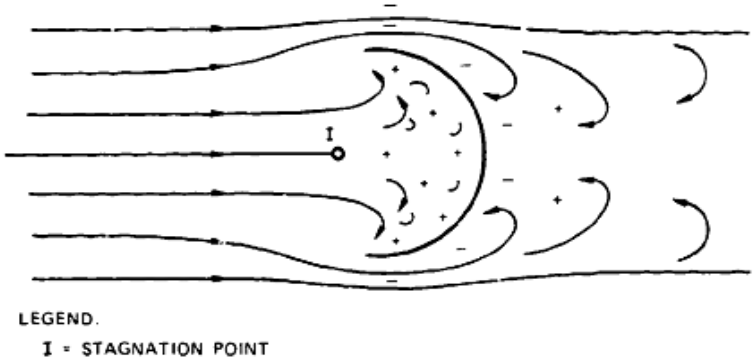

Figure 3.22.
Airflow and pressure distribution around a parachute canopy. [2]

3.5. Clustering of parachutes

A parachute cluster consists of two or more parachutes used to stabilize, decelerate or lower a payload. The use of this clustering basically depends on the mission, which must take into account both the advantages and disadvantages that entails.

On the one hand several small parachutes are easier to fabricate, store, maintain, handle and retrieve than a single large parachute. During its performance, they also have less probability of a catastrophic system failure than a single one and provide a stable descent even when using individual, high-drag, unstable parachutes. Another important advantage during its performance is that a parachute cluster has a shorter filling time than a single large parachute.

On the other hand however, it is impossible to obtain a perfectly synchronized opening of all parachutes in a cluster. For this reason each parachute in the cluster must be designed to handle the maximum individual load. Therefore, the total strength of the parachutes in a cluster and their associated weight and volume are higher than the weight and volume of a single large parachute of equivalent drag area and because of the interference and systems geometry, they also experience a reduction in drag, although its effect is less aggressive.

3.5.1. Loss of Drag in Cluster Applications

Parachutes combined into clusters suffer a reduction in drag because of the geometry of the cluster system, which forces parachutes to fly at a large angle of attack. However this problem can be reduce using longer suspension lines to decrease the individual angle of attack and thereby increases the cluster drag. Another reason of reduction in drag also happens because of mutual interference, but this reason is less aggressive than the previous one.

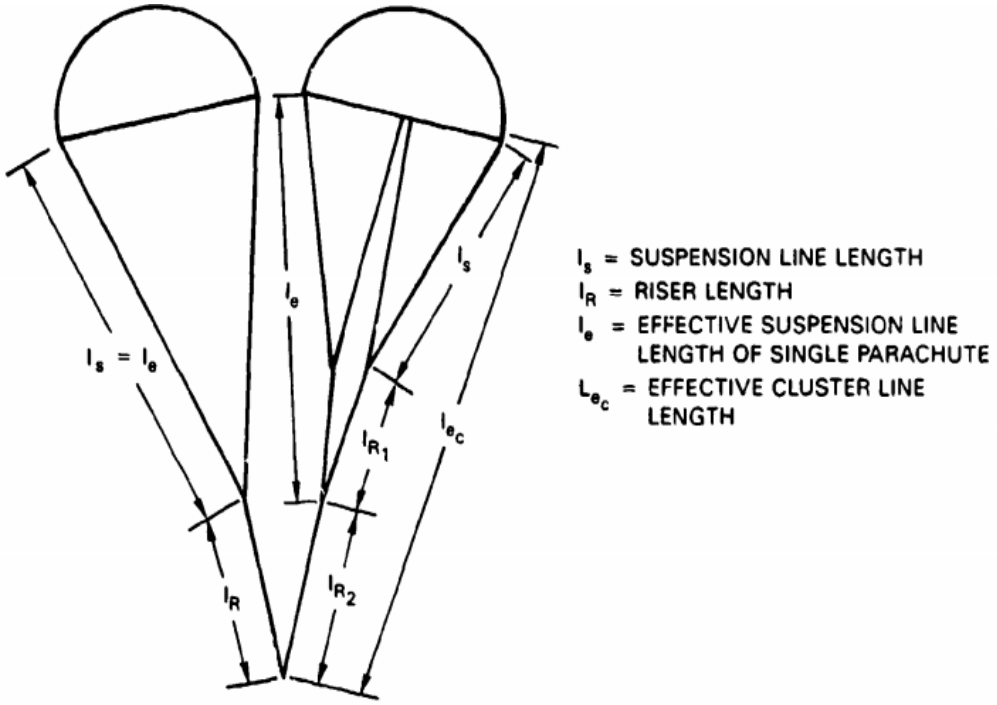

Figure 3.23. Typical Parachute Cluster Arrangement [2].

Figure 3.24 shows a group of parachutes of different types and different sizes, whose drag coefficient decreases as the number of parachutes in the cluster increases.

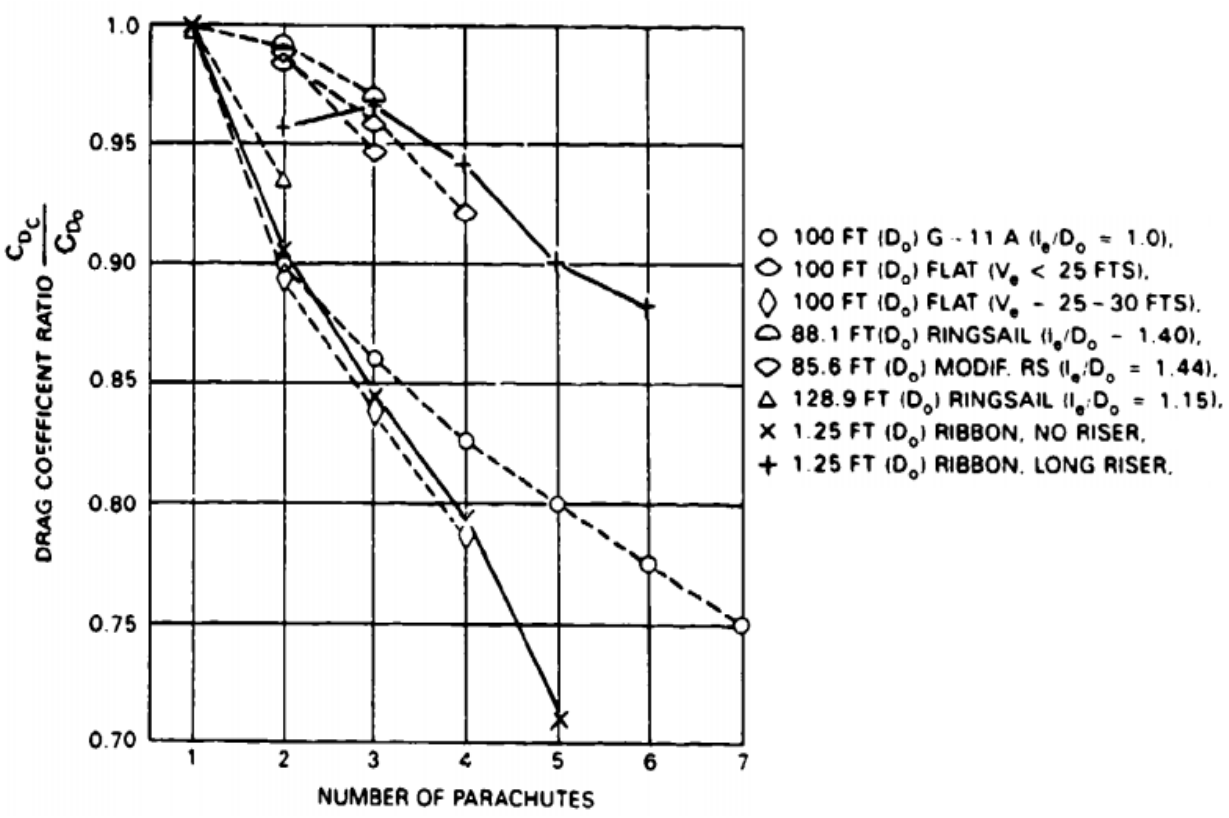

Figure 3.24. Drag loss in Parachute Clusters [2].

3.5.2. Synchronization problems

The problems of synchronization can occur if one of the parachutes of the cluster inflates ahead of the others, since the velocity and dynamic pressure decreased so rapidly that the remaining pressure is not enough to inflate the lag parachutes. This is considered a catastrophic failure because the early inflated parachutes can be destructed by the supported overload.

To avoid this problem the reefing technique is used. Reefing the individual parachutes in the cluster allows all parachutes to obtain an initial inflation followed by a reasonably uniform full inflation and inflation forces.

3.6. Supersonic parachutes

The supersonic flow around a parachute canopy is different form the subsonic flow around them. The use of parachutes in the supersonic regime is limited due to performance, stability and structural concerns to applications such as missile recovery, Mars entry-systems and ballistic nose cone recovery.

Recent experimental and analytical work with subscale parachutes in supersonic flight has shown that for operations above Mach 1.2 it exists an instability as a result of the fluid-structure interaction between the flow-field and the canopy [15]. This instability is driven by aerodynamic coupling of the parachute bow-shock and forebody wake, and is dependent on Mach and proximity and shape of the forebody.

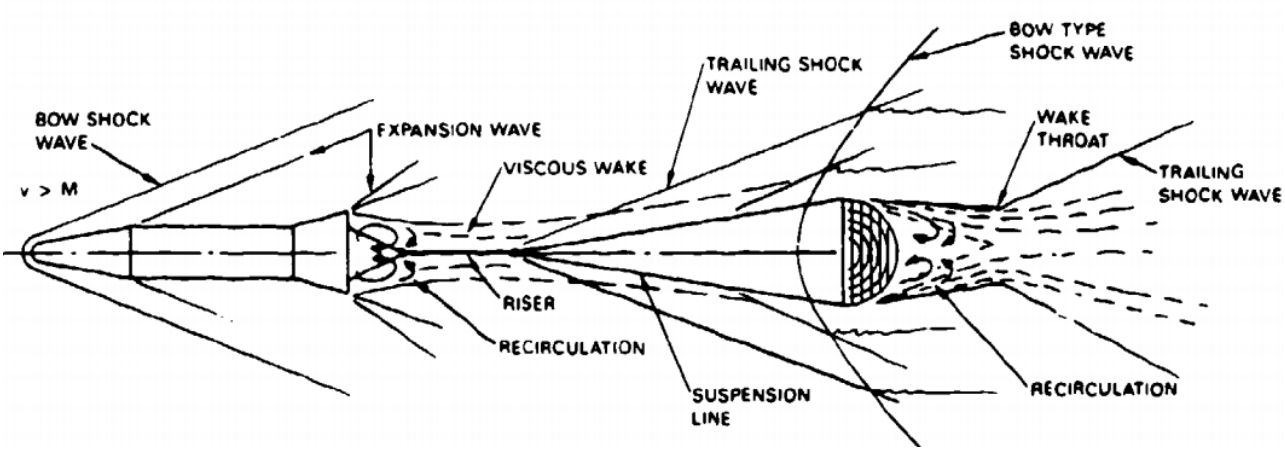

Figure 3.25. Supersonic flow around a Vehicle-Parachute System [16].

Supersonic parachute aerodynamics was first investigated with subscale wind tunnel tests of ribbon parachutes form Mach 1 to 3 [17]. These studies revealed lateral and inflation instabilities as a function of Mach number and canopy porosity, and manifested that at Mach numbers above 1.2 a supersonic breathing phenomenon appeared for parachutes flown in the wake of a bluff-body vehicle. Figure 3.26 shows that the instability is characterized by periodic collapse and re-inflation events that result in dynamic loading, projected area variation, and in some cases parachute structural damage or failure.

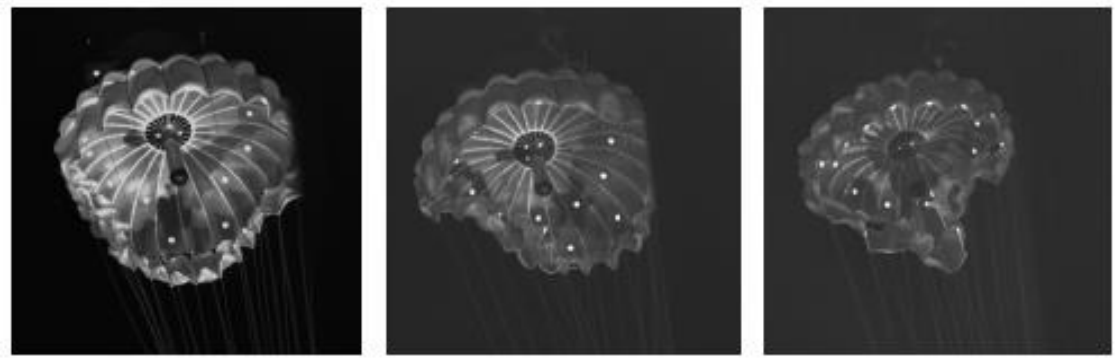

Figure 3.26. Instability at Mach 2.0, 2.2 and 2.5 for a 26-ft-Disk-Gap-Band Parachute [17].

This supersonic instability is usually known as the *Squidding phenomenon*, by its similarity to the movement of a squid. The momentum deficit of the subsonic wake of the forebody causes the parachute's bow-shock to change in shape, move forward, and reduce mass flow into the canopy. During this time the canopy depressurizes and partially collapses, disrupting the primary bow-shock ahead of the canopy. Then the canopy re-pressurizes and the bow-shock is re-established. This process repeats cyclically at a frequency on the order of the acoustic frequency. Figure 3.27 shows the high-speed shadowgraph sequence of a 26-ft-DGB parachute at Mach 2.0, where the oscillatory motion of the bow-shock is clear and is also evident the shocks generated by the suspension lines.

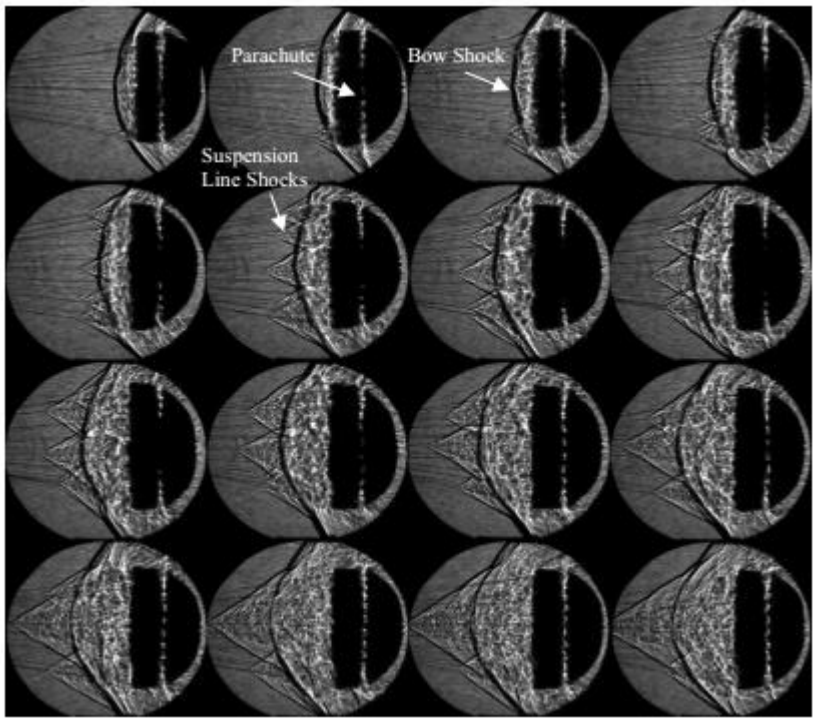

Figure 3.27. Progression of fluid interaction of a Disk-Gap-Band parachute [17].

Regarding to the velocity dependence, when the Mach number increases, parachute drag efficiency reduces, as well as the canopy dynamics increases. This is correlated with a more chaotic bow-shock oscillation and more turbulent wake contribution to the bow-shock coupling. As the Figure 3.28 shows, the drag coefficient of the considered parachutes doesn't increase while approaching Mach 1, but after Mach 1.2 the drag coefficient decreases, because of the gradual decrease in inflated parachute diameter. It can also be observed that hemisflo and hyperflo parachute canopies exhibit less breathing, flutter and decrease in inflated diameter with increasing Mach number than do flat and conical parachutes because of their spherical design distributes better stresses in case of asymmetric dynamic loads.

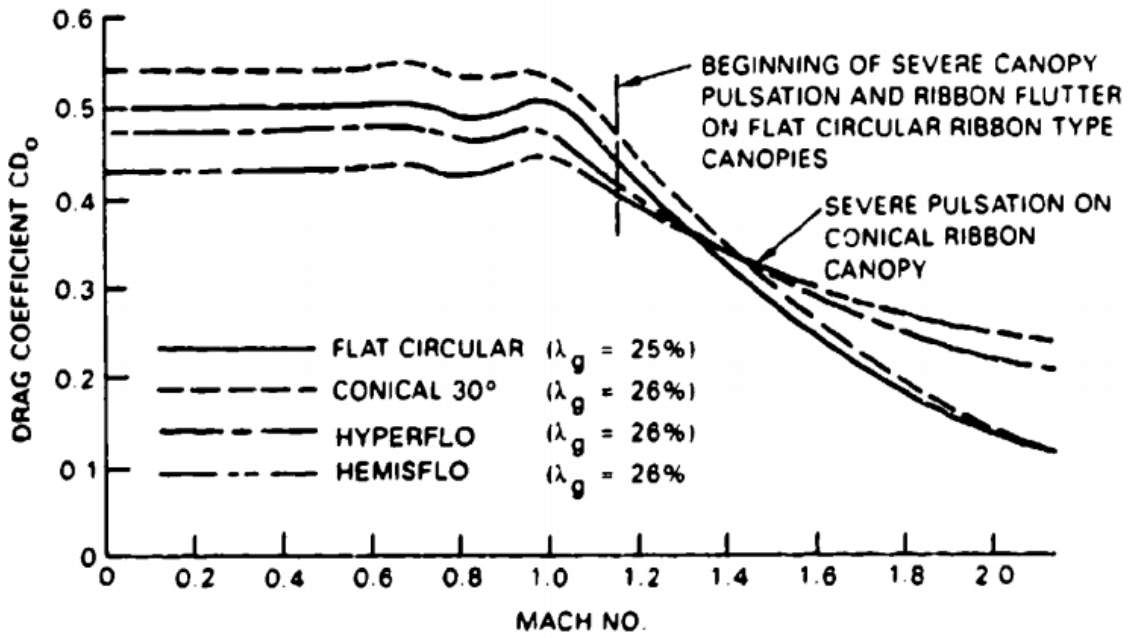

Figure 3.28. Drag Coefficient of several parachutes as function of Mach number [16].

The shape, scale and proximity of the parachute and bluff-body vehicle affect parachute performance. The ratio of vehicle diameter to parachute nominal diameter (d/D_0) is a measure of the contribution of the wake to the fluid-structure interaction. The non-dimensional trailing distance (x/d) is defined as the axial distance between the parachute leading-edge and the vehicle maximum diameter. Knowing this, wind tunnel tests [16] demonstrated that an increase in d/D_0 tends to reduce the flow field unsteadiness and similarly, an increase in trailing distance reduces the coupling of the wake to bow-shock and the drag coefficient is higher. Therefore, in the limit of $x/d \rightarrow \infty$ or $d/D_0 \rightarrow 0$, the effective vehicle diameter approaches zero, i.e. the flow field approaches that of the parachute without an upstream wake contribution.

In general, the flow-dynamics is strongly associated with the parachute geometric parameters and is dependent on the degree of coupling between the wake and parachute bow-shock. Thereby, the selection of an appropriate trailing distance can reduce coupling, but it must be traded with an orderly deployment process, parachute inflation time, and multibody dynamics considerations.

CHAPTER 4: Application. Parachute design for the recovery of a rocket's first-stage

In this section the concepts developed in the previous chapter will be applied to a real case of recovery of the first stage of a rocket, which as we saw in the first chapter, the recovery and subsequent reuse of the components of a rocket has become a very important aspect for future space transport systems. Thus, from the data compilation of the mission of this real case we will be able to make a preliminary design of the recovery system of the first stage of the rocket. Therefore, through performance and system analysis we can choose which type of parachute to select for high-speed deceleration and for final recovery. We will try to verify as much as possible the design considered with the real design, but of course we must take into account that different engineers may make different selections based on experiences with particular types of parachutes.

4.1. Ares I-X: Overview and General data

The rocket selected to make the preliminary design of the recovery system is the Ares I-X, since in it we find a recovery system based on parachutes in which we can apply properly the concepts studied in the last chapter.

Ares-I is one of the first rockets of the next-generation space transportation systems developed by NASA's Constellation Program to deliver explorations beyond the low Earth orbit. The first flight test of this Program, known as Ares I-X, was on October 2009 and provided NASA an opportunity to test and prove hardware, models, facilities and ground operations associated with the Ares I launch vehicle. This flight test vehicle was built to demonstrate the flight control system performance during ascent and gathering information to help engineers to find a final design of the Ares-I vehicle.

The Ares I-X vehicle consisted of two main parts: a functional five-segment solid rocket booster stage (First Stage, FS) and an Upper Stage (US).

The US consists of eleven segments: two interstage segments, two ballast segments, five "common" segments, and the spacecraft adapter and service module. These together account more than 30 meters of the total 99.6-meter vehicle height and almost 205,000 kilograms of the Ares I-X vehicle's lift-off weight.

The FS is approximately 53 meters in length and is responsible for lifting the entire Ares I off the ground toward Earth orbit. It comprises a five-segment solid rocket booster. It has an aluminium aft skirt, which provides structural support for the vehicle and a forward skirt extension that contains the avionics system and the parachute recovery system. The frustum which is made of a composite material, interfaces with the US and contains the aeroshell, which houses the pilot and drogue parachutes.

Figure 4.1 shows a scheme of the different important parts of the Ares I and Table 4.1 lists some information gathered about the mass properties and dimensions of Ares I:

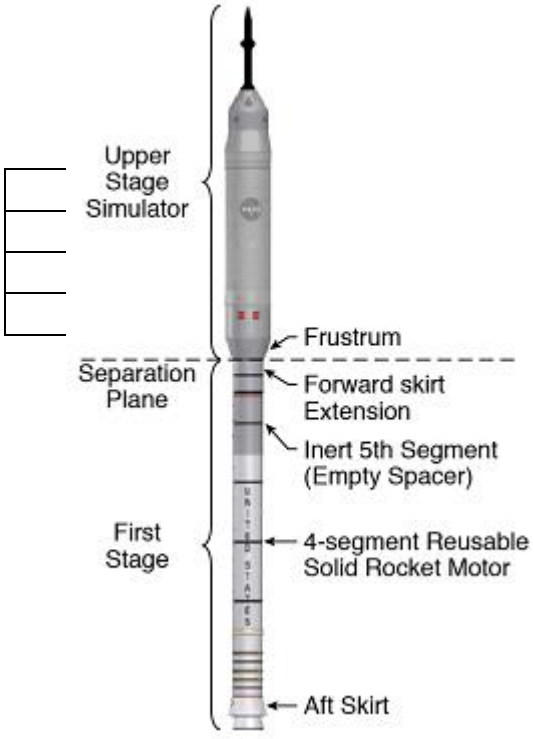

Figure 4.1. Ares I Elements [18].

ARES I-X General	
Length	99.6 m
Diameter	5.5 m
Total Mass	803.5 tons
Upper Stage	
Length	46.9 m
Diameter	5.5 m
Total Mass	220 tons
First Stage	
Length	52.7 m
Diameter	3.7 m
Total Mass	583.5 tons
Empty Mass	126.2 tons

Table 4.1. Dimensions and Mass properties [18].

4.1.1. Flight Performance

At launch, the thrust produced by the engine is greater than the weight of the rocket and the net force accelerates the rocket away from the pad. Leaving the pad, the rocket begins a powered vertical ascent. The vehicle accelerates because of the high thrust and decreasing weight and rather quickly moves out of the thick atmosphere near the surface of the Earth. Although the rocket is traveling supersonically, the drag on the vehicle is small because of the shape of the rocket and the lower air density at higher altitude. As the rocket ascends, it also begins to pitch over and its flight path becomes more inclined to the vertical.

After approximately two minutes into the ascent, the propellants burn off and the first stage becomes a near-empty tankage and must be discarded to allow the rest of the vehicle to continue its ascent trajectory. This process is called staging. The discarded first stage continues on a ballistic flight back to the Earth. At this point we will focus only on the trajectory of the first stage and it will be described in more detail [18].

Staging of the Ares I-X occur near Mach 4.6 at an altitude of 40,000 meters and a dynamic pressure of 4.8 kPa. The Ares I-X separation plane is located at the base of the frustum. At staging, eight Booster Deceleration Motors (BDMs), located on the FS aft skirt, are ignited to reduce the velocity of the FS relative to the US. During this time the FS moved primarily in an axial direction relative to the US. Three seconds after staging, four Booster Tumble Motors (BTMs), also located on the aft skirt of the FS, are ignited to induce a tumbling motion predominantly about the negative yaw-axis in order to increase drag and reduce re-entry dynamic pressure. Both the BDMs and BTMs have short (~3 seconds) burn times, and the FS subsequently descend, unpowered and uncontrolled, until parachute deployment.

For the first 15-20 seconds after staging, the FS is in the wake of the US and thus is subjected to aerodynamic interference effects. The FS reach an apogee altitude of approximately 46,000 meters nearly 38 seconds after staging and 90 seconds later (130 seconds after staging) it reach a maximum dynamic pressure (max-q) of 42 kPa at an altitude of 16,600 meters.

Once the FS descend to an altitude of approximately 4,500 meters the FS nose cap is jettisoned, releasing a pilot chute that deploys the drogue parachute with 20 meters of nominal diameter. The drogue parachute reaches full inflation, decelerating the FS and orienting it into a tail-first attitude. Then, the main parachutes (45-m nominal diameter each one) are deployed as the forward skirt extension (FSE) is separated [18].

Figure 4.2 shows a sketch of the recovery trajectory of the first stage:

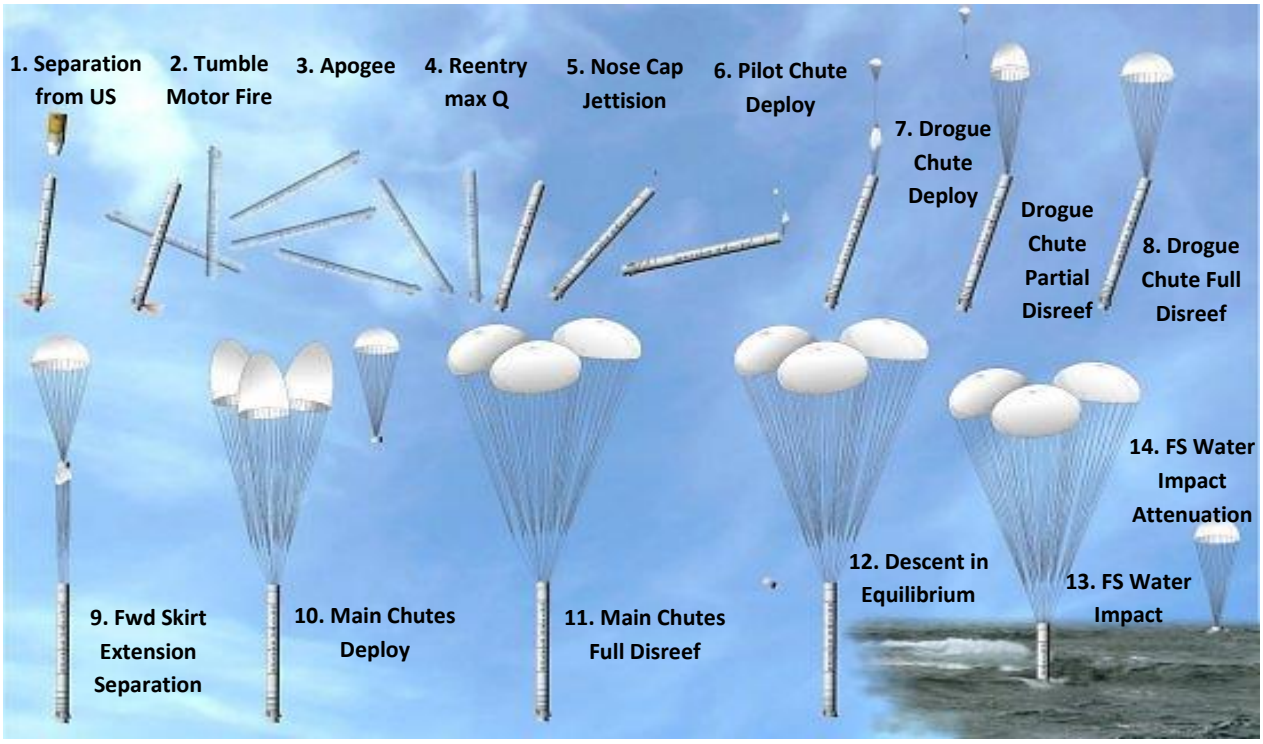

Figure 4.2. Recovery Trajectory of the first stage [19].

FIRST STAGE RECOVERY	Time (s)	Altitude (m)	Velocity (m/s)	Dynamic Pressure (Pa)
1. First Stage Separation.	0	40107.41	1487.42	4500.74
2. Tumble Motor Fire.	3	41483.28	1475.23	3638.9
3. Apogee.	38	46664.88	1368.55	1580.05
4. Reentry Max q.	128	16672.56	710.18	42134.62
5. Nose Cap Jettision.	191	4660.392	160.02	9576.05
6. Pilot Chute Deploy.	192	4553.712	160.02	9671.81
7. Drogue Chute Deploy.	194	4206.24	157.89	9767.57
8. Drogue Chute Full Disreef.	206	2560.32	118.87	6511.71
9. Fwd Skirt Extension Separation.	216	1371.6	103.63	5601.99
10. Main Chutes Deploy.	218	1143	117.35	7325.68
11. Main Chutes Full Disreef.	231	347.472	31.09	574.56
12. Descent in Equilibrium.	236	228.6	21.64	335.16
13. FS Water Impact.	245	0	21.64	335.16
14. FS Water Impact Attenuation.	306	0	12.19	95.76

Table 4.2. Events based on predicted nominal performance, unless otherwise noted [19].

From Table 4.2 it can be represented the following graphs that show the characteristics on the behaviour of the Recovery System of Ares I-X's first stage.

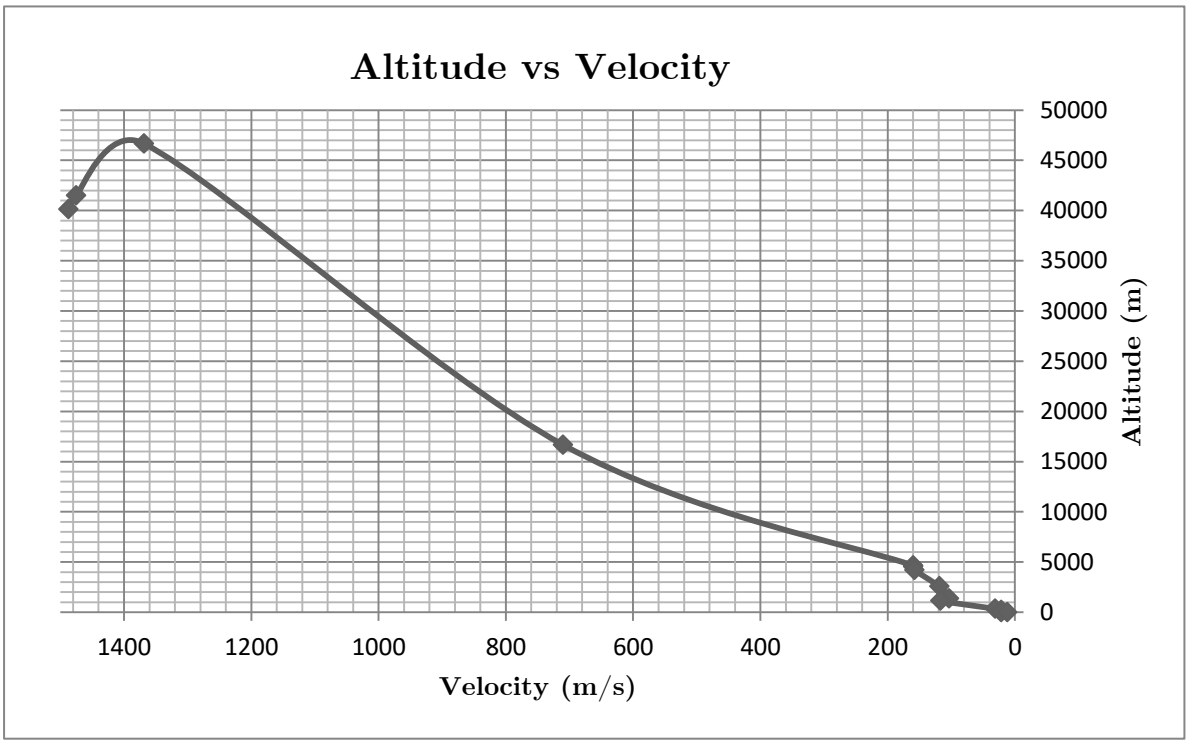

Figure 4.3. Altitude vs Velocity curve of Ares I-X performance data from Table 4.2.

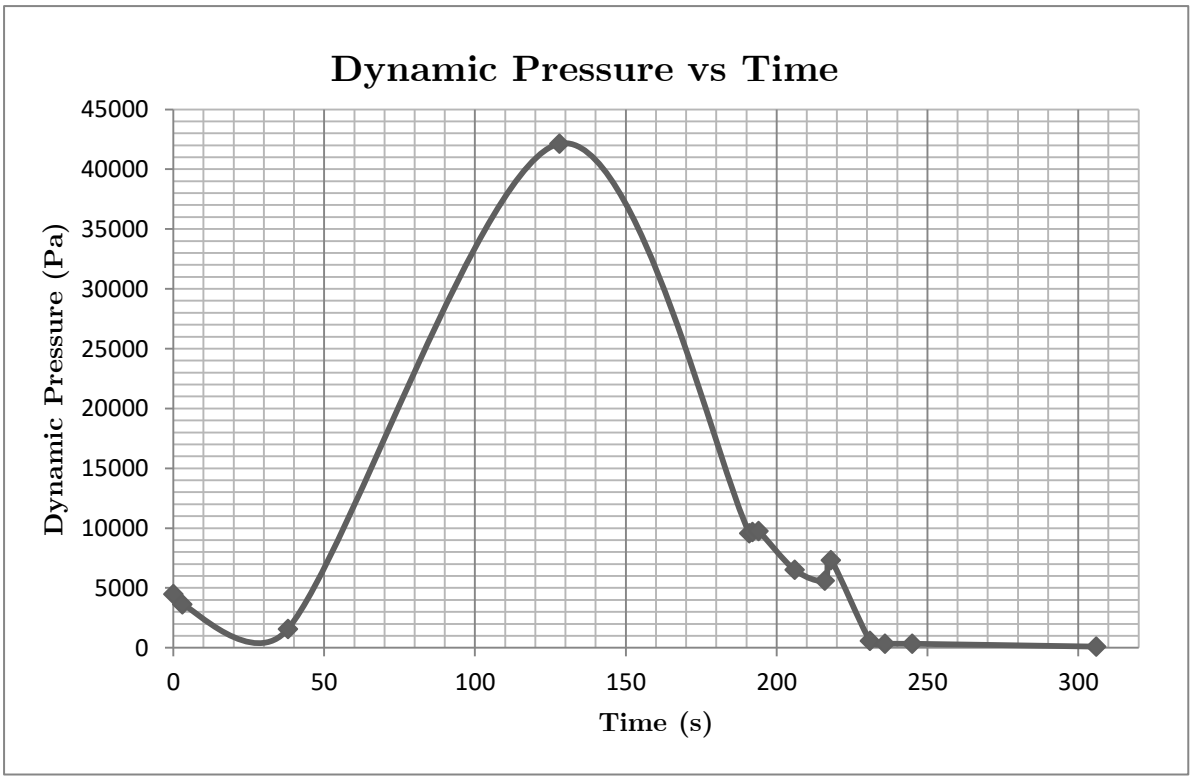

Figure 4.4. Dynamic Pressure vs Time curve of Ares I-X performance data from Table 4.2.

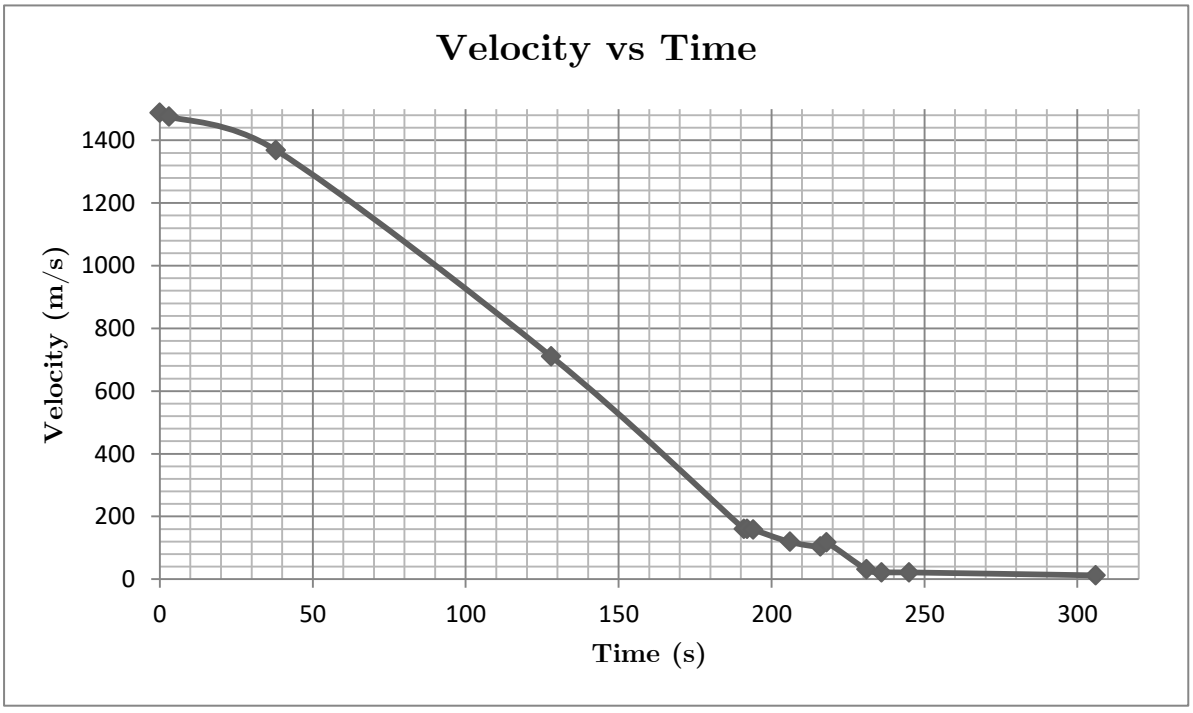

Figure 4.5. Velocity vs Time curve of Ares I-X performance data from Table 4.2.

If an increase of Figure 4.3 is made, we can observe in greater detail the behaviour of the first stage of the rocket when the parachute recovery system is activated.

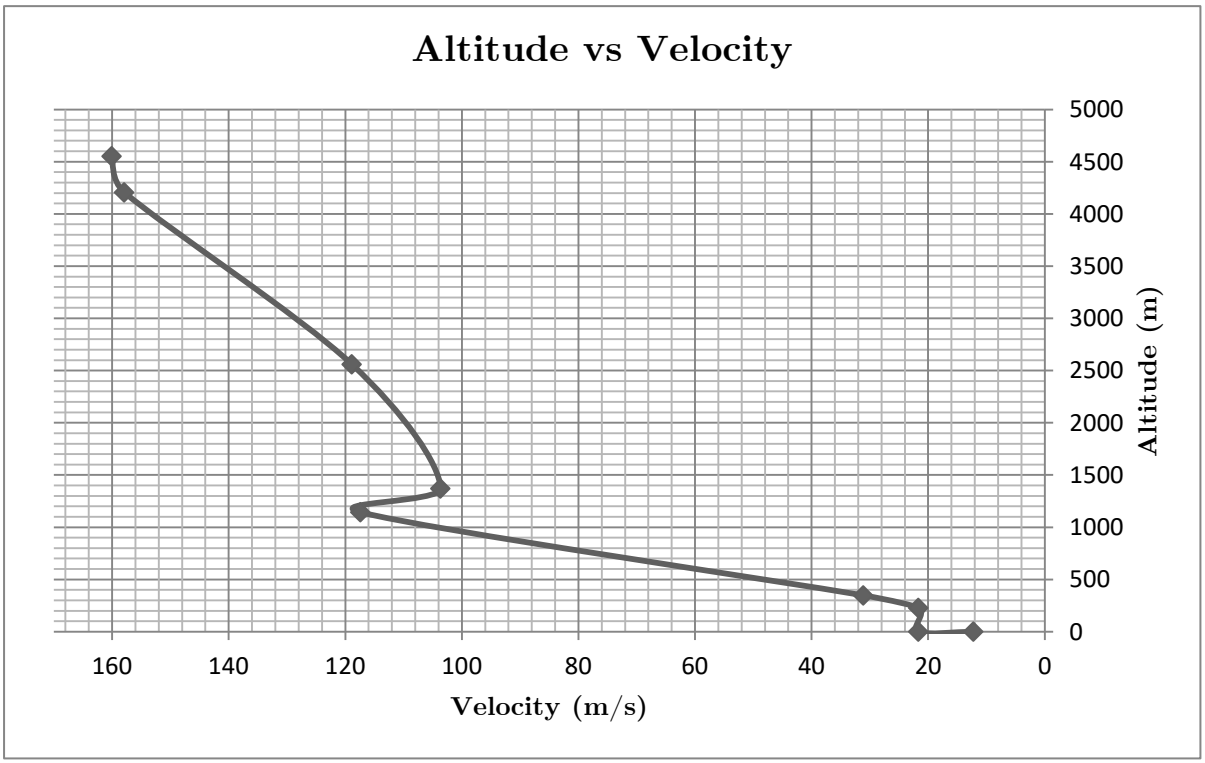

Figure 4.6. Enlargement of Altitude vs Velocity curve of Ares I-X performance.

We can distinguish mainly three different phases according to this graph.

First, a rapid descent is made to an altitude of about 1400 meters. In this phase is precisely where the pilot chute followed by the drogue chute deploys. The latter is capable of decelerating the vehicle to about 35% in less than 25 seconds.

Next, a sudden increase in speed is observed due to the transition between the separation of the drogue chute and the deployment of the main parachutes. As expected in this transition there is no decelerator element and therefore the speed increases to 13% in a period of 2 seconds.

The second phase, in which the parachutes are reefed, a lower descent is observed, since the reefed parachutes offer more drag than the drogue chute, and consequently the rate of descent is smaller. Thus it is possible to reduce the speed more than 80% with respect to the speed before the deployment of the parachutes.

Finally, in a third phase, it is observed that the speed remains constant with the altitude. This is because the main parachutes are completely disreef and reach a state of equilibrium in the descent.

4.2. Parachute Recovery System Design

In this section, a preliminary design will be made of the parachute system described in the previous section, used for the recovery of the first stage of Ares I-X rocket. For this, the design concepts described in Chapter 3 will be applied, with which we will be able to obtain certain characteristic values of the parachute system and its performance. Some of these values can be compared with the values of the real case and therefore we can verify the degree of adequacy of these procedures as a tool to obtain a suitable preliminary design. On the other hand, in those cases where veridical information is not available in the specific case, we will simply try to apply the necessary procedures to obtain the values that characterize the parachute and based on the experience of other designs, we will discuss the validity of the results obtained.

4.2.1. Main Parachute System Design

a) Nominal Diameter:

The main objective of the main parachute system is to decelerate the vehicle in its last descent phase, period in which the load is already stabilized at a low altitude and a relatively slower speed.

First, to try to approximate as much as possible the design calculations with the real main parachute system, we will select a cluster of three Ringslot parachutes. Anyway this choice can be justified.

On the one hand, the decision to use a parachute cluster instead of a single one is mainly due to the safety they offer, since it is less probably that a catastrophic failure could occur. Besides this, the cluster reduces the inflation time of the parachute and its manufacture is much simpler.

On the other hand, among the possible types of parachute shown in appendix A, the Ringslot parachute proves to be one of the most suitable choices under these operating conditions. Experience has shown that this type of parachute worked successfully as a final recovery parachute and also because of its lighter weight, good drag coefficient, slower inflation rate (thus lower opening-shock load), and improved stability compared to other canopies.

The size of the cluster is determined by calculating the total effective drag area required. For this, it is necessary to select the required rate of descent, when the main parachutes are full opened and thus in equilibrium descent. In this application, the selected rate of descent must be 21.7 m/s at an altitude of 230 m (see Table 4.2).

$$m_{FS} = 126.2\ tons = 126200\ kg\ \text{(Table 4.1)}\,;\quad v_1 = v(z = 230m) = 21.7\ m/s \qquad (4.1)$$

Therefore, in equilibrium descent, the equilibrium dynamic pressure must be the same at both 230 m altitude and sea level. Knowing this, it can be obtained an expression of the rate of descent as a function of altitude:

$$q_e = \frac{1}{2}\rho(z)v^2 \quad ; \quad \rho(z) = \rho_0(1 - 22.57 \cdot 10^{-6}z)^{4.256} \quad ; \quad \rho_0 = 1.225\, kg/m^3 \tag{4.2}$$

$$\frac{1}{2}\rho(z = 230m)v_1^2 = \frac{1}{2}\rho_0 v_0^2 \quad \rightarrow \quad v_0 = v_1\sqrt{\frac{\rho_1}{\rho_0}} \quad ; \quad z_0 < z < z_1 \tag{4.3}$$

Applying equation (4.3), the velocity of descent at sea level is $v_0 = 21.5\, m/s$, which is a value very close to the value of the speed of descent acquired in the real case.

Considering that in equilibrium descent the total drag of the system is very nearly equal to its weight, the required effective drag area can be obtained.

$$W = D = (C_d S_0)\, q_e \quad \rightarrow \quad (C_d S_0) = \frac{W}{q_e} = \frac{2\, m_{FS}\, g}{\rho(z)v^2} \quad ; \quad z_0 < z < z_1 \tag{4.4}$$

In this case, the equilibrium dynamic pressure is $q_e = 282.102\, Pa$, and the total drag area is $(C_d S_0) = 4384.1\, m^2$, which is equivalent to an individual drag area for each main parachute of $(C_d S_0)_{1,2,3} = 1461.4\, m^2$.

Once the drag area of each parachute is determined, the nominal surface can be estimated and consequently the nominal diameter of each parachute of the cluster. At this point it is necessary to make an assumption about the drag coefficient of the parachute, since we don't have a real value of it. Considering that a ringsail parachute usually has a drag coefficient from 0.75 to 0.9 (see Appendix A), we can determine the drag coefficient of each parachute representing a correlation between the nominal diameter and the drag coefficient from data of different parachutes. These parachutes are ringsail type, but built with different diameters [20].

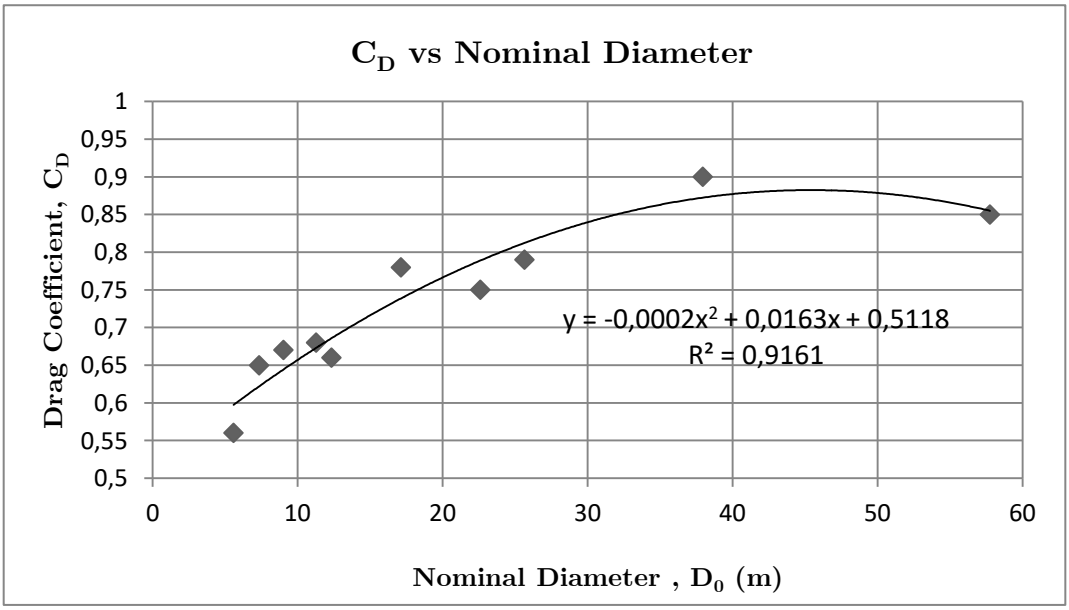

Figure 4.7. Typical drag coefficient versus nominal diameter for different sizes of ringsail parachutes [20].

According to the graph of Figure 4.7, a typical drag coefficient value for a parachute of 45 m in diameter is 0.84, but in a cluster of three parachutes there is a drag loss (section 3.5.1). Nevertheless this drag loss can be attenuated by lengthening the suspension lines (section 3.4.5). Figures 4.8 and 4.9, based on experimental data of different parachute systems, can give an idea of the percentage of drag change.

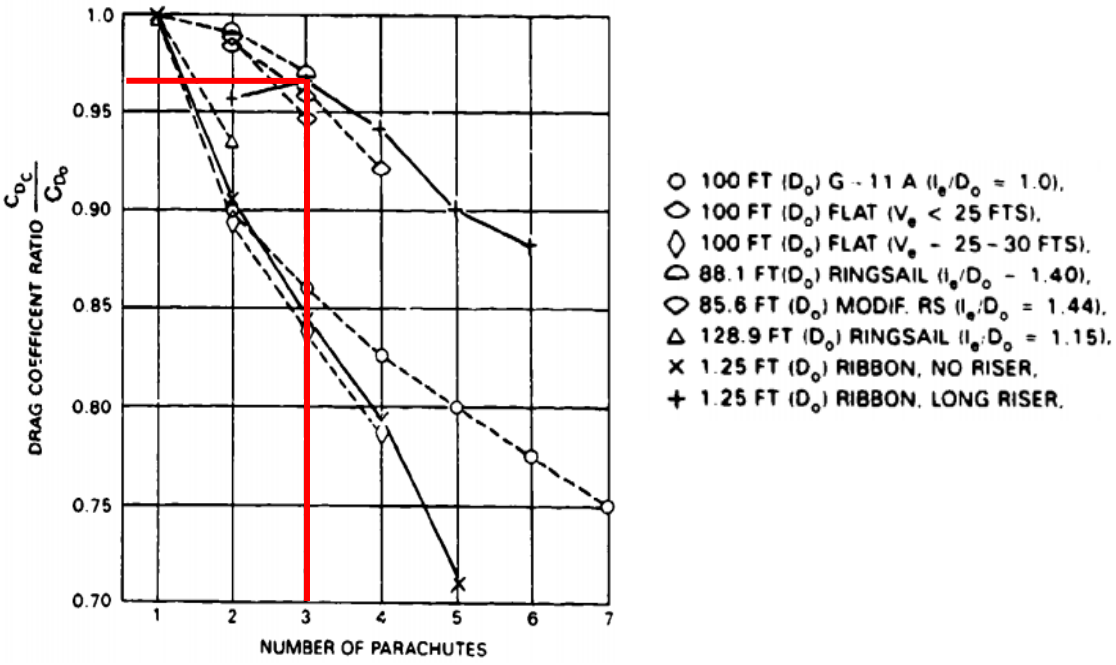

Figure 4.8. Drag loss in Parachute Clusters [2].

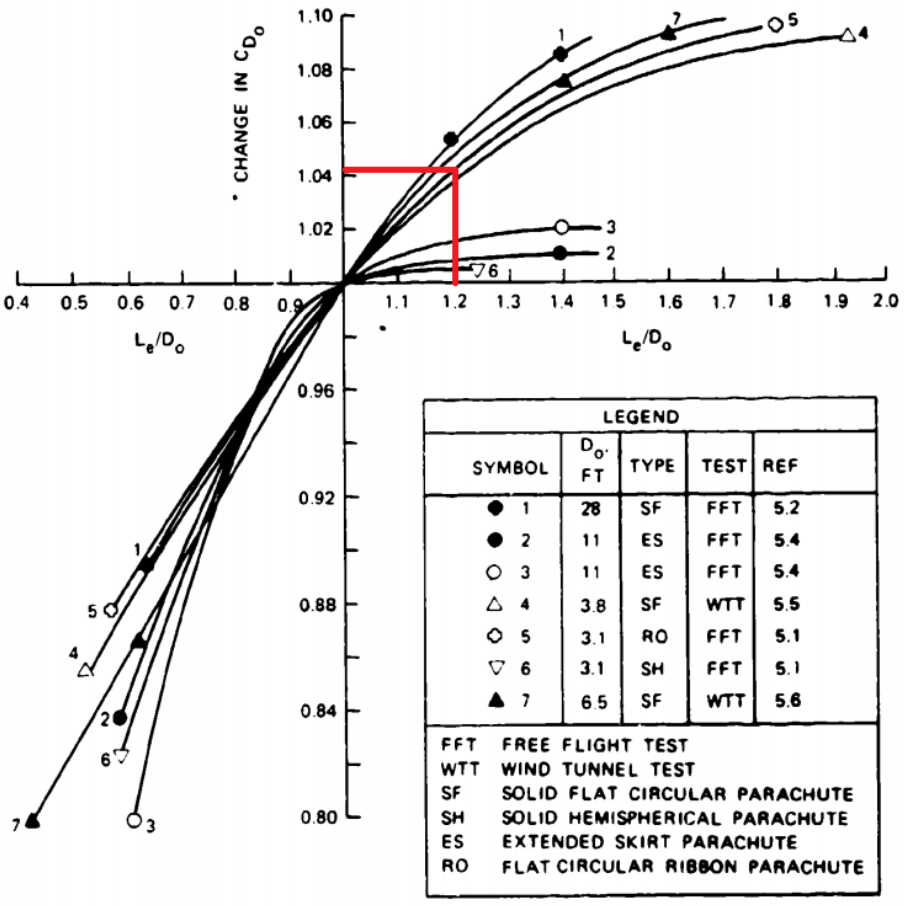

Figure 4.9. Variation of Drag Coefficient with Suspension Line Ratio [2].

As can be seen the percentage of drag loss is less than 5% for a cluster of three parachutes, and this drag loss can be almost recover with a ratio l_e/D_0 greater than 1.2. Therefore for this preliminary design, this issue doesn't mean a serious problem and can be obviated.

$$C_d = 0.84 \quad \rightarrow \quad S_0 = \frac{C_d S_0}{C_d} \quad \rightarrow \quad D_0 = \sqrt{\frac{4\,S_0}{\pi}} \tag{4.5}$$

Using these equations, for each canopy the nominal surface is $S_0 = 1739.1\,m^2$ and the nominal diameter is $\boldsymbol{D_0 = 47.05\,m}$. Comparing the latter with the nominal diameter of the parachutes used in the Ares's first stage (Section 4.1.1), it can be deduced that it is a practically identical value, and therefore the assumptions are correct.

b) Canopy Inflation Time:

In the final interval in which the main parachutes are deployed, two phases can be differentiated: reefed and disreefed phase. For this reason it is necessary to determine two inflation times for both reefed and disreefed stages.

Considering that during the reefed phase, the equation of motion is given by:

$$m\,\ddot{x} = mg - D_{FB} - D_P \tag{4.6}$$

Where D_P is the drag generated by the parachute ($\frac{\rho}{2}(C_D S_0)_R v^2$) and D_{FB} is the drag of the forebody. The drag generated by the forebody can be calculated by considering the flat plate analogy developed by Daniel P. Raymer [21]. This method consists of calculating the drag generated by a flat plate, and correcting the result by a shape factor (SF), which depends on the geometrical parameters that define the volume of the body, and therefore takes into account that the boundary layer becomes thicker and detaches compared to the flat plate.

$$D_{FB} = \frac{\rho}{2} S_{wet}\, v^2\, C_f\, SF \tag{4.7}$$

Where:

- ρ is the air density.
- S_{wet} is the wet surface of the forebody.
- v is the velocity of the forebody.
- C_f is the Friction Coefficient.
- SF is the Shape Factor.

According to Raymer, the Friction Coefficient C_f can be calculated as a function of the Reynolds number and the Mach number as follows:

$$C_f = 0.455\,(\log_{10} Re(D_0))^{-2.58}(1 + 0.144\,M^2)^{-0.65} \tag{4.8}$$

In this case the velocity is a variable, therefore we can express the equation (4.8) as:

$$C_f = 0.455 \left(\log_{10}\left(\frac{\rho\, v\, D_0}{\mu}\right)\right)^{-2.58} \left(1 + 0.144 \left(\frac{v}{c_S}\right)^2\right)^{-0.65} \tag{4.9}$$

Moreover, considering that the forebody has a cylindrical shape similar to an aircraft fuselage, Raymer proposes that the Shape Factor can be calculated as follows:

$$SF = \left(1 + \frac{60}{f^3} + \frac{f}{400}\right) \tag{4.10}$$

Where f is the ratio between the length of the forebody and its diameter, also known as slenderness (l_{FB}/d_{FB}).

Therefore the force of resistance of the forebody in the instant in which the main parachutes deploy ($v_R = 117.35\, m/s$ and $z_R = 1143\, m$ from Table 4.2) can be calculated.

From Table 4.1 we can obtained the values of length and diameter of the forebody, which allow to obtain the value of f and consequently the value of SF.

$$f = \frac{52.7}{3.7} = 14.24 \;\rightarrow\; SF = \left(1 + \frac{60}{f^3} + \frac{f}{400}\right) = 1.0564 \tag{4.11}$$

In order to obtain the value of the Friction Coefficient, Reynolds and Mach numbers must be calculated (see Chapter 2), and then equation (4.8) is applied.

$$\begin{aligned} Re &= \frac{\rho\, v\, D_0}{\mu_0} = \frac{1.096 \cdot 117.35 \cdot 47.05}{17.894 \cdot 10^{-6}} = 2.6595 \cdot 10^7 \\ M &= \frac{v}{c_S} = \frac{117.35}{\sqrt{T_0 \cdot (1 - 22.57 \cdot 10^{-6} \cdot 1143)}} = 0.349 \end{aligned} \tag{4.12}$$

$$C_f = 0.455\, (\log_{10} Re(D_0))^{-2.58} (1 + 0.144\, M^2)^{-0.65} = 0.002551 \tag{4.13}$$

Then applying equation (4.7), the resulting Drag force of the forebody is:

$$D_{FB} = \frac{\rho}{2} \pi\, l_{FB}\, d_{FB}\, v^2\, C_f\, SF = 12458.5\, N \tag{4.14}$$

Finally, obtaining the deceleration from the data of Table 4.2, the drag area of the reefed parachute can be calculated rearranging equation (4.6):

$$\ddot{x} \sim \frac{\Delta v}{\Delta t} = \frac{117.3 - 31.1}{231 - 218} = -6.63 \frac{m}{s^2} \;\; ; \;\; (C_D S_0)_R = \frac{2\,(m(g - \ddot{x}) - D_{FB})}{\rho v^2} = 273.35\, m^2 \tag{4.15}$$

Therefore each parachute have an individual drag area of $(C_D S_0)_{R_{1,2,3}} = 91.12\, m^2$.

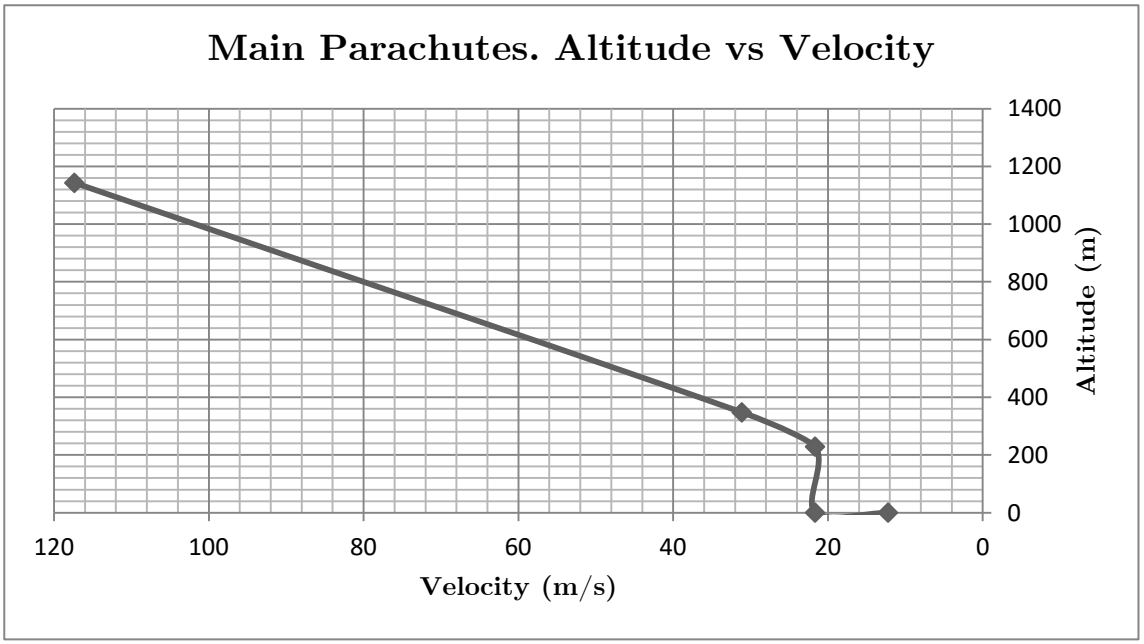

Figure 4.10. Altitude vs Velocity of the Main Parachutes.

With this we can easily obtain the nominal area $(S_0)_R$ dividing by the drag coefficient and thus we can obtain the nominal diameter $(D_0)_R$ of the reefed parachutes.

$$(S_0)_R = \frac{(C_D S_0)_R}{C_D} = 108.435\, m^2 \quad \rightarrow \quad (D_0)_R = \sqrt{\frac{4\, S_0}{\pi}} = 11.75\, m \tag{4.16}$$

Finally, applying the equation (3.10) the inflation time of both phases can be obtained. In this case the constant n must be $n_1 = 8$ and $n_2 = 2$ for ringsail parachutes.

$$\boldsymbol{t_{f1} = 0.20\, s} \quad ; \quad \boldsymbol{t_{f2} = 2.94\, s} \tag{4.17}$$

These values can be considered acceptable, even though the real values are not available, since if we observe the inflation sequence of other parachute examples, the filling time values are similar. Figure 4.11 shows an example of a cluster of two 72.8 ft-diameter conical, full-extended skirt parachutes with a 2200-kg payload.

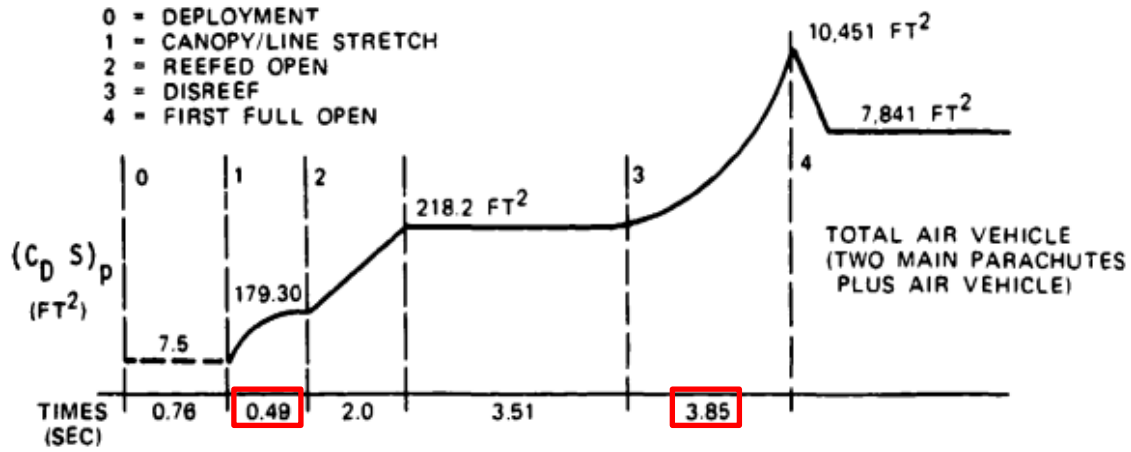

Figure 4.11. Inflation Sequence profile for a 72.8 ft-diameter Parachtue [2].

c) Opening Forces:

To calculate parachute opening forces we can apply the Pflanz Method described in section 3.4.2.d. First we must calculate the ballistic parameter to be able to determine through the graph of Figure 3.16 the force reduction factor X_1.

For the reefed parachutes we have the following data:

$$\left.\begin{array}{c} m_1 = m_{FS}/3 = 42066.7\ kg \\ (C_D S)_R = 91.12\ m^2 \\ \rho(z_R) = 1.096\ kg/m^3 \\ g = 9.81\ m/s^2 \\ v_R = 117.35\ m/s \\ t_{f1} = 0.20\ s \end{array}\right\} \rightarrow \quad A_R = \frac{2\,W_1}{(C_D S)_R\,\rho\,g\,v_R\,t_{f1}} = 35.89 \qquad (4.18)$$

In the case of the disreefed parachute we have:

$$\left.\begin{array}{c} m_1 = m_{FS}/3 = 42066.7\ kg \\ (C_D S)_D = 1461.4\ m^2 \\ \rho(z_D) = 1.185\ kg/m^3 \\ g = 9.81\ m/s^2 \\ v_D = 31\ m/s \\ t_{f2} = 2.94\ s \end{array}\right\} \rightarrow \quad A_D = \frac{2\,W_1}{(C_D S)_D\,\rho\,g\,v_D\,t_{f2}} = 0.533 \qquad (4.19)$$

Before continuing we can observe that the ballistic parameter in this case takes low and different values because the canopy loading is relatively low ($W/(C_D S)_R = 461.7\ kg/m^2$ and $W/(C_D S)_D = 28.8\ kg/m^2$). Therefore, as section 3.4.3 (Altitude effects) explains, before we get the values of the opening forces we can predict that they will decrease in descend because of the strong velocity decrease (finite mass conditions).

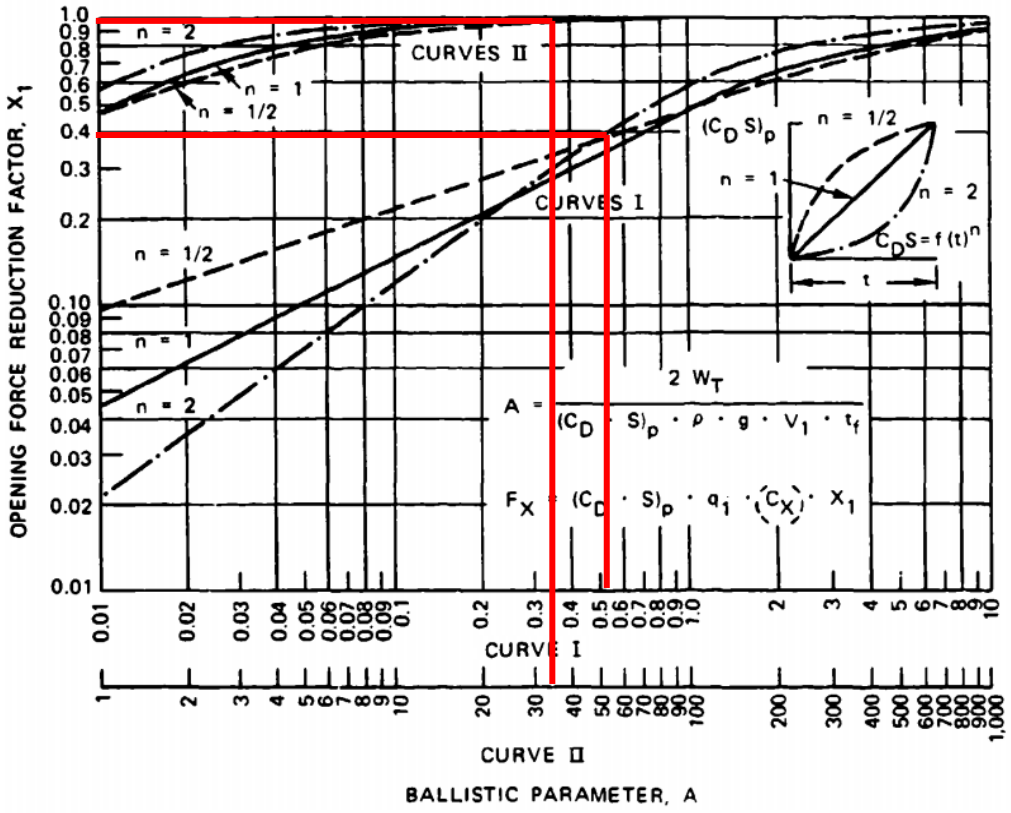

Figure 4.12. Opening-Force reduction factor versus Ballistic Parameter.

From Figure 3.17 we obtain that the force reduction factors are $(X_1)_R = 1$ for the reefed phase and $(X_1)_D = 0.4$ for the disreefed phase. Finally according to Appendix A, for this preliminary design the opening-force coefficient can be considered $C_X = 1.05$. With this the opening forces for each parachute can be obtained using equation (3.11).

$$(F_X)_{Reefed} = (C_D S)_R \cdot q_R \cdot C_X \cdot (X_1)_R = 722032\ N$$
$$(F_X)_{Disreefed} = (C_D S)_D \cdot q_D \cdot C_X \cdot (X_1)_D = 349385\ N \tag{4.20}$$

These are the opening forces applied on one main parachute and as expected, the opening force decreases almost half. These opening forces are one of the most important aspects in the design of the parachute system, since from them it is possible to choose the material that is able to withstand these forces. As we saw in section 3.4.3, an opening of the parachutes at an altitude higher than expected could cause serious damage to the parachute system, as it would experience forces greater than expected at a lower altitude.

Indeed, investigating some of the tests made with the Ares I-X rocket, this issue was a big problem in one of the tests of recovery of the first stage of the Ares I. It can be observed in the video captures of Figure 4.13 that there have been indeed problems in this matter. In particular Figure 4.13 shows that one of the parachutes fails during its opening, although the rest remain and avoid a catastrophic failure.

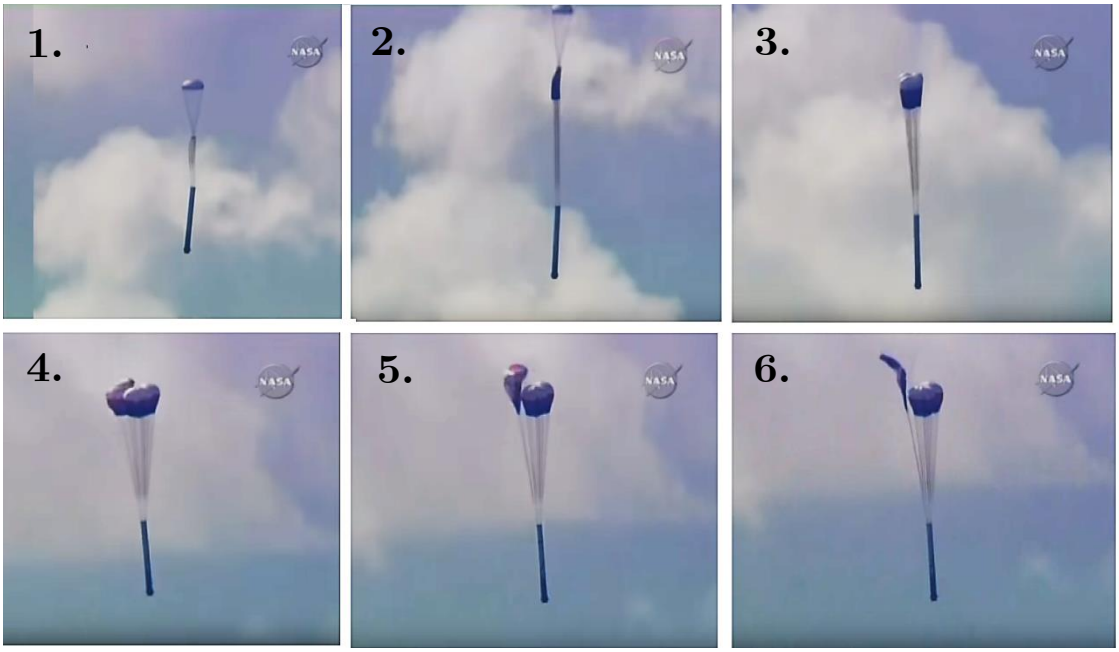

Figure 4.13. Sequence of images of the deployment of the main parachutes of the first stage of the Ares I-X [22].

d) Weight Estimation:

Since we don't have most of the measurements of the components of the parachute, except the diameter of the main parachutes, it is not possible to make an estimation of the complete parachute system weight, however it is possible to calculate a value of the canopy weight using the K. E. French method (Section 3.3.6.d).

First, knowing that $N_{SL}P_s = F_X$, we can rewrite the equation (3.4) as following:

$$W_{canopy} = (1.9 \cdot 10^{-5}(F_X D_0)^{0.96}) \tag{4.21}$$

Therefore, the obtained value of the canopy weight is $\boldsymbol{W_{canopy} = 160.71\ kg}$ and consequently the three canopies would weigh $\boldsymbol{W_{3canopies} = 582.12\ kg}$.

To contrast this result, we can make a similar procedure from data collected from other ringsail canopies made of nylon as the main material. [20]. If these data are represented in a graph, we obtain a curve with an exponential tendency, from which we can deduce that the canopy weight is:

$$W_{canopy} = 0.0598\, D_0^{2.046} \ \rightarrow \boldsymbol{W_{canopy} = 158.38\ kg} \ \rightarrow \ \boldsymbol{W_{3canps} = 475.15\ kg} \tag{4.22}$$

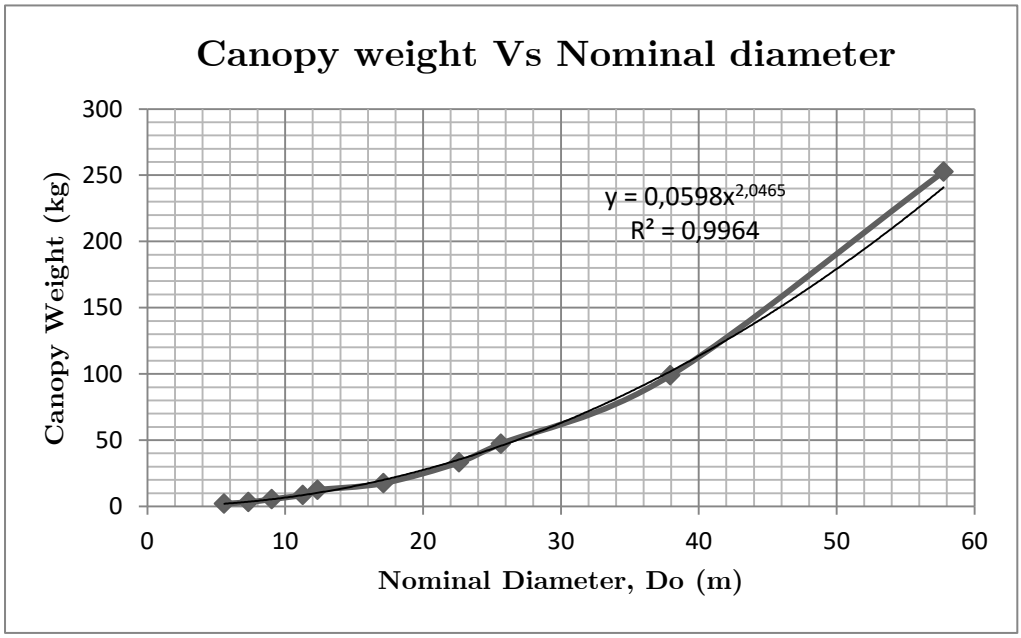

Figure 4.14. Canopy Weight versus Nominal Diameter for different sizes Ringsail Parachutes [20].

These two values of canopy weight obtained present a difference of about 2 kg for each canopy, which allows us to deduce that it is quite probable that the real canopy has a weight around 160 kg.

4.2.2. Drogue Chute Design

a) Nominal Diameter:

The following operational requirements govern the design of the drogue chute:

- The drogue chute must have a reliable operation in the velocity range from 157.9 m/s at 4206 meters (Point 7, Table 4.2).
- The drogue chute must be able to decelerate the forebody to the permissible opening speed of the main parachute assemblies, which is 103.6 m/s at an altitude of 1371 meters (Point 9, Table 4.2).

Evaluating the possible drogue chute candidates from Appendix A, the conical ribbon parachute meets all requirements and has a higher drag coefficient than the equally suited hemisflo parachute. The drag coefficient determines the parachute size and its associated weight and volume.

As we can see in Figure 4.6, the behaviour of the drogue chute is similar to that of the main reefed parachutes. Therefore the diameter of the drogue chute can be determined with the same procedure used to determine the diameter of the reefed parachutes.

Applying equation (4.14), the drag of the forebody, when the descent velocity is $v = 157.9\, m/s$, is:

$$D_{FB} = \frac{\rho}{2} \pi\, l_{FB}\, d_{FB}\, v^2\, C_f\, SF = 16352.8\, N \tag{4.23}$$

Obtaining the deceleration from the data of Table 4.2, the drag area of the drogue chute can be calculated using equation (4.15):

$$\ddot{x} \sim \frac{\Delta v}{\Delta t} = \frac{103.6 - 157.9}{216 - 194} = -2.467\, m/s^2 \tag{4.24}$$

$$(C_D S_0)_{DC} = \frac{(2\,(m(\ddot{x} - g) + D_{FB})}{\rho v^2} = 153.5\, m^2 \tag{4.25}$$

Therefore, assuming that the conical ribbon parachute has a drag coefficient $C_D = 0.5$, we can obtain the nominal area and consequently the nominal diameter:

$$(S_0)_{DC} = \frac{(C_D S_0)_{DC}}{C_D} = 307.039\, m^2 \quad \rightarrow \quad (D_0)_{DC} = \sqrt{\frac{4\, S_0}{\pi}} = \mathbf{19.77\ m} \tag{4.26}$$

Comparing the value of this nominal diameter with that one of the drogue chute used in the Ares's first stage ($D_{0_{DC}} = 20\, m$, Section 4.1.1), it can be deduced that it is a practically identical value, and therefore the assumptions are correct.

b) Canopy Inflation Time:

The inflation time can be calculated in this case using equation (3.6), specific for the ribbon parachute.

$$t_{f_{DC}} = \frac{8 \cdot D_{0_{DC}}}{0.9 \cdot v} \quad \rightarrow \quad \boldsymbol{t_{f_{DC}} = 1.11\ s} \tag{4.27}$$

c) Opening Forces:

In order to determine the Opening Force, we will apply again, just as the Section 4.2.1.c, the Pflanz method described in section 3.4.2.d.

Applying equation (3.12) the ballistic parameter is obtained:

$$\left.\begin{array}{c} m_1 = 126200\ kg \\ (C_D S)_{DC} = 153.5\ m^2 \\ \rho(4206) = 0.801\ kg/m^3 \\ g = 9.81\ m/s^2 \\ v_{DC} = 157.9\ m/s \\ t_{f1} = 1.11\ s \end{array}\right\} \rightarrow \quad A_R = \frac{2\ m_1}{(C_D S)_{DC}\ \rho\ v_{DC}\ t_{f1}} = 1.194 \tag{4.28}$$

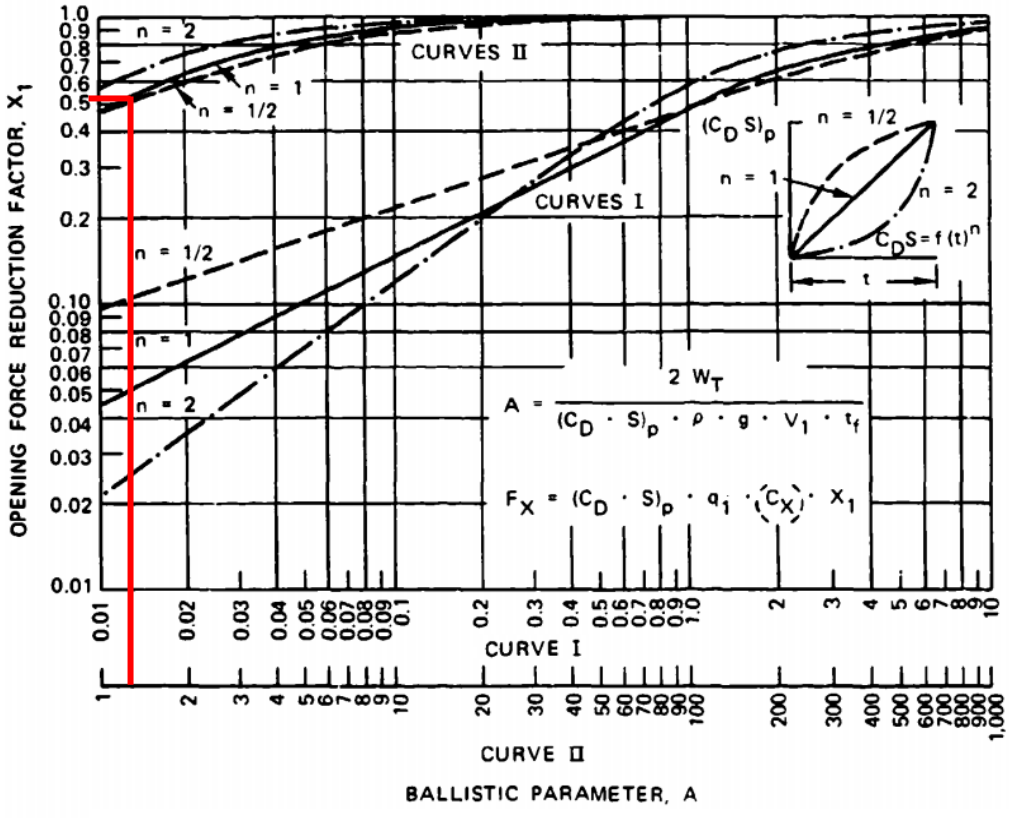

Figure 4.15. Opening-Force reduction factor versus Ballistic Parameter.

From Figure 4.15 we obtain that the force reduction factor is $(X_1)_{DC} = 0.5$.

Finally according to Appendix A, the opening-force coefficient for the conical ribbon parachute is $C_X = 1.05$. With this the opening force can be obtained using equation (3.11).

$$(F_X)_{DrogueChute} = (C_D S)_{DC} \cdot q_{DC} \cdot C_X \cdot (X_1)_{DC} = \mathbf{804497\ N} \tag{4.29}$$

d) Weight Estimation:

Again, as in the Section 4.2.1.d, we can only calculate the weight of the canopy by applying the K. E. French method (Section 3.3.6.d).

$$W_{DC_{canopy}} = \left(1.9 \cdot 10^{-5}\left(F_{X_{DC}} D_0\right)^{0.96}\right) \rightarrow \quad W_{DC_{canopy}} = \mathbf{155.7\ kg} \tag{4.30}$$

CHAPTER 5: Impact Attenuation System. General Design Considerations

5.1. Landing Analysis

The rate of descent, the allowable impact deceleration, the type of vehicle, or the required deceleration stroke (or distance) are factors that determine need for impact attenuation.

This required deceleration distance (stroke) can be defined as follows [2]:

$$s = \frac{v_1^2 - v_2^2}{2g(n-1)} \tag{5.1}$$

Where:

- s is the required deceleration stroke (distance).
- v_1 is the rate of descent at start of deceleration.
- v_2 is the rate of descent at impact.
- g is the acceleration of gravity.
- n is the allowable impact deceleration factor in multiples of g.

Figure 5.1 shows the required deceleration stroke for any kind of vehicle as a function of the rate of descent, v_1, and the allowable impact deceleration, n, using the assumption that the velocity at impact, v_2, is zero. As it can be seen, the selection of the impact attenuator best suited for the operation is mainly based on the required deceleration stroke and the allowable impact deceleration. Because of this we can differentiate three primarily types of impacts attenuators with different application ranges: Crushable and frangible attenuators are suitable for low required deceleration strokes and have a high impact deceleration; Inflatable airbags are best suited for higher deceleration strokes than the crushable attenuators and also permit a low impact deceleration; and Retrorockets are used for longer deceleration strokes and are very suitable for low impact deceleration.

Some examples of allowable impact deceleration factors based on measured data and experience are listed in Table 5.1 [2].

Operation	**Impact deceleration, g**
Military airdrop cargo	20 to 35
Target drones, unmanned vehicle structures	20 to 30
Telemetry equipment	20 to 25
Sensitive electronics equipment	5 to 10
Aircrew members	6 to 10
Astronauts after long duration space flights	3 to 5

Table 5.1. Allowable Impact Decelerations [2].

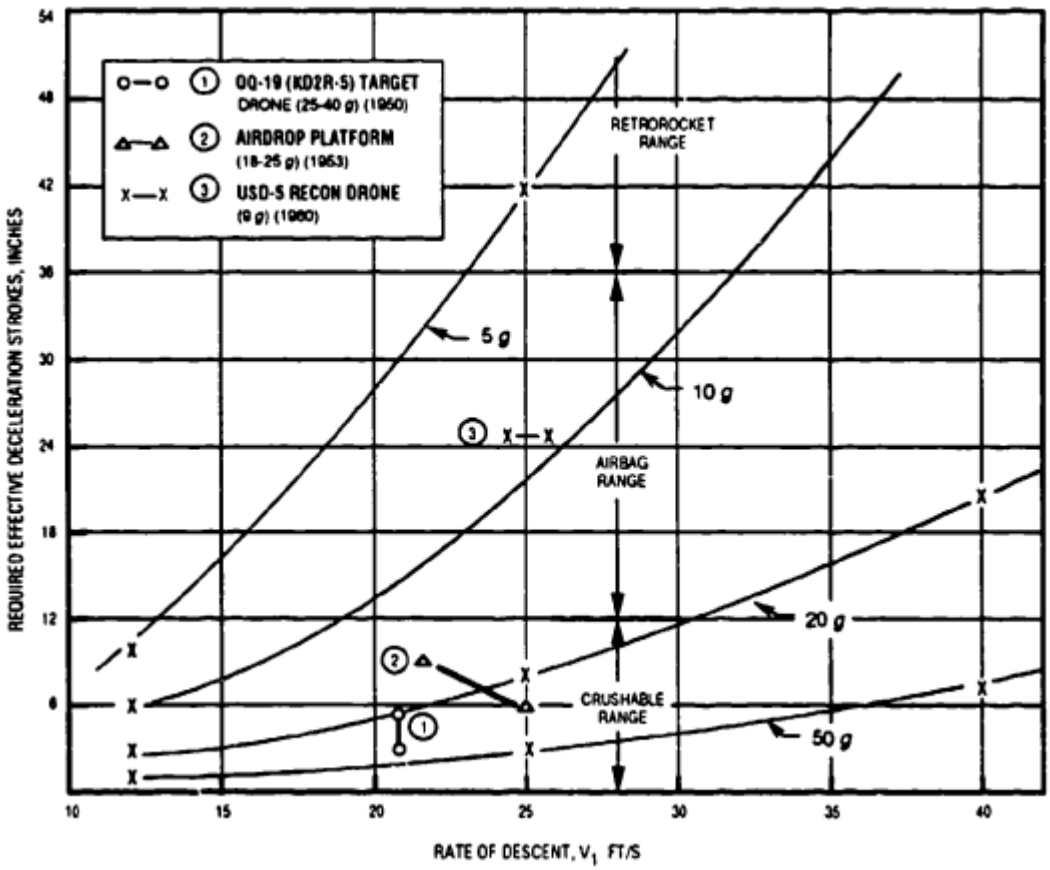

Figure 5.1. Deceleration Stroke vs Rate of Descent and Allowable Impact Deceleration [2].

5.1.1. Crushable Impact Attenuators:

Crushable impact attenuators include paper, plastic, aluminium honeycomb, and several types of foam material. All honeycomb material consists of a cell structure with variation in the cell size and material density. The energy absorption capability is higher in the x-direction (see Figure 5.2). The primary application of the crushable impact attenuator is cushioning material for airdroppable cargo platforms that require energy absorption primarily in the vertical plane, with the horizontal energy being absorbed by sliding on the ground.

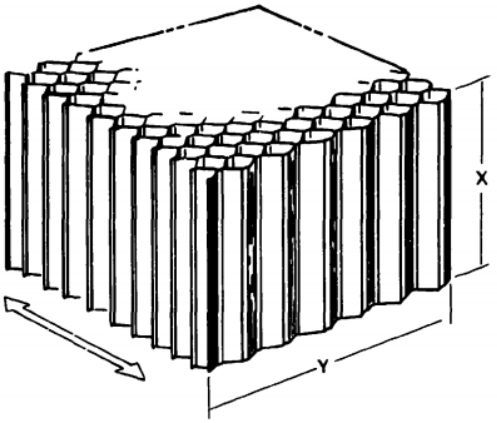

Figure 5.2. Typical Honeycomb Structure [2].

5.1.2. Air Bags

Air Bags are very used for impact attenuation of target and reconnaissance drones, training missiles or landing of aircrew escape modules because they require relatively little storage volume compared to crushables, are reusable, have a high energy absorption capability per unit of weight, and use almost 100% of the compression stroke for shock absorption.

The basic concept of the airbags consists of a textile bag coated with flexible plastic with zero porosity. The bag or bags are stored in the fuselage of the vehicle. After the main descent, parachutes are inflated, the bag compartment cover is ejected, and the bag is deployed and inflated to obtain a proper initial shape. At ground contact, the pressure in the bag rises adiabatically. At a predetermined level, pressure relief valves open and allow part of the compressed gas to escape. This venting mechanism flattens the pressure force curve, releasing energy from the system and thus allowing rapid damping of the movement for better bag efficiency. Airbags are always designed for one specific energy level. Changing the rate of descent, and thereby the energy to be absorbed, results in a bounce at the end of the deceleration stroke if the energy is higher than the design level. Figure 5.3 is a typical airbag pressure-stroke diagram.

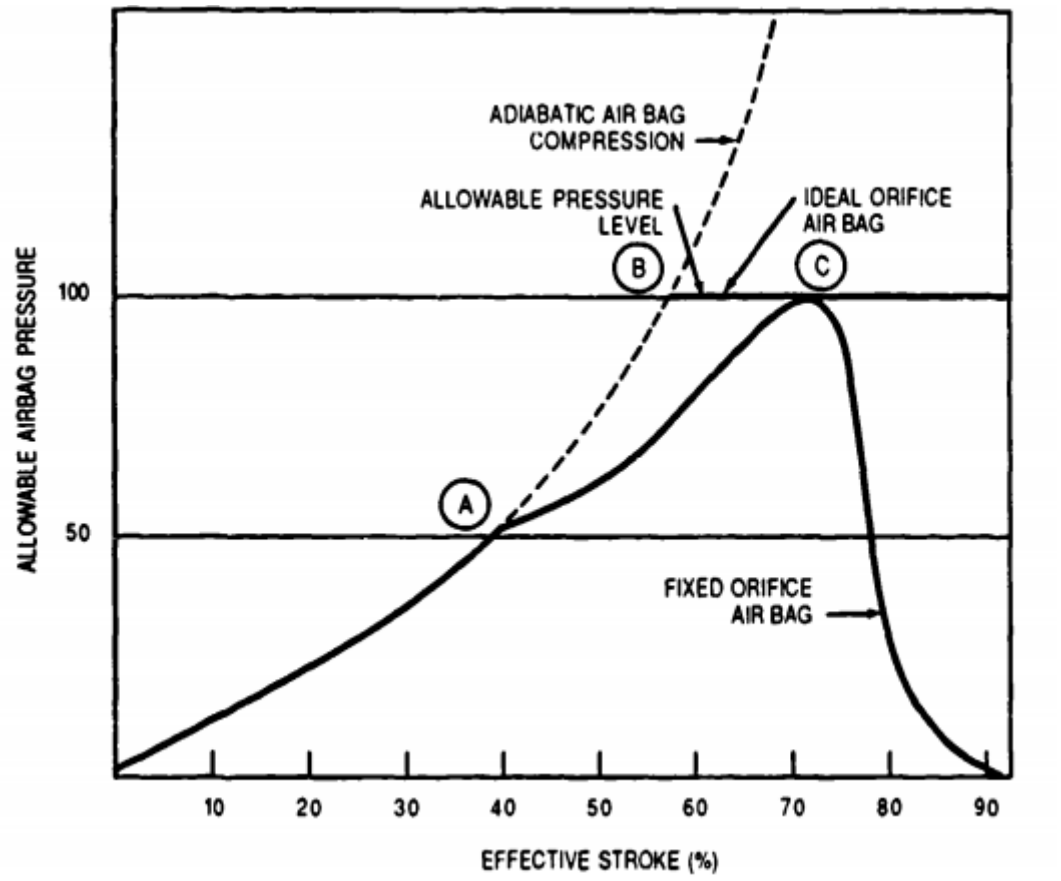

Figure 5.3. Airbag Pressure vs Stroke Characteristics [2].

At ground contact, the bag starts to compress and the internal pressure increases until at Point A, where the pressure relief valves open simultaneously, staggered or pressure controlled. Then the pressure increase lessens until the allowable pressure level is reached at Point C. Finally a pressure decay follows. The design of the pressure relief valves contributes notably to the efficiency of the bag. Ideal orifices permit the bag pressure to rise Point B and then remain constant until ground impact.

5.1.3. Retrorocket Landing Attenuation System

Retrorockets may be called long-stroke impact attenuators. Retrorockets are well suited for loads and vehicles that have impact deceleration limits when landing in the 3- to 6-g range that normally results in required deceleration strokes of more than 1 meter. The main advantage of retrorockets is their high energy-weight ratio and their capability of decelerating the vehicle before ground contact.

Retrorockets, like most other impact attenuators, are designed for one energy level but this problem can be solved using a two-step rocket. The high thrust level is decreased to a lowest energy level and then this low-energy deceleration stops the vehicle slightly above the ground and gently lowers it for final landing.

5.2. Airbag Impact Dynamics Modelling

In this section the operation of the airbag system will be described in greater detail, because it is the most appropriate impact attenuator for rocket's stage recovery applications. As its capabilities show in Section 5.1, airbag impact attenuation systems are used for applications in which very strict allowable impact decelerations are not required, as is the case for the recovery of the stage of a rocket. In addition they are economically cheaper than the retrorockets and can have a second function of float for those cases in which the landing takes place in the sea.

Fundamentally, airbags attenuate impact loads on objects through a series of energy conversion processes. During landing, the kinetic energy of an impacting object is transferred into the internal energy of the gas within the airbag. When predetermined conditions are met, vents within the airbag open, releasing the gas into the open environment and thereby removing this energy form the system. Although seemingly simple, this process involves principles from several disciplines, including thermodynamics, fluid mechanics and structural dynamics.

5.2.1. Thermodynamics Analysis

Considering a system dropped vertically from a fixed height, consisting of a solid mass supported underneath by a gas-filled airbag with an in-built vent, as shown in Figure 5.4 below:

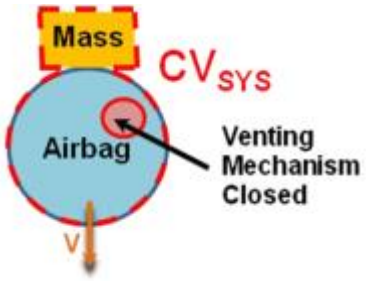

Figure 5.4. Initial Condition for Thermodynamic Analysis [23].

Throughout the duration of this process, the system experiences three main dynamic phases, each of which having a unique thermodynamic state. These phases include:

1) Freefall.
2) Compression of the airbag after contact with the ground surface.
3) Venting of the airbag, assumed here to commence at the moment at which the airbag has attained its maximum compression.

It should be noted that even though the entire process is inherently transient, the state of the system at the end of each major phase will be assumed to be in quasi-equilibrium, therefore the properties of the system are uniform across the system at each of these phases.

1) From Freefall to First Contact of the System with the Ground Surface.

During the period prior to initial contact with the ground surface, the system is closed and isolated. That is, the energy content of the system stays constant, and no work is done on the system. The energy content (E) is a result of the combination of the kinetic (KE), the potential energy (PE) and the internal energy (U) of the gas within the airbag. This can be represented mathematically as follows:

$$E_{Sys} = PE_{Mass} + KE_{Mass} + PE_{Gas} + KE_{Gas} + U_{Gas} \tag{5.2}$$

Note here that the contributions to the system energy by the airbag itself are neglected here as they are insignificant to those of the mass and the gas within the airbag. Furthermore, the internal energy of the mass is also ignored as it is negligible compared to the other energy contributions to the system.

Considering the standard relationships for kinetic and potential energy, equation (5.2) can be rewrite as:

$$E_{Sys} = m_{Mass}gh + \frac{1}{2}m_{Mass}v^2 + m_{Gas}gh + \frac{1}{2}m_{Gas}v^2 + U_{Gas} \tag{5.3}$$

Because the altitude is almost zero, potential energies are also zero, and since the operating medium is assumed to behave as an ideal gas, the Ideal Gas Law can be used to determine the mass of air within the airbag.

$$pV = mRT \tag{5.4}$$

2) From Initial Contact with the Surface to Maximum Airbag Compression.

As Figure 5.5 shows, during this phase the mass does boundary work on the airbag as its weight acts to compress the airbag. Consequently, only a thermodynamic analysis of the gas within the airbag is required. As can be seen the system remains no longer isolated, due to the work being done on it.

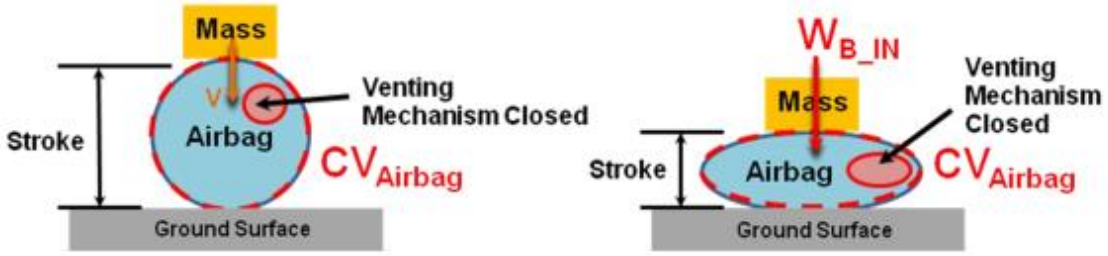

Figure 5.5. System State Transition between Initial Contact weight the Surface and Maximum Airbag Compression [23].

This process can be represented quantitatively using the First Law of Thermodynamics, which states that the energy must be conserved.

$$E_{IN} - E_{OUT} = \Delta E_{Gas} \tag{5.5}$$

Since the process is assumed to be adiabatic and no work is being done by the internal gas, there is no energy leaving the control volume ($E_{OUT} = 0$). Hence the energy content of the gas within the airbag can be expressed as:

$$W_B = U_2 - U_1 \tag{5.6}$$

Where W_B denotes the boundary work being done on the operating medium, and the subscripts 1 and 2 denote respectively the period of initial contact between the airbag and the surface, and the time at which the airbag reaches its maximum compression.

The energy content of the system at this latter period can be observed by simply rearranging equation (5.6).

$$U_2 = U_1 - W_B \tag{5.7}$$

In effect, equation (5.7) states that during the compression phase of the airbag, the kinetic energy of the mass is being transferred into the internal energy of the gas via the means of boundary work. The amount of kinetic energy transferred is equal to the magnitude of the boundary work, which is defined as the integral of the system pressure (P) over its changing volume (V).

$$W_B = \int_1^2 P\, dV \tag{5.8}$$

A dependence on pressure and volume implies that boundary work, and hence the efficiency of the energy transfer between the mass and the gas, is directly related to the change in the geometry of the airbag as it compresses.

Assuming that the energy transfer process is completely efficient, the boundary work at state 2 is equal to the kinetic energy of the mass and the gas at state 1.

$$U_2 = U_1 - (KE_{Mass} + KE_{gas}) \tag{5.9}$$

3) From Airbag Venting to Rest.

The vents built into the airbag are opened immediately after it has reached its maximum compression. At this point, the system becomes one which is open, as mass is allowed to cross the boundary of the control volume.

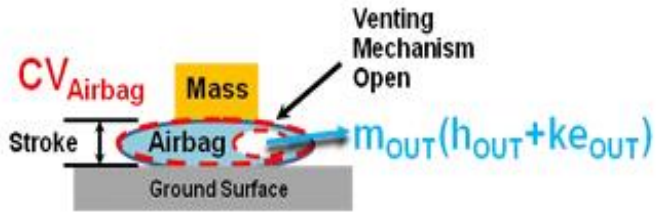

Figure 5.6. System during the Venting Phase [23].

To simplify the analysis, it will be assumed that boundary work is no longer being done on the operating medium during this phase. As a consequence, $E_{IN} = 0$, and the energy content of the system by the time it comes to rest can be represented by:

$$-m_{OUT}(h_{OUT} + ke_{OUT}) = U_3 - U_2 \tag{5.10}$$

Where h_{OUT} denotes the specific enthalpy, ke_{OUT} denotes the specific kinetic energy, and the subscript 3 denotes the state of the system being at rest. Again, the energy content of the system after this process can be expressed by rearranging equation (5.10) as follows:

$$U_3 = U_2 - m_{OUT}(h_{OUT} + ke_{OUT}) \tag{5.11}$$

It can be seen that the final energy of the content of the system is equal to its energy prior to venting, minus the energy removed by the kinetic energy and enthalpy of the vented gas.

Ideally, this system would have zero energy at the end of the venting stage, signifying a complete attenuation of the impact energy. To obtain an estimate for the proportion of gas required to be vented to achieve this, U_3 will be set to zero and equation (5.11) will be solved for m_{OUT}.

$$m_{OUT} = \frac{U_2}{h_{OUT} + ke_{OUT}} \tag{5.12}$$

5.2.2. System Dynamics Equation

From a fluid mechanics perspective, the change in airbag geometry is calculated based on the position of the supported mass. This is then used to obtain the pressure, volume and mass of the operating medium, which is in turn used to determine the conditions for venting of the airbag.

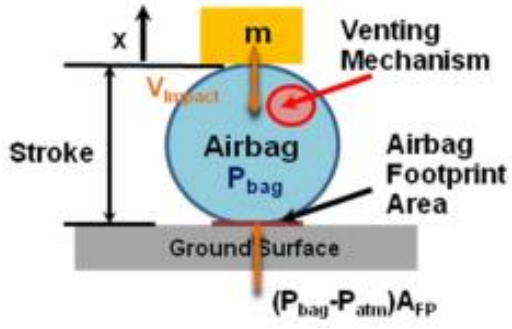

Figure 5.7. Single Airbag Impact Model Initial Condition [23].

Considering the initial condition of the model presented in Figure 5.7, it can be observed that the forces present in this single degree of freedom are:

- The force resulting from the acceleration of the mass sitting atop the airbag as it impacts with the ground surface.
- The weight force of the mass sitting atop the airbag.
- The reaction force from the surface, which can be simplified to be equivalent to the effects of the differential pressure between the airbag operation medium and the local atmosphere on the contacting area.

$$m\,\ddot{x} = \left(p_{bag}(x) - p_{atm}\right)A_{FP}(x) - m\,g \tag{5.13}$$

This equation forms the basis for the determination of the system dynamic state at each instant within the airbag impact model. Considering the finite difference representation of the acceleration term, $\ddot{x} = \Delta U/\Delta t$, where ΔU is the change in velocity, equation (5.13) can be used to represent the change in system velocity over each timestep:

$$\Delta U = \frac{A_{FP}\,p_{atm}\,\Delta t}{m}\left(\frac{p_{bag}}{p_{atm}} - 1 - \frac{mg}{A_{FP}\,p_{atm}}\right) \tag{5.14}$$

5.2.3. Shape Function Equations

Considering that the typical airbag geometry is a cylinder, two simple shape functions are needed to represent the changing volume and ground contact surface of the airbag as it compresses. This shape functions assume that the axial length of the cylindrical airbags remains constant throughout the compression process. As a result, these functions only focus on the changing cross section of the airbag form its initial circular shape, as is shown below in Figure 5.8.

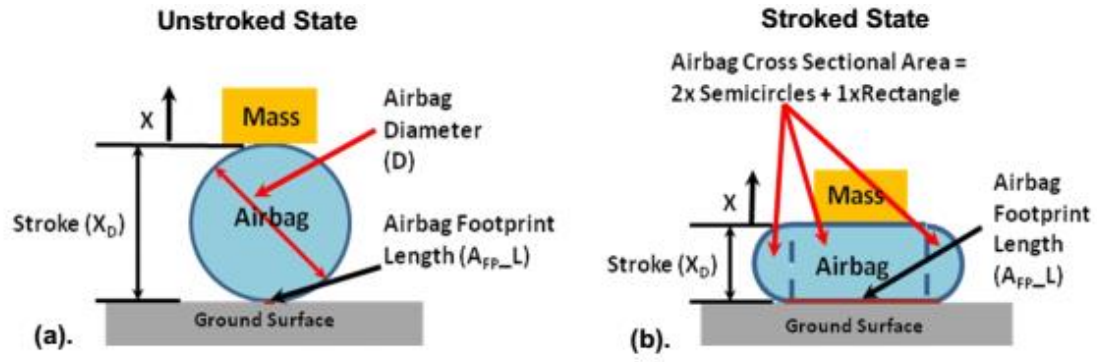

Figure 5.8. Shape Function used in Single Airbag Impact Model [23].

A condition is enforced such that the circumference of the airbag cross section remains constant. This can be expressed as:

$$\pi D = \pi X_D + 2L_{A_{FP}} \tag{5.15}$$

Rearranging equation (5.15) the airbag footprint length can be written as a function of the airbag stroke:

$$L_{A_{FP}} = \pi(D - X_D) \tag{5.16}$$

The cross sectional area of the airbag in the stroked state can be determined using the fact that it consists of a rectangle and two semi-circles:

$$A_{X-section} = \pi X_D^2/4 + X_D L_{A_{FP}} \tag{5.17}$$

Since the axial length (L) is assumed to remain constant throughout the compression process, the airbag volume and contact surface can be obtained.

$$A_{FP}(X_D) = L \cdot L_{A_{FP}}(X_D) = L\,\pi(D - X_D) \tag{5.18}$$

$$V(X_D) = L\,A_{X-section} = L\,X_D\left(\pi\frac{X_D}{4} + L_{A_{FP}}\right) \tag{5.19}$$

5.2.4. Gas Dynamics Equation

A simplifying assumption is made such that the operating medium within the airbag acts as an ideal gas, and that the process is isentropic.

Therefore the Ideal Gas Law can be applied:

$$p\,V = w\,R_{Gas}T \tag{5.20}$$

Where p is the pressure, V is the volume, w is the equivalent mass of the gas, R_{Gas} is the specific gas constant, and T is the operating temperature.

And it can be also considered the Isentropic Process Equation:

$$\frac{T_2}{T_1} = \left(\frac{p_2}{p_1}\right)^{\frac{\gamma-1}{\gamma}} = \left(\frac{\rho_2}{\rho_1}\right)^{\gamma-1} \tag{5.21}$$

5.2.5. Orifice Flow Equations

The flow of a gas can be modelled using the mass flow equation applied at the location of the orifice:

$$\frac{dw}{dt} = C_D\, A_{th}\, \rho_{th}\, v_{th} \tag{5.22}$$

Where the subscript *th* indicates the state at the orifice, C_D is the discharge coefficient (a factor representing inefficiencies in the flow stream), A_{th} is the orifice area during the current timestep, and v_{th} is the flow velocity through the orifice. The mass flow rate through the orifice can be represented in terms of only the pressure and temperature of the gas using the following equations:

Density form of the Ideal Gas Law applied at the orifice:

$$\rho_{th} = \frac{p_{th}}{R_{Gas} T_{th}} \tag{5.23}$$

The velocity to the gas:

$$v_{th} = M_{th}\, c_{th} \quad ; \quad c_{th} = \sqrt{\gamma R_{Gas} T_{th}} \tag{5.24}$$

Combining equations (5.23) and (5.24) into equation (5.22), the mass flow rate is:

$$\frac{dw}{dt} = C_D\, A_{th}\, p_{th}\, M_{th} \sqrt{\frac{\gamma}{R_{Gas} T_{th}}} \tag{5.25}$$

Since there is close to zero average flow of gas within the airbag, a standard nozzle flow equation can be used to relate the flow velocity through the orifice, to the ratio of pressure at the orifice and upstream from it.

$$\frac{p_{th}}{p_u} = \left(1 + \frac{(\gamma - 1) M_{th}^2}{2}\right)^{\frac{\gamma}{\gamma - 1}} \tag{5.26}$$

Where p_u indicates the pressure upstream from the orifice, that is effectively the same pressure as of that to the airbag, as shown in Figure 5.9.

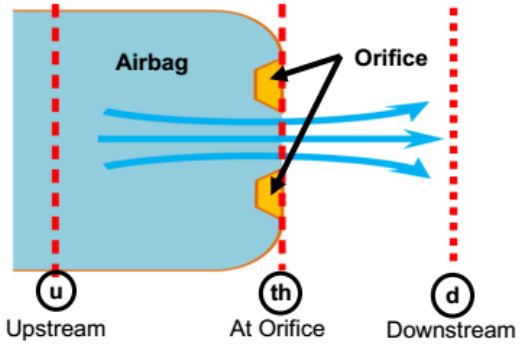

Figure 5.9. Definition of Upstream and Downstream Pressure as used by the Single Airbag Impact Model [23].

With this, equation (5.26) can be rearranged:

$$M_{th} = \left(\frac{2}{\gamma - 1} \left(\left(\frac{p_{th}}{p_u} \right)^{\frac{1-\gamma}{\gamma}} - 1 \right) \right)^{\frac{1}{2}} \tag{5.27}$$

Substituting this result into equation (5.25) yields:

$$\frac{dw}{dt} = C_D \, A_{th} \, p_{th} \left(\frac{2}{\gamma - 1} \left(\left(\frac{p_{th}}{p_u} \right)^{\frac{1-\gamma}{\gamma}} - 1 \right) \right)^{\frac{1}{2}} \left(\frac{\gamma}{R_{Gas} T_{th}} \right)^{\frac{1}{2}} \tag{5.28}$$

Assuming that the gas at the orifice experiences an isentropic process from the initial system state to the current state, the initial pressure and temperature of the gas at the orifice are the same as those of the gas within the airbag.

$$\frac{1}{T_{th}} = \frac{1}{T_i} \left(\frac{p_i}{p_{th}} \right)^{\frac{\gamma-1}{\gamma}} \tag{5.29}$$

Thus, substituting equation (5.29) into equation (5.28) results in:

$$\frac{dw}{dt} = C_D \, A_{th} \, p_{th} \left(\frac{2}{\gamma - 1} \left(\left(\frac{p_{th}}{p_u} \right)^{\frac{1-\gamma}{\gamma}} - 1 \right) \right)^{\frac{1}{2}} \left(\frac{\gamma}{R_{Gas}} \right)^{\frac{1}{2}} \left(\frac{1}{T_i} \left(\frac{p_i}{p_{th}} \right)^{\frac{\gamma-1}{\gamma}} \right)^{\frac{1}{2}} \tag{5.30}$$

Finally, manipulating this equation and considering that the upstream pressure is equivalent to the airbag pressure ($p_u = p_{bag}$) and orifice pressure is equal to the local, downstream atmospheric pressure ($p_{th} = p_{atm}$) the final form of this orifice flow equation can be expressed as:

$$\frac{dw}{dt} = C_D \, A_{th} \, p_{atm} \left(\frac{\gamma}{R_{Gas} \, T_i} \right)^{\frac{1}{2}} \left(\frac{2}{\gamma - 1} \left(\left(\frac{p_{atm}}{p_{bag}} \right)^{\frac{1-\gamma}{\gamma}} - 1 \right) \left(\frac{p_i}{p_{atm}} \right)^{\frac{\gamma-1}{\gamma}} \right)^{\frac{1}{2}} \tag{5.31}$$

In this last equation it can be seen that the mass flow rate is a function of the ratio between the airbag pressure and the local atmospheric pressure. Moreover, it is important to note that this relationship is only valid for subsonic flows.

In the case that the flow through the orifice is sonic, $M_{th} = 1$, equation (5.26) reduces to:

$$\frac{p_{th}}{p_u} = \left(\frac{\gamma + 1}{2} \right)^{\frac{\gamma}{1-\gamma}} \tag{5.32}$$

Proceeding in the same way as in the subsonic case, the equation for sonic flow through the airbag orifice is given as:

$$\frac{dw}{dt} = C_D\, A_{th}\, p_i \left(\frac{\gamma}{R_{Gas}\, T_i}\right)^{\frac{1}{2}} \left(\left(\frac{2}{\gamma+1}\right)^{\frac{\gamma+1}{\gamma-1}} \left(\frac{p_{bag}}{p_i}\right)^{\frac{\gamma+1}{\gamma}}\right)^{\frac{1}{2}} \tag{5.33}$$

In this case it can be observed that the sonic orifice flow has a flow rate that remains constant and unaffected by the fluctuations in the pressure downstream of the orifice.

To determine if the flow through the orifice is subsonic or sonic, the pressure ratio across the orifice compared to that of the critical pressure ratio of the operating medium. This critical pressure ratio is defined as the ratio at which the flow is accelerated to a velocity equal to that of the local velocity of sound. Subsequently, this can be obtained from equation (5.32) substituting the appropriate ratio of specific heats for a given operating medium. For atmospheric air at room temperature, this specific heat ratio is 1.4 and thereby the critical pressure ratio is:

$$\frac{p_{th}}{p_u} = \left(\frac{\gamma+1}{2}\right)^{\frac{\gamma}{1-\gamma}} = \left(\frac{1.4+1}{2}\right)^{\frac{1.4}{1-1.4}} = 0.528 \tag{5.34}$$

Therefore, if the pressure ratio across the orifice is less than 0.528, the flow through the orifice is subsonic and equation (5.31) applies. However, if the pressure ratio across the orifice is greater than 0.528, the sonic orifice flow is given by equation (5.33).

* Discharge Coefficient

The discharge coefficient refers to the losses due to frictional and viscous effects as the gas flow through the orifice, which varies as function of the pressure ratio across the orifice. To model this effect, data obtained from orifice flow experiments conducted by Perry [24] was used to form an empirical relationship between pressure ratio and discharge coefficient.

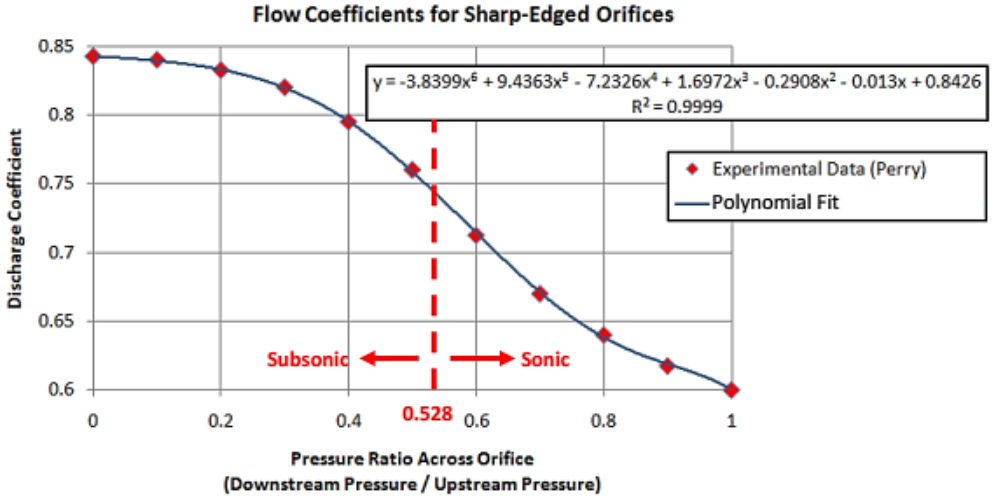

Figure 5.10. Data used to model the Discharge Coefficient within the Single Airbag Impact Model [24].

5.2.6. The Integrated Single Airbag Impact Model

The governing equations from each of the previously discussed functional modules can be integrated into a general framework, as shows Figure 5.11.

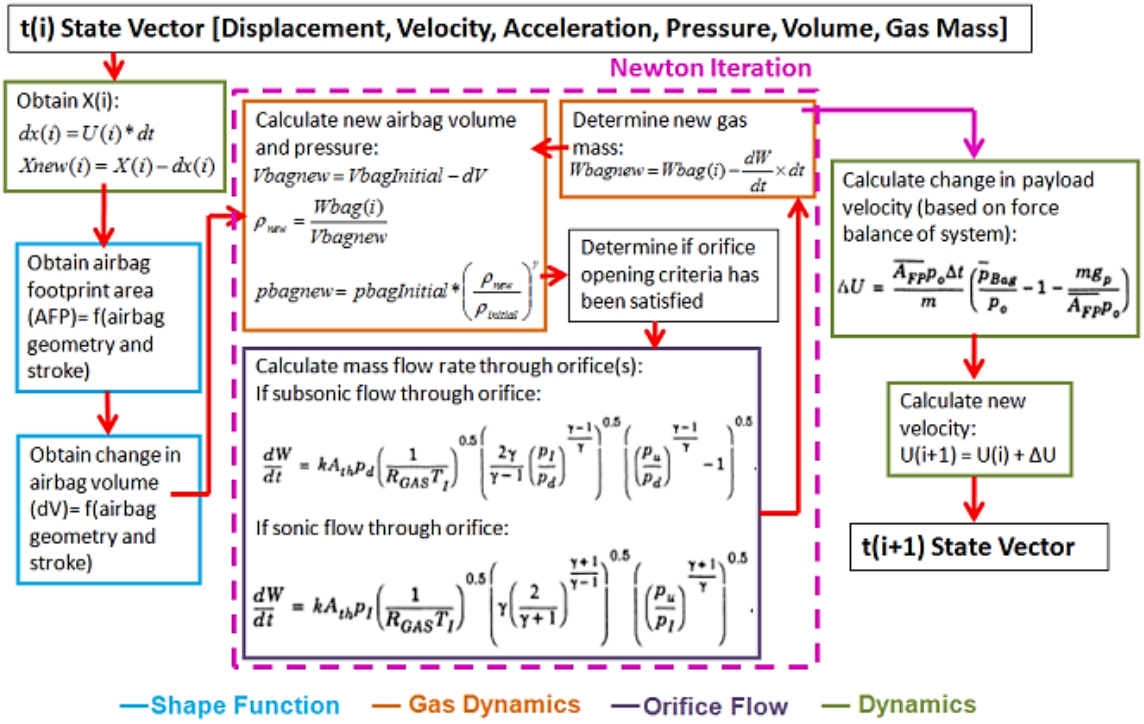

Figure 5.11. Single Airbag Impact Model Functional Flow Block Diagram [23].

It can be seen that there is an iterative interaction between the gas dynamics and orifice flow components of the model. This is because the orifice flow module requires pressure information from the gas dynamic module, which in turn requires knowledge of the mass of gas within the airbag, which is dependent on the orifice flow conditions.

To resolve this circular dependence, the pressure and gas mass values at each time step are solved for simultaneously by applying Newton's method. For the case where a root of a real valued function is being searched for, the method travels along this direction until it obtains a solution with a zero objective value. If the initial guess is sufficiently close enough to the root, this resulting solution will be an improved approximation to the root when compared to the previous guess. By repeating this process in an iterative manner, the obtained solution will gradually move closer towards the root of the function. This method is summarized by the following equation:

$$x_{n+1} = x_n - \frac{f(x_n)}{f'(x_n)} \tag{5.35}$$

Where n is an index representing the n^{th} iteration, f is the real valued function, x is the approximation to the root of f, and f' is the first derivative of f with respect to x.

Therefore, a general Newton step for a function of pressure can be expressed as:

$$p_{t+\Delta t,n+1} = p_{t+\Delta t,n} - \frac{f(p_{t+\Delta t,n})}{f'(p_{t+\Delta t,n})} \tag{5.36}$$

Where p is the airbag pressure, t is a time coordinate and n is an increment denoting the iteration number. For the purposes of simplifying the notation used in this derivation, let $p_{t+\Delta t,n}$ be denoted by $p_{new}(n)$ and $p_{t+\Delta t,n+1}$ by $p_{new}(n+1)$. Furthermore, let the pressure from the previous time step, that is p_t, be denoted by p_{old}. Thus, equation (5.36) becomes:

$$p_{new}(n+1) = p_{new}(n) - \frac{f(p_{new}(n))}{f'(p_{new}(n))} \tag{5.37}$$

From this, explicit relationships for $f(p_{new})$ and $f'(p_{new})$, can be derived as follows:

- $\boldsymbol{f(p_{new})}$

The relationship that describes the change in airbag pressure from one timestep to the next is given by equation (5.21):

$$p_{new} = p_{old}\left(\frac{\rho_{new}}{\rho_{old}}\right)^{\gamma} = p_{old}\left(\frac{w_{new}}{\rho_{old}V_{new}}\right)^{\gamma} = p_{old}\left(\frac{w_{old} - \frac{dw(p_{new})}{dt}dt}{\rho_{old}V_{new}}\right)^{\gamma} \tag{5.38}$$

Moreover, the mass flow rate component of this equation for subsonic flow (equation (5.31)) can be expressed as:

$$\frac{dw}{dt} = C_D p_{new} A_{th} p_{atm}\left(\frac{\gamma}{R_{Gas}T_i}\right)^{\frac{1}{2}}\left(\frac{2}{\gamma-1}\left(\left(\frac{p_{atm}}{p_{new}}\right)^{\frac{1-\gamma}{\gamma}} - 1\right)\left(\frac{p_i}{p_{atm}}\right)^{\frac{\gamma-1}{\gamma}}\right)^{\frac{1}{2}} \tag{5.39}$$

Substituting equation (5.39) into equation (5.38) yields:

$$p_{new} = p_{old}\left(\frac{1}{\rho_{old}V_{new}}\left\{\begin{array}{l} w_{old} - dt\, C_D(p_{new})\, A_{th}\, p_{atm}\left(\frac{\gamma}{R_{Gas}T_i}\right)^{\frac{1}{2}}\cdot \rightarrow \\ \rightarrow \cdot\left(\frac{2}{\gamma-1}\left(\left(\frac{p_{atm}}{p_{new}}\right)^{\frac{1-\gamma}{\gamma}} - 1\right)\cdot\left(\frac{p_i}{p_{atm}}\right)^{\frac{\gamma-1}{\gamma}}\right)^{\frac{1}{2}} \end{array}\right\}\right)^{\gamma} \tag{5.40}$$

From this, a function in terms of p_{new} can be determined by rearranging equation (5.40):

$$f(p_{new}) = p_{old}\left(\frac{1}{\rho_{old}V_{new}}\left\{\begin{array}{l} w_{old} - dt\, C_D(p_{new})\, A_{th}\, p_{atm}\left(\frac{\gamma}{R_{Gas}T_i}\right)^{\frac{1}{2}}\cdot \rightarrow \\ \rightarrow \cdot\left(\frac{2}{\gamma-1}\left(\left(\frac{p_{atm}}{p_{new}}\right)^{\frac{1-\gamma}{\gamma}} - 1\right)\cdot\left(\frac{p_i}{p_{atm}}\right)^{\frac{\gamma-1}{\gamma}}\right)^{\frac{1}{2}} \end{array}\right\}\right)^{\gamma} - p_{new} \tag{5.41}$$

- $\boldsymbol{f'(p_{new})}$

Using the chain rule, equation (5.41) can be differentiated, with the following result:

$$\begin{aligned} f'(p_{new}) = \frac{df(p_{new})}{dp_{new}} = \gamma\left(f\left(p_{new}\right) + p_{new}\right)^{\gamma-1} \cdot \rightarrow \\ \rightarrow \cdot \frac{-dtA_{th}p_{atm}}{\rho_{old}V_{new}}\left(\frac{\gamma}{R_{Gas}}T_i\right)^{0.5}\left(\frac{2}{\gamma-1}\left(\frac{p_i}{p_{atm}}\right)^{\frac{\gamma-1}{\gamma}}\right)^{0.5} \cdot \rightarrow \\ \rightarrow \cdot \begin{pmatrix} C_D(p_{new})\left(\left(\frac{p_{new}}{p_{atm}}\right)^{\frac{\gamma-1}{\gamma}} - 1\right)^{0.5} + \rightarrow \\ \rightarrow \ +0.5\ C_D'(p_{new})\left(\left(\frac{p_{new}}{p_{atm}}\right)^{\frac{\gamma-1}{\gamma}} - 1\right)^{-0.5} \cdot \left(\frac{\gamma-1}{\gamma}\right)\left(\frac{p_{new}}{p_{atm}}\right)^{-\frac{1}{\gamma}} \end{pmatrix} - 1 \end{aligned} \tag{5.43}$$

With this, equations (5.41) and (5.42) can be substituted into equation (5.37) and computationally implemented into an iterative scheme to obtain the pressure and gas solution over a given timestep.

CHAPTER 6: Application: Airbag design for the recovery of a rocket's first-stage

In this section we will obtain the proposal of a preliminary design for an Airbag based on the characteristics and behaviour of the first stage of the Ares I-X rocket. It is a completely invented approach, since the rocket does not actually have such an impact attenuation system. To do this we will use the concepts described in Chapter 5 and try to dimension the airbag system and its performance.

6.1. Airbag Sizing

Before beginning the design of the airbag, we must consider how the position of the airbag should be to fulfil its impact attenuation function.

Firstly, according to the recovery performance of the FS described in Section 4.1.1, the vehicle impacts with a completely vertical position at a speed of 21.64 m/s. The impact in this vertical position implies that the lower end of the vehicle suffers the greatest loads, i.e. most of the stresses are concentrated in the lower part of the vehicle and therefore suffer more damage than the upper end. For this reason it would be necessary to design a very robust attenuation system to absorb such loads.

It is physically more logical that the vehicle impacts the surface in a horizontal position, because with this the impact stresses are spread uniformly throughout the structure. In addition the airbag system in this case can be designed along the entire length of the vehicle and as a secondary function can work as a flotation system to prevent the sinking of the vehicle.

In short, the airbag design to be considered must attenuate the impact of the FS in horizontal position instead of vertical position. For this we must also design a mechanism that can change the vertical position of the FS to a horizontal position.

This mechanism can be another parachute system that is deployed at the lower end of the vehicle. This mechanism involves reconsidering the recovery action of the first stage in its final phase, i.e. once the main parachutes have been fully opened.

Therefore we must now consider that a second parachute system is deployed. To achieve a horizontal position, this parachute system must be identical to the main parachutes, i.e. a cluster of 3 parachutes of 45 meters in diameter and with the same drag area (4384.1 m^2).

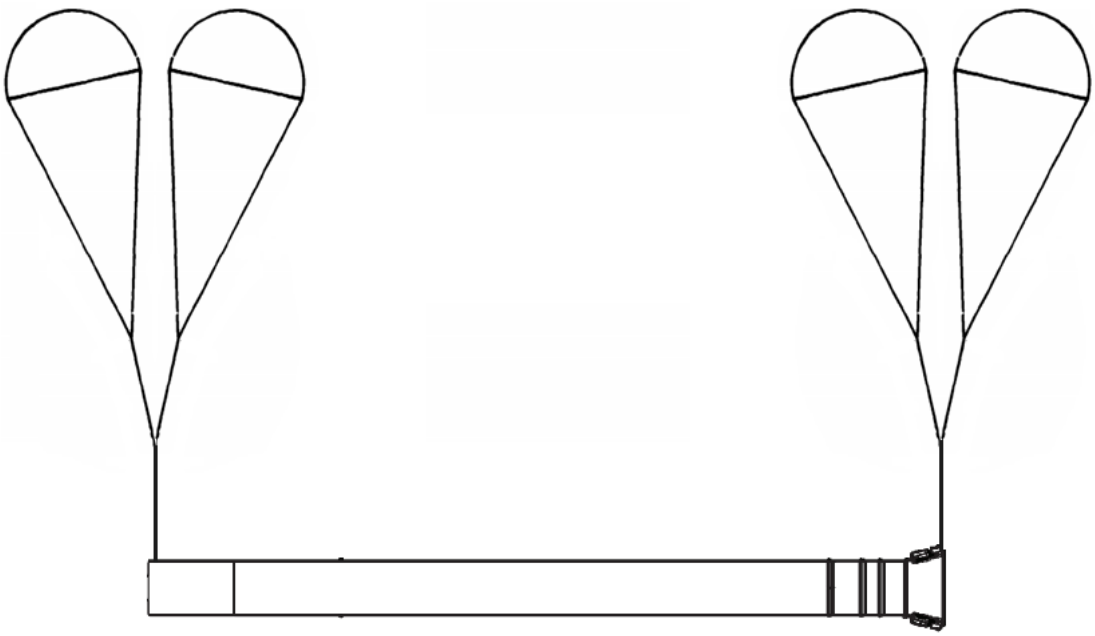

Figure 6.1. New Design of the Main Parachutes for the Final Descent.

With these two clusters of 3 parachutes, the speed of descent in equilibrium will be much smaller than the previous one (21.64 m/s). This speed is difficult to determine due to the oscillations that the vehicle can suffer until it stabilizes completely in horizontal position. Therefore to continue with the design of the airbag, we will assume that the parachute system descends in equilibrium from 200 meters and with a speed of 10 m/s.

6.2. Airbag performance

The first issue is to find the volume of air that the airbag needs to absorb all the energy of the impact. The method used to solve this problem is based on the thermodynamic analysis (section 5.2.1), with which we can study the energy state of the system in each of the three phases of the impact and we can obtain the required mass of air. For this we will consider certain assumptions based on other airbag impact attenuation systems, such as the Orion CEV airbag system [25].

The initial data considered in this case are those mentioned in the previous section ($v_1 = 10\,m/s$ and $z = 0\,m$). Regarding the Airbag, we will assume that the operating medium is atmospheric air that is in normal conditions with an initial pressure of 130 kPa. Table 6.1 shows the assumed values for the thermodynamic analysis based on the Orion CEV airbag system.

Parameter	Quantity	Rationale
Mass (m_{FB})	126000 kg	Mass of the First Stage Rocket after separation
Impact Velocity (v_1)	10 m/s	Impact Velocity of the First Stage Rocket
Airbag		
Operating Medium	Atmospheric Air	Most likely to be accepted as the operating medium for airbags located within the cabin environment.
Operating Temperature (T_1)	22 °C (295 K)	This is a reasonable approximation to the expected temperature within the cabin environment.
Initial Pressure (p_1)	130 kPa	Initial pressure of a candidate design for the airbag system of the Orion CEV.
Thermodynamic Properties of Operating Medium		
Internal Energy (u_1)	210.49 KJ/kg	Ideal gas property of air at 295 K
Enthalpy (h)	295.17 KJ/kg	Ideal gas property of air at 295 K
Specific gas constant (R)	0.2869 KJ/kgK	Standard value for air.

Table 6.1. Values assumed for the Thermodynamics Analysis [25].

With these values, the energy contribution of each component of the system can be calculated via the standard relationship for kinetic energy.

$$KE_{FB} = \frac{1}{2}\, m_{FB}\, v_1^2 \qquad ; \qquad KE_{gas} = \frac{1}{2} m_{gas} v_1^2 \quad ; \quad U_1 = m_{gas}\, u_1 \tag{6.1}$$

Where m is mass of the system, v is the vertical velocity, u_1 is the specific internal energy of the air and g is the gravitational acceleration.

Considering equation (5.9), the energy at the moment at which the airbag has attained its maximum compression is equal to the internal energy minus the kinetic energy at state 1.

$$U_2 = U_1 - \left(KE_{FB} + KE_{gas}\right) = m_{gas}\, u_1 - \left(\frac{1}{2}\, m_{FB}\, v_1^2 + \frac{1}{2}\, m_{gas}\, v_1^2\right) \tag{6.2}$$

$$U_2 = 210440 \left[\frac{J}{kg}\right] m_{gas} - 6.31 \cdot 10^6 [J] \tag{6.3}$$

Finally the system will have zero energy at the end, signifying a complete attenuation of the impact energy. To obtain this we will consider that $U_3 = 0$ and with this we can obtain the required volume of air within the airbags.

$$U_3 = 0 = U_2 \rightarrow\rightarrow\ 0 = 210440 \left[\frac{J}{kg}\right] m_{gas} - 6.31 \cdot 10^6 [J] \rightarrow\ \boldsymbol{m_{gas} = 29.98\ kg} \tag{6.4}$$

Since the operating medium is assumed to behave as an ideal gas, the Ideal Gas Law can be used to determine the volume of air in the airbag. This is given by equation (5.20):

$$V_{gas} = \frac{m_{gas} R\, T_1}{p_1} \quad \rightarrow \quad \boldsymbol{V_{gas} = 19.52\ m^2} \tag{6.5}$$

As we can observe the minimum value of the initial volume required to absorb the impact energy is a very low value. This is because the vehicle already descends with a sufficiently low speed and therefore the energy of impact is considerably low.

However as our goal is that the airbag system could have a second function of flotation system, it seems obvious that with this volume the first stage will sink. For this reason we must analyse what is the minimum volume that the airbag must have to keep the first stage afloat.

Applying the Archimedes principle, the weight of the displaced water volume equals the flotation force.

$$\rho_{water} \cdot V_{sink} \cdot g = F_{flotation} \tag{6.7}$$

In this case as a requirement we will impose that the submerged volume of the airbag should be at most half, that is $V_{sink} = V_{bag}/2$. Therefore from the equation of equilibrium of forces we can obtain the required volume to maintain the FS afloat:

$$mg = F_{flotation} = \rho_{water} \cdot V_{bag}/2 \cdot g \quad \rightarrow \quad V_{bag} = 2\, m/\rho_{water} \tag{6.8}$$

$$V_{bag} = 2 \cdot \frac{126200}{1000} \quad \rightarrow \quad \boldsymbol{V_{bag} = 252.4\, m^3} \tag{6.9}$$

The required initial volume must be larger enough to reach a final volume of $252.4\, m^3$. This problem can be solved simply by assuming a coherent initial volume value, then applying the equations necessary to obtain the final volume value, and if this latter value is less than the minimum volume required for the flotation, we must correct the initial value until the condition is fulfilled. For this we will use the mathematical program Matlab, which will help us to estimate this volume much faster.

First of all we will consider that:

- Two airbags are located at the ends of body of the first stage .
- The airbag geometry is an orthohedron of height h, total length l and width w.
- The length of the air bag is 6 meters for each airbag and remains constant.
- The value of the airbag width varies.
- The height of the airbag varies with time.

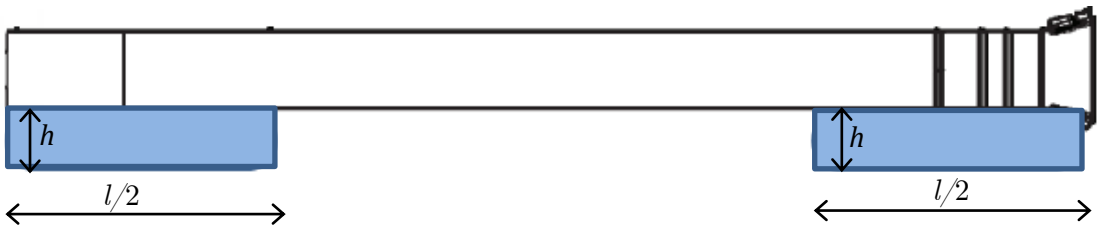

Figure 6.2. Proposal of Airbag System Design.

To simplify the calculations we will consider a single airbag with a length of 12 meters.

Figure 6.3. Simplified Arbag System Design.

As a first step we will consider that the initial volume is $V_i = 300\,m^3$ and that the initial height of the airbag is $h_i = 3\,m$ and the length of the airbag is $l = 12\,m$, which remains constant. Taking into account that the volume of the Airbag can be expressed as follows:

$$V_i = \left(\pi \frac{h^2}{4} + h\,w\right) \cdot l \tag{6.10}$$

Rearranging the terms of the equation (6.10) we can obtain an expression of the width as a function of the height.

$$w = \left(\frac{V_i}{h \cdot l} - h\frac{\pi}{4}\right) = \frac{25}{h} - 0.7854\,h \tag{5.11}$$

Therefore, if we considered that the initial height of the airbag is h_i=3 meters, the initial width will be w=5.97 meters.

With these values we can calculate the evolution of the pressure by using the Matlab program, with which we can calculate the pressure in every timestep. The code created to model this consists on the following steps:

1) Calculate the velocity change and the new velocity.

$$\Delta v = \frac{A_{FP}\,p_{atm}\,\Delta t}{m_{FB}}\left(\frac{p_{bag}}{p_{atm}} - 1 - \frac{m_{FB}\,g}{A_{FP}\,p_{atm}}\right) \quad \rightarrow \quad v_{new} = v_{old} + \Delta v \tag{6.12}$$

2) Calculate the height change and thereby define the new height of the airbag.

$$dt = 0.002\,s \;\rightarrow\; dh = v_{new}\,dt \;\rightarrow h_{new} = h_{old} - dh \tag{6.13}$$

3) Calculate the new volume of the airbag system.

$$L_{FP} = \frac{\pi}{2}(h_{old} - h_{new}) + w_{old} \tag{6.14}$$

$$A_{xsection} = \pi \frac{h_{new}^2}{4} + h_{new}\,L_{FP} \tag{6.15}$$

$$V_{new} = l \cdot A_{xsection} \tag{6.16}$$

4) Calculate the new pressure of the enclosed air.

$$p_{new} = p_{old}\left(\frac{\rho_{new}}{\rho_{old}}\right)^{\gamma} = p_{old}\left(\frac{V_{old}}{V_{new}}\right)^{\gamma} \tag{6.15}$$

5) Repeat this process until the velocity of the vehicle is zero.

After calculating the final pressure of the attenuation process, we must check if the final volume is greater than the minimum volume necessary to maintain the flotation of the first stage. In this case we obtain that the final volume is $V_{fin} = 181.15\, m^3$,, which is less than the required volume. Therefore we must repeat the same procedure now considering an initial volume greater than $300\, m^3$.

Finally iterating, it is obtained that the initial volume should be $\boldsymbol{V_i = 386\, m^3}$, for the particular case in which the initial pressure is 130 kPa.

The following graphs are obtained:

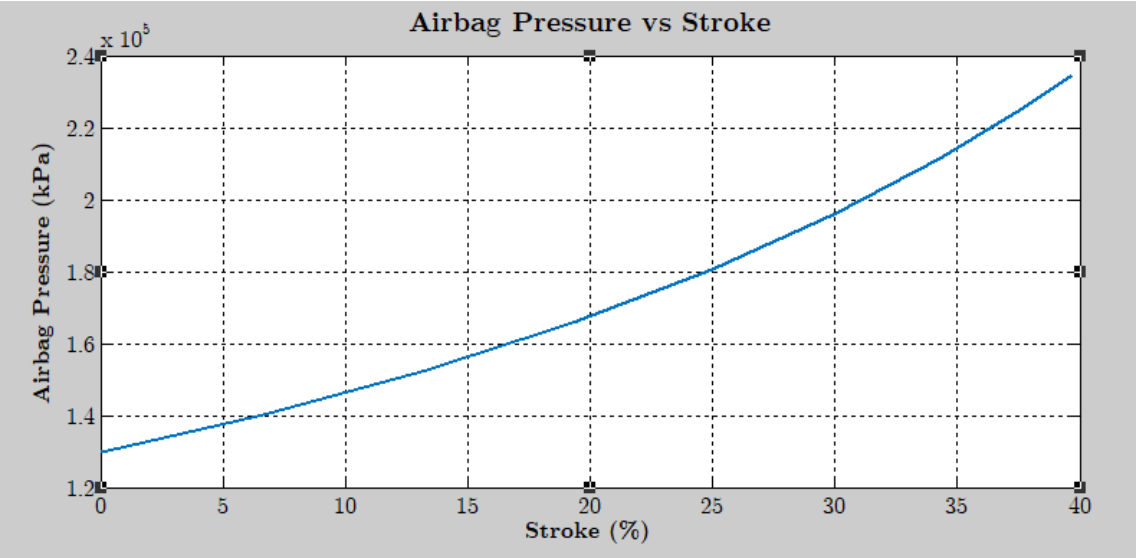

Figure 6.4. Airbag Pressure vs Stroke.

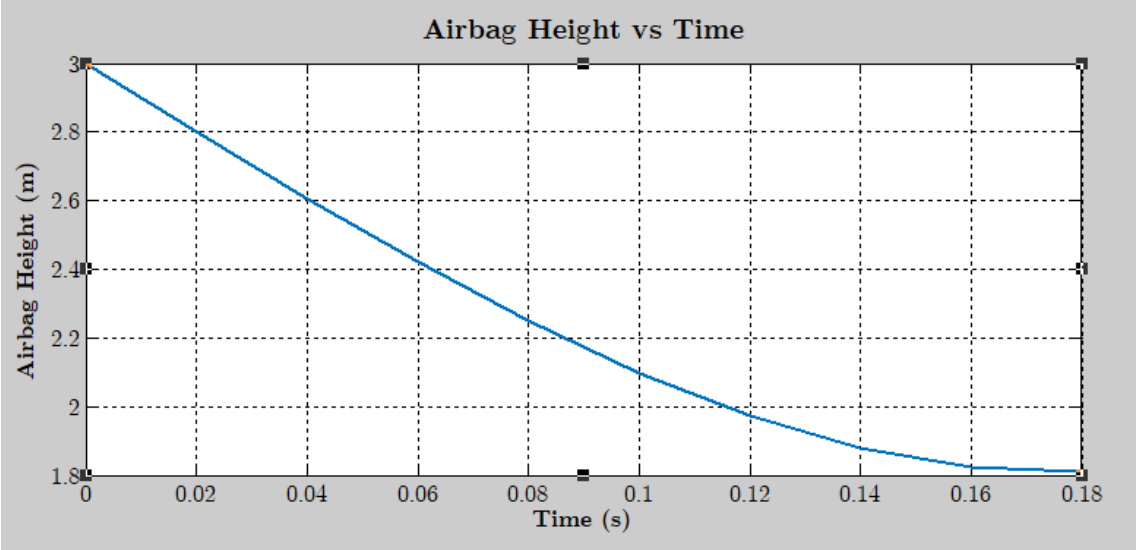

Figure 6.5. Airbag Height vs Time.

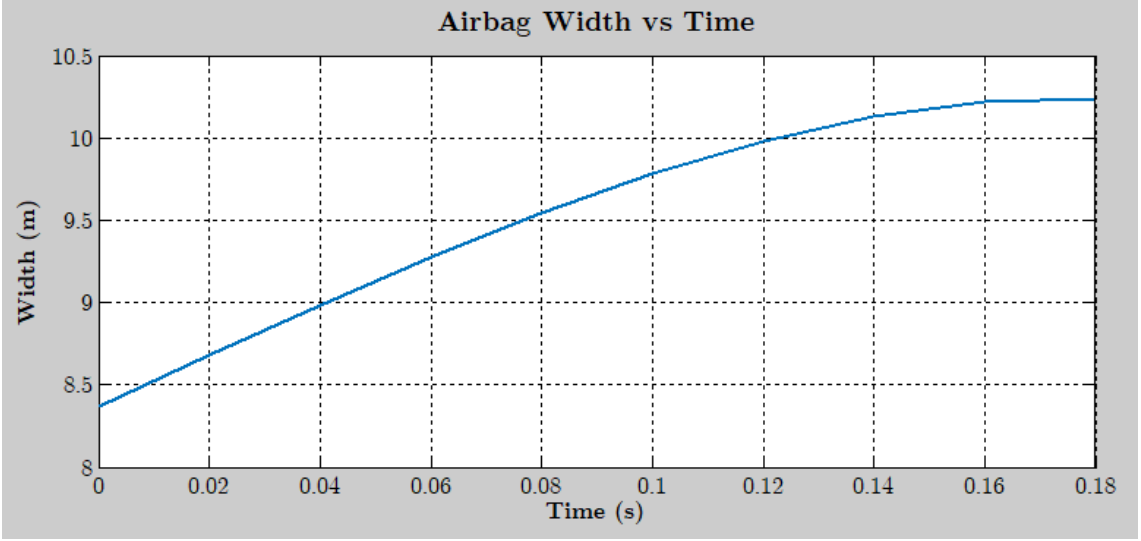

Figure 6.6. Airbag Width vs Time.

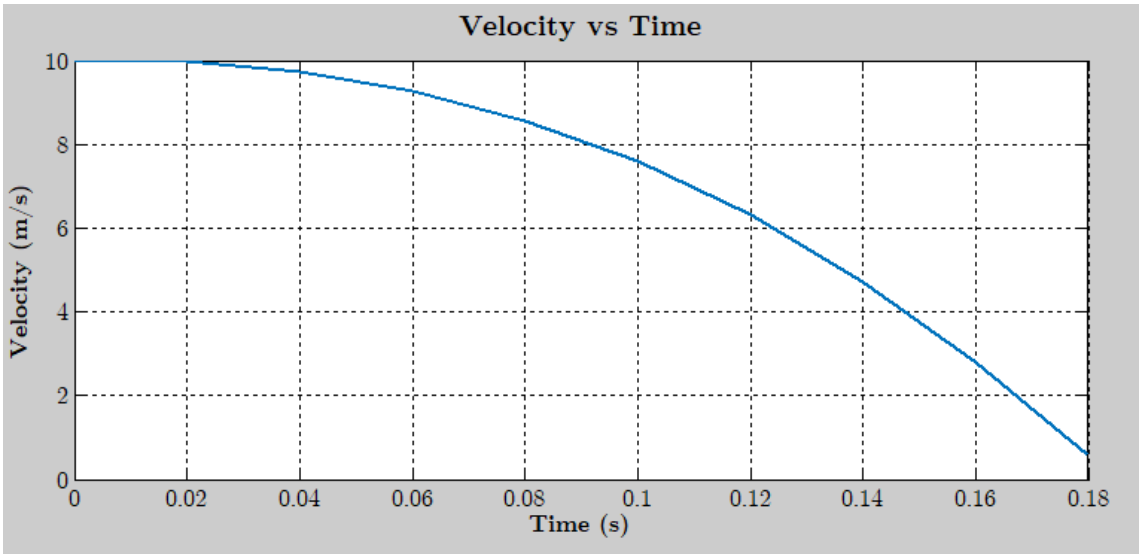

Figure 6.7. Velocity vs Time.

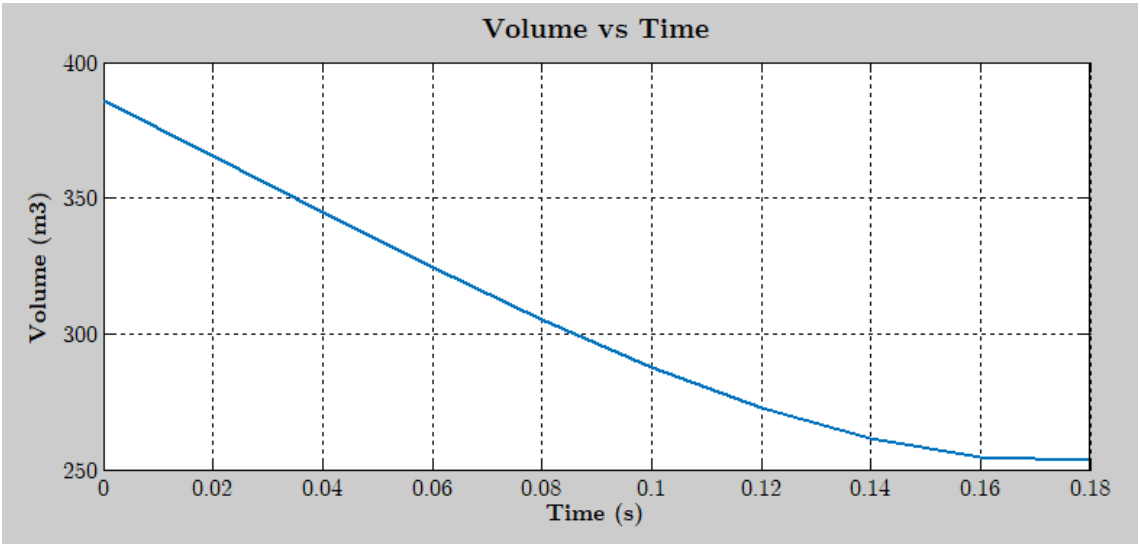

Figure 6.8. Volume vs Time.

Como se puede observar en estas gráficas, tras una reducción de la altura del airbag de $\mathbf{39.65\%}$, la primera etapa alcanza el reposo y la presión del airbag es $\mathbf{2.34 \cdot 10^5\ Pa}$. Estos valores se alcanzan en un periodo de tiempo de $\mathbf{0.18\ s}$, donde los valores finales de la altura y la anchura del airbag son $\mathbf{1.81\ m}$ y $\mathbf{10.23\ m}$ respectivamente, lo cual da lugar a un volumen final de $\mathbf{253.24\ m^3}$.

If we consider now that the airbag has the same initial height and length ($h_i = 3\,m\,, l = 12\,m$) but the initial pressure of the airbag is $\mathbf{150\ kPa}$ instead of $130\,kPa$, we can analyse what is the influence of having a higher initial pressure. For this we must apply again the whole procedure described previously and the new values obtained are presented in Table 6.2 together with the values of the previous case:

Initial Pressure	130 kPa	150 kPa
Final Pressure	234 kPa	2.42 kPa
Initial Volume	386 m3	357 m3
Final Volume	253.24 m3	253.26 m3
Initial Height	3 m	3 m
Final Height	1.81 m	1.96 m
Intial Width	8.36 m	7.56 m

As we can see in Table 6.2, the final pressure of the airbag is greater if the initial pressure is too. The final volume is the same in both cases because the volume of flotation does not depend on the pressure of the airbag, however the final dimensions of the airbag are different, since in the second case the airbag deforms less and therefore the final height is higher and the final width is smaller than the first case. In respect of the attenuation time, the second case requires less time. And finally, the mass of air required for the second case is greater than for the first one.

With all these data we can deduce that designing an airbag with less pressure is more appropriate than designing it with more initial pressure, mainly for reasons of weight. However, it must also be taken into account that in the first case the initial volume is higher, which means that a larger airbag needs to be built which can increase the weight. Therefore the choice between both cases also depends on the material used to build the airbag system. On the one hand, it would be necessary to consider whether the reduction of the mass of air of the first case is not affected by the additional weight of the airbag, and on the other hand it would be necessary to analyse if the material with which the air bag is manufactured is capable of deforming until reaching the desired final values of altitude and width.

CHAPTER 7. Conclusions

The main objective of this project was to carry out the preliminary design of the recovery system of the first stage of a rocket. This recovery system was based on the design of two main subsystems: the Parachute System and the Airbag System.

The design of the parachute system was based on a real parachute system used to decelerate the first stage of the Ares X-I rocket. According to the data collected from this application, we can conclude that the procedure used to calculate the required parachute dimensions is adequate, since it is very close to the real case.

On the other hand, both the filling time and the estimated opening forces could not be compared with the real values due to lack of information, but the experience with other similar parachutes allows us to deduce that the estimated values are reasonable and sufficient for the preliminary design, since they allow us to choose the material or materials to manufacture the parachute system. However the time of inflation and the opening forces are critical parameters that determine the success or failure of the parachute performance, and therefore in a later refinement of the design would be necessary to perform tests to ensure reliability.

Similarly, the parachute mass estimation was based on the correlation of mass values of other parachutes. This method allows us to obtain the weight of the canopy in a fast and effective way in preliminary design tasks. But the result of the weight estimation obtained in this preliminary design phase is a very approximate value of the real one, whose uncertainty depends fundamentally on the choice of materials of all the components of the parachute. Therefore only from the last stages of design it can be possible to obtain a more accurate estimate of this parameter, since a list of all the components of the parachute with their dimensions and materials would require.

The design of the impact attenuation system is not included in the Ares I-X rocket recovery system, but taking advantage of this example, it was proposed a possible airbag system design that could be installed in the first stage of the rocket. The purpose of this preliminary design was to check numerically the airbag behaviour described in the theory and with this to validate the assumptions made. It was necessary to modify the final phase of descent to be able to integrate a feasible airbag system. For this purpose, a mechanism was included which consisted of an additional parachute system to rotate the first stage from a vertical position to a horizontal position. Despite the difficulty of modelling the airbag performance, it was possible to obtain a sufficiently consistent impact attenuation system as a preliminary design. To do the design of the airbag we didn't consider the venting mechanism, but in a later refinement of the design it would be necessary to study in detail the process of attenuation, because the airbag really has a spring effect that makes the body oscillate, and the system of relief valves is precisely the responsible for dampening this movement.

Appendix A

A.1. High-Performance Parachute Types

Type	Constructed shape	Inflated Shape	Drag Coefficient	Average Angle of Oscillation	Opening Load Factor	General Application
	D_c/ D_0	D_P/ D_0	CD_0 (D_0)	Degrees	C_X	
Flat circular	1.00	0.67 to 0.70	0.75 to 0.80	±10 to ±40	~1.8	Descent
Conical	0.93 to 0.95	0.70	0.75 to 0.90	±10 to ±30	~1.8	Descent
Biconical	0.90 to 0.95	0.70	0.75 to 0.92	±10 to ±30	~1.8	Descent
Estended Skirt (10%)	0.86	0.66 to 0.70	0.78 to 0.87	±10 to ±15	~1.4	Descent
Extended Skirt (14.3%)	0.81	0.66 to 0.70	0.75 to 0.90	±10 to ±15	~1.4	Descent
Hyperflo	0.71	0.66	0.62 to 0.77	±10 to ±15	~1.6	Descent
Guide Surface (Ribbed)	0.63	0.62	0.28 to 0.42	0 to ±2	~1.1	Stabilization Drogue
Guide Surface (Ribless)	0.66	0.63	0.30 to 0.34	0 to ±3	~1.4	Pilot, Drogue
Cross	1.15 to 1.19	0.66 to 0.72	0.60 to 0.78	0 to ±3	~1.2	Descent, Deceleration
Flat Ribbon	1.00	0.67	0.45 to 0.50	0 to ±3	~1.05	Pilot, Drogue, Deceleration, Descent
Conical Ribbon	0.95 to 0.97	0.70	0.50 to 0.55	0 to ±3	~1.05	Pilot, Drogue, Deceleration, Descent
Hemisflo Ribbon	0.62	0.62	0.30 to 0.46	±2	1.00 to 1.30	Supersonic drogue
Ringslot	1.00	0.67 to 0.70	0.56 to 0.65	0 to ±5	~1.05	Extraction, Deceleration, Descent
Ringsail	1.16	0,69	0.75 to 0.90	±5 to ±10	~1.10	Decent
Disc-Gap-Band	0.73	0.65	0.52 to 0.58	±10 to ±15	~1.30	Supersonic, Drogue, Descent
Hyperflo	1.00	0.80	0.35 to 0.44	0 to ±3	1.20 to 1.50	Supersonic, Drogue.

A.2. Skechtes and Applications

Solid Cloth Parachtues		
Flat Circular Parachutes	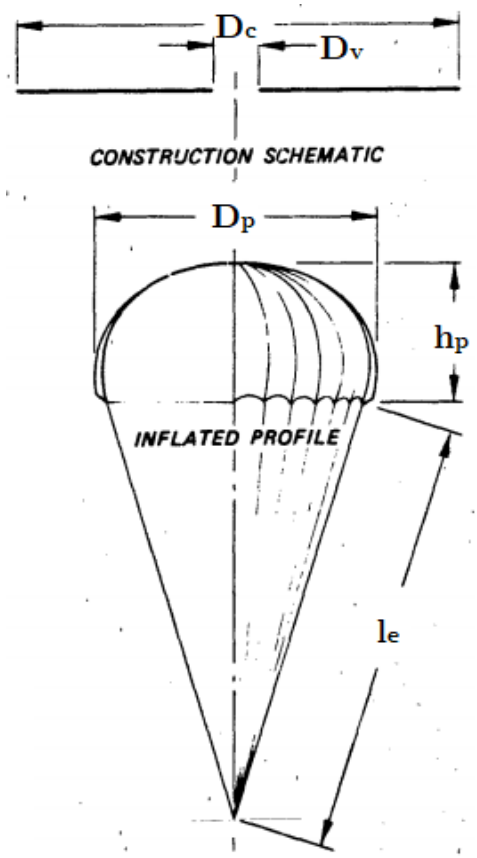	The canopy is a regular polygon of N sides, constructed as a flat surface with a central vent. Its design is the basis for most circular parachutes, other types being variations in gore pattern and general geometry. Flat circular parachutes are simple and economical to construct, handle and inspect, and are often used in clusters. They are in wide use for personnel and airdrop applications. This parachute is very reliable.
Conical Parachutes	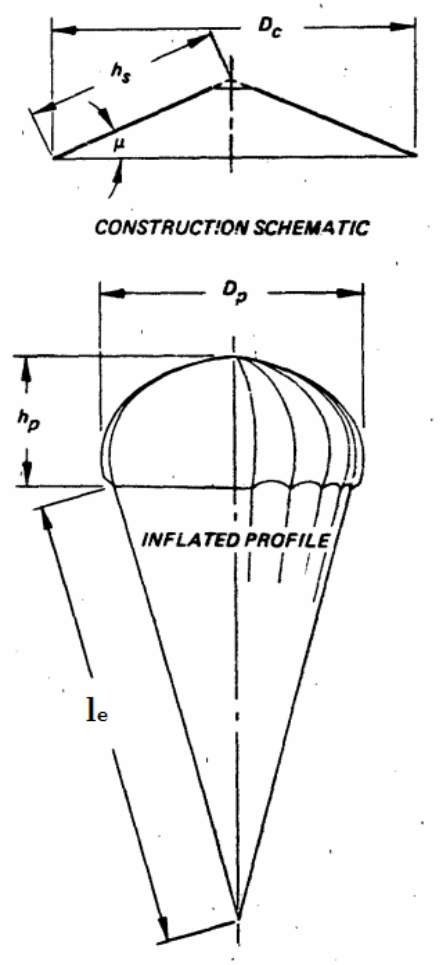	The canopy is constructed as the surface of a regular pyramid of N sides and base angle μ. Its design is a minor variation of the flat circular canopy. The conical parachute is as simple and economical to construct, handle and inspect as the flat circular and serve similar applications. As a result of drop tests with models conducted in 1949, conical parachutes with up to 30^{o} cone angles showed approximately 10% higher drag than solid flat parachutes of the same surface area.

Biconical Parachutes	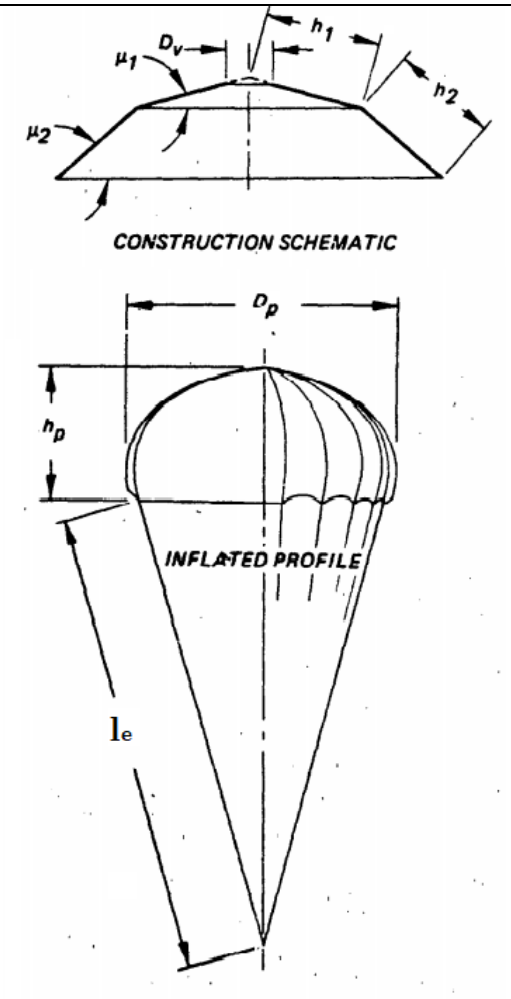	The canopy is constructed as the surface of a regular pyramid and a pyramid frustum of N. Its design is a variation of the conical canopy. The biconical parachute is reasonably simple and economical to construct. It serves applications which are typical for flat circular parachutes with better stability and drag performance.
Extended Skirt Parachutes	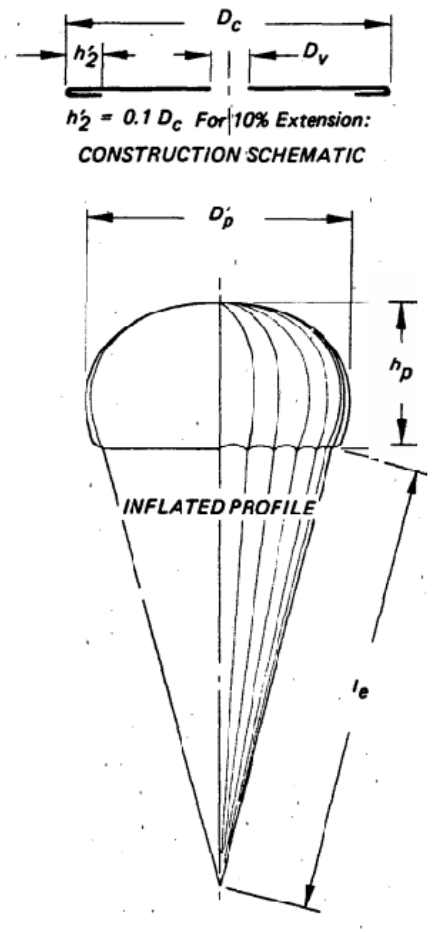	The canopy is characterized by a flat polygonal surface to which is added an extension in the form of an annular flat ring of a width designated as a percent of the flat surface diameter as illustrated by the construction schematic. A 10% extension has proven a common choice, although 12.5 and 14% extensions have been also tried successfully. Flat extended skirt canopies are more complex to design, but with proper patterns they are no more complicated to form and assemble than the flat circular. Extended skirt parachutes have slightly higher drag, longer filling times and lower opening forces than flat circular parachutes of identical S_o.

Hemispherical Parachutes	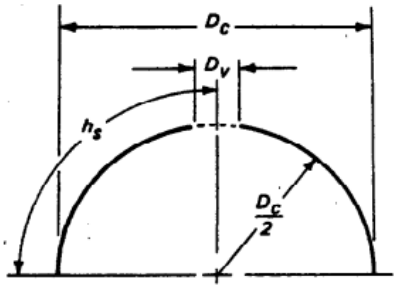 CONSTRUCTION SCHEMATIC 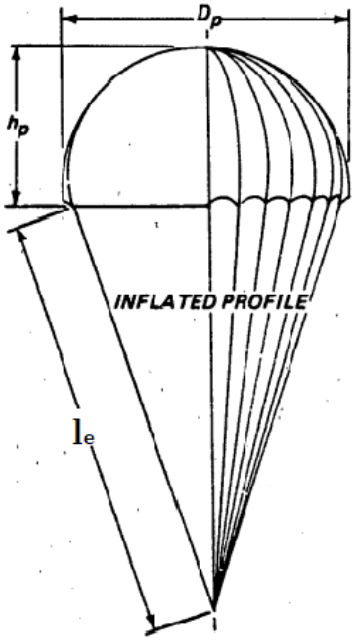	The constructed shape of this canopy is a hemispherical surface. The gore is designed so that the flat width dimension is the horizontal arc distance between radial seamlines. The inflated shape approaches the constructed profile under load. The hemispherical parachute is more stable than the flat circular type and is used primarily for airdrop of supplies.
Ribbed Guide Surface Parachutes	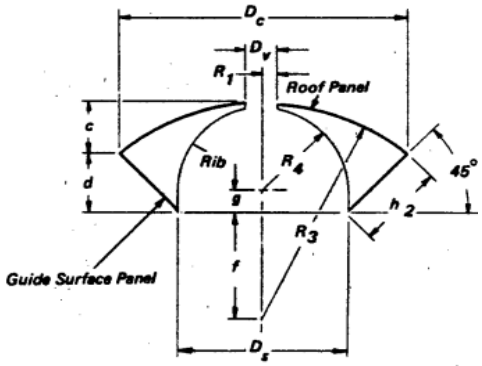 CONSTRUCTION SCHEMATIC 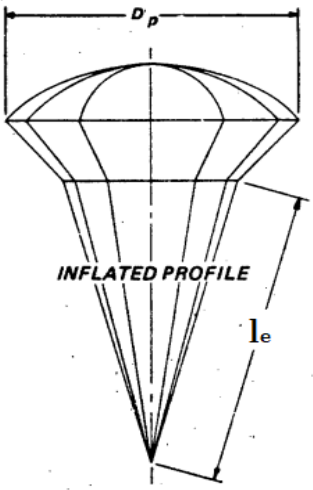	The canopy is constructed with a slightly rounded crown or roof, and an inverted conical front or "guide surface" extending from roof edge to skirt hem. Ribs, placed between gores in a plane with the suspension lines, help to maintain the constructed profile during operation. The guide surface parachute was specifically developed as a stabilization device for bombs, mines, torpedoes and similar bodies. Its good stability comes from the abrupt flow separation edge of its largest diameter and the guide surface slope of the skirt. Low porosity cloth is used in the roof and guide surfaces to promote fast inflation and to help maintain its characteristic shape. The ribbed guide surface parachute is reliable and very stable. However, it has a low drag coefficient and is difficult to manufacture.

Ribless Guide Surface Parachutes	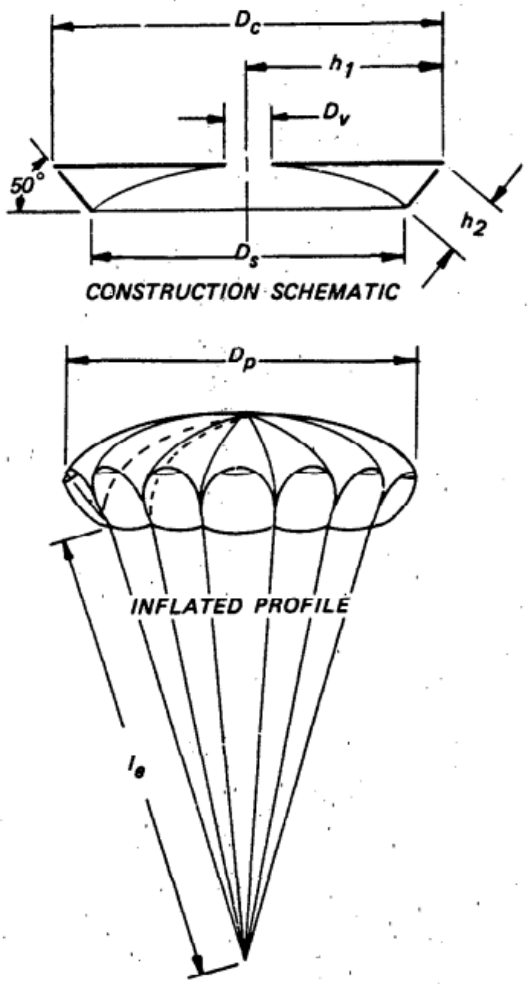	In the ribless guide surface canopy, the desired shape is obtained by modifying the gore outline. The roof panel is widened to extend around the edge of the guide surface panel to the skirt edge, eliminating the rib. The resulting flow-separation edge is less abrupt, accounting for a slightly higher oscillation angle than the ribbed version. A slit vent at the outer edge of each guide surface panel also helps to promote flow separation. Construction is simplified by avoiding the rib. Dimensions for roof and guide surface panels depend upon diameter and the number of gores in the canopy.
Cross Parachutes	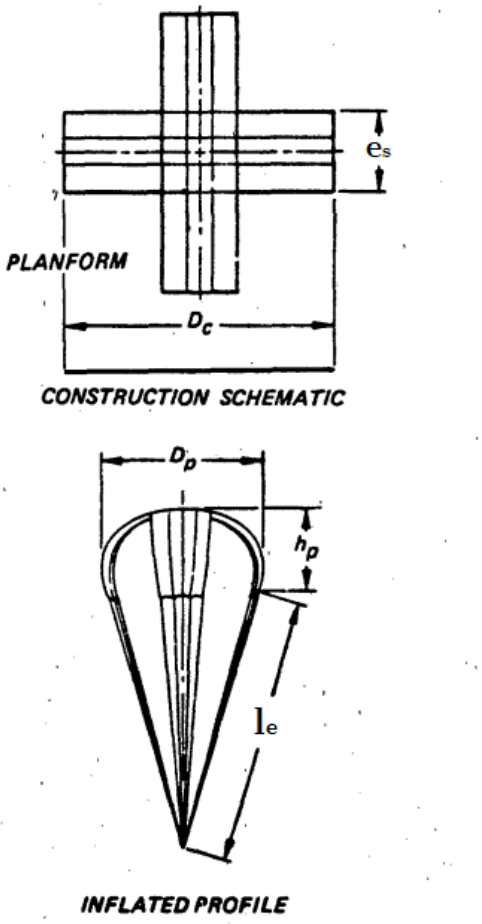	The cross parachute, a French development, is finding increased use for deceleration in applications that require good stability and low cost. The design is simple. The carnopy consists of two identical cloth rectangles, crossed and joined to each other at the square intersection “t” fcrm a flat surface having four equal arms. Suspension lines are attached to the outer edges of four arms. The Cross parachute is similar in stability performance and drag efficiency to the ringslot parachute, but it has a tendency to rotate. It is popular as a deceleration perachute for ground vehicles. Recent applications include stabilization and deceleration of air dropped n3val weapons and low rate of descent, high altitude experiments.

Slotted Canopy Parachutes

Flat Circular Ribbon Parachutes

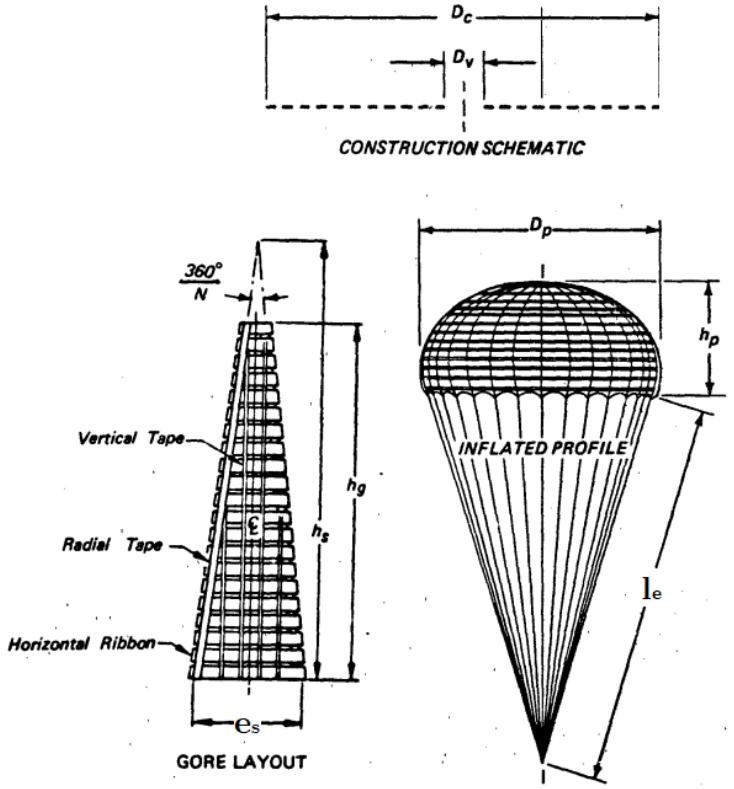

The canopy is a flat circular design and consists of concentric ribbons, usually 2 inches in width, supported by smaller horizontally spaced tapes and radial ribbons at gore edges. Ribbons and tapes are accurately spaced to provide the desired ratio of open space to solid fabric over the entire canopy. Gores are triangular and their dimensions are determined in the same manner as for the solid cloth flat circular parachute. The flat circular ribbon parachute has a lower drag efficiency than the solid cloth parachutes. However, its stability is excellent and the maximum opening force is low in comparison. The canopy is relatively slow in opening and its performance reliability depends on specific design parameters. Compared to solid cloth parachute canopies, the flat circular ribbon canopy is more difficult to manufacture.

Conical Ribbon Parachutes

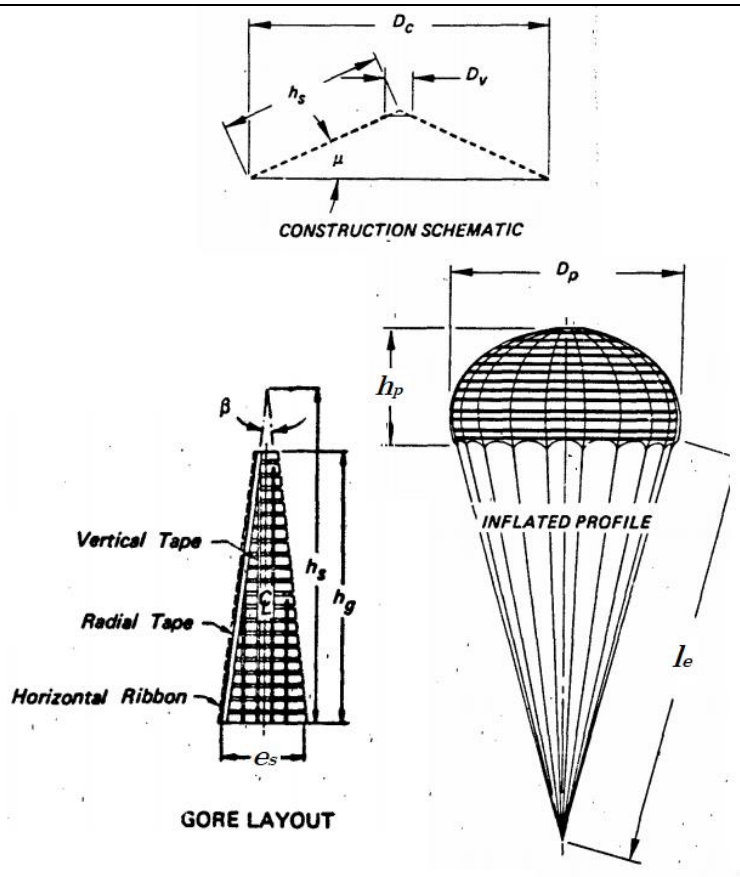

The constructed shape of this canopy is obtained in the same manner as that described for solid cloth conical parachutes. Gores, like the flat circular ribbon design, are composed of a grid of horizontal ribbons spaced and retained at close intervals by narrow vertical tapes. Radial tapes which extend from the vent to the skirt are sewn together in the joining of adjacent gores.
The conical ribbon parachute shows higher drag than the flat circular ribbon just as the solid cloth conical parachute does over the solid flat parachute of equal area.

Hemisflo Ribbon Parachutes	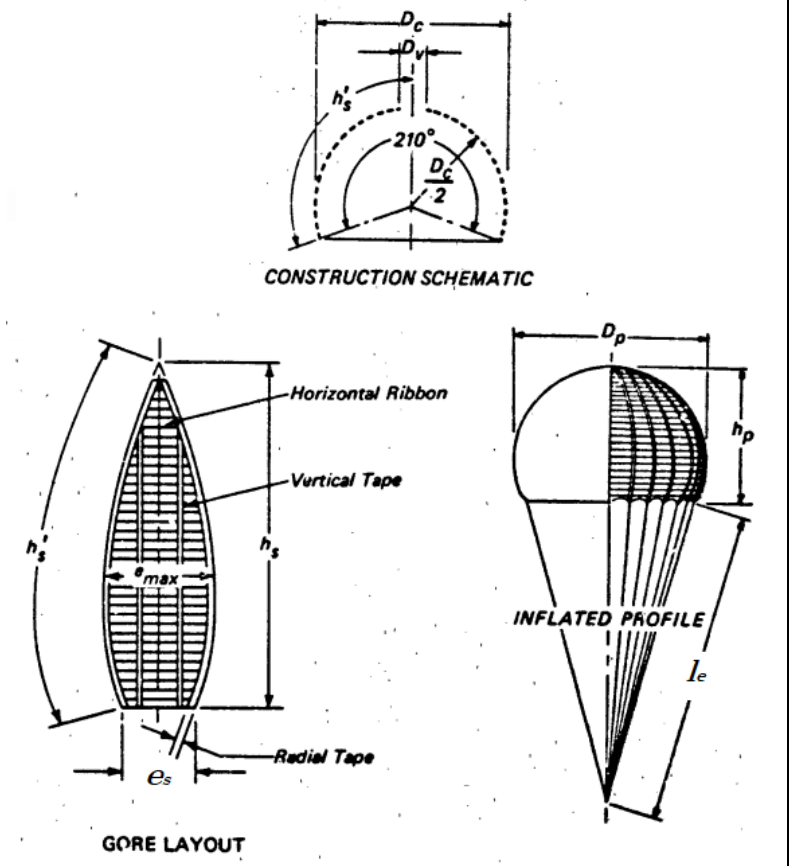	The constructed shape of this canopy is a spherical surface which continues 15 degrees past a hemisphere at the skirt as shown. The canopy design retains effective drag and stability performance over the range from Mach 1.5 to 2.5, although conical ribbon parachutes are as good or better at speeds below Mach 1.5. Hemisflo parachute is used almost exclusively for drogue applications which require stabilization and retardation at supersonic speeds.
Ringslot Parachutes	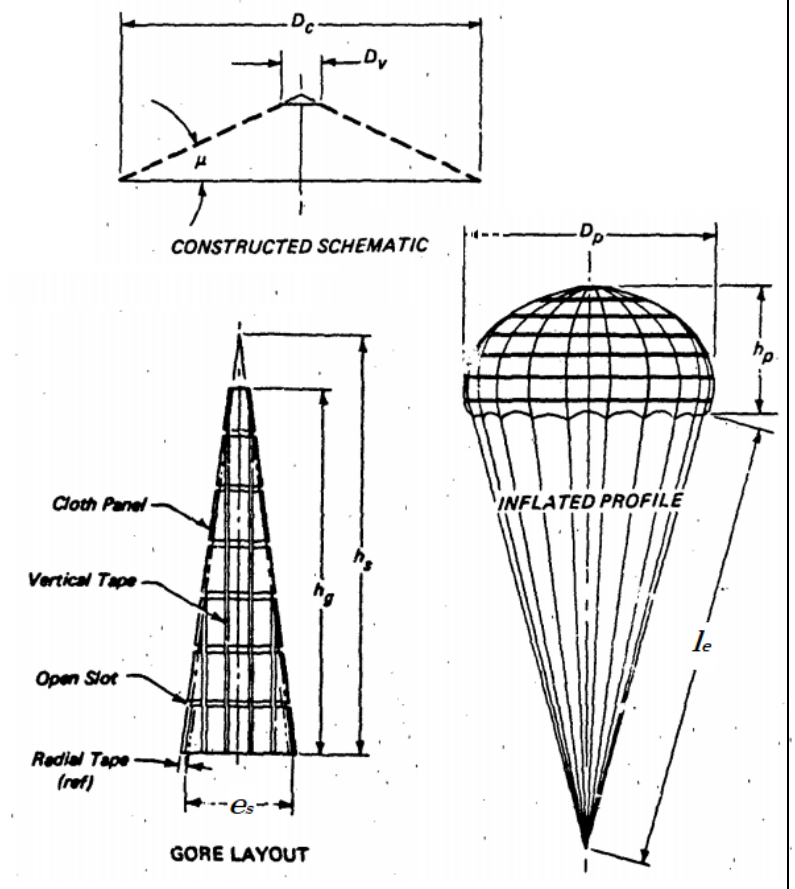	This parachute exists in flat and conical designs. The canopy is constructed of wide concentric cloth strips with intervening slots in a manner similar to the assembly of ribbon designs. Fewer operations are required, simplifying manufacture and reducing cost compared with ribbon parachutes. Performance characteristics are between those of the ribbon and solid cloth types. Ringslot parachutes are being used for aircraft landing deceleration, extraction of air drop equipment and final recovery parachutes. Opening reliability is comparable to ribbon parachutes

Ringsail Prachutes	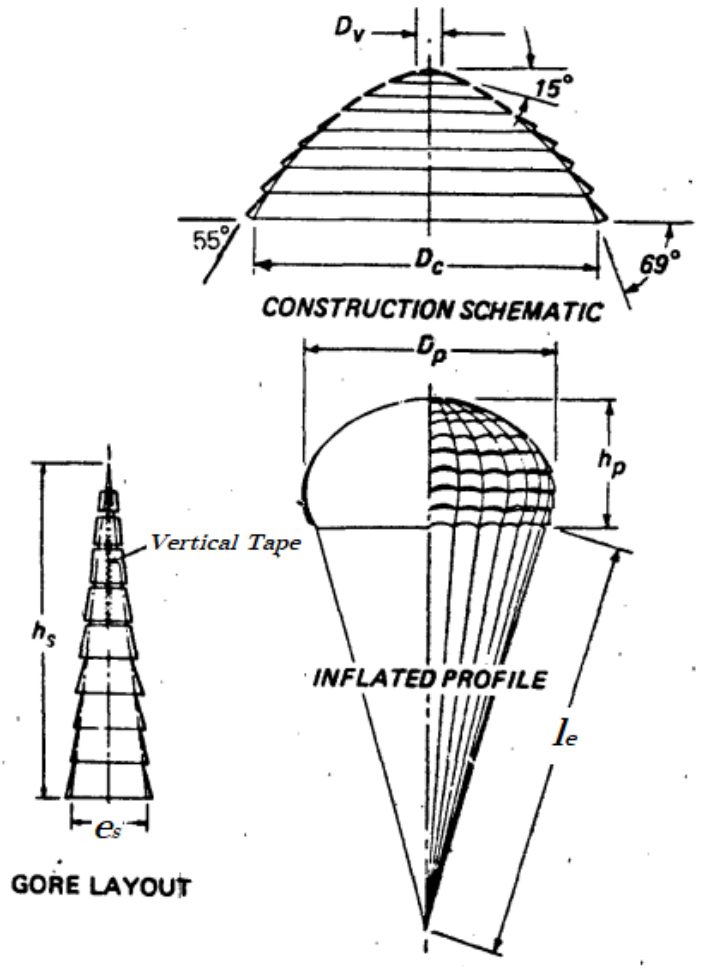	This parachute design is complex and develops a unique shape from the ccmbination of a curved basic profile and fullness at the leading edge of annular cloth rings. The constructed profile is a circular arc, tangent to a 15° cone at the apex and tangent to a 55° cone at the skirt edge. The ringsail canopy is constructed of wide concentric cloth strips, spaced apart in the upper crown with slots like the ringslot, but adjacent over the remainder of the canopy, obtaining geometric porosity through crescent-shaped slots resulting from the cloth dimension between radials being longer for the leading edge of each sail than the trailing edge of the sail below it.
Disk-Band-Gap parachutes	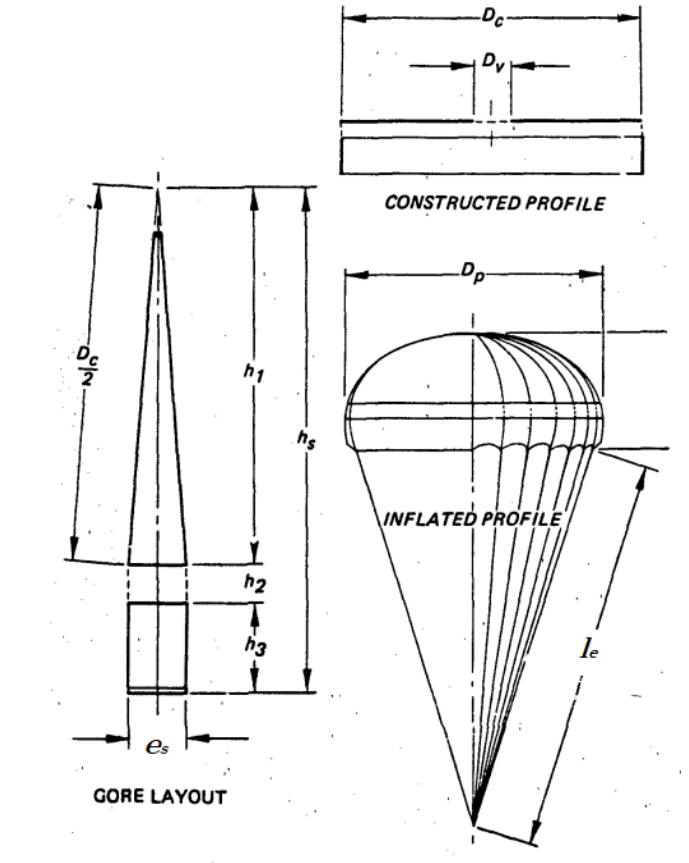	The disk-gap-band parachute was developed to operate at very low dynamic pressures at high altitudes and supersonic speeds. This parachute is designed to have better stability than a solid flat canopy without loss of drag efficiency. The right-angle change from the band to the disk portion of the canopy provides a discontinuity in the surface shape and causes the interior airflow to become separated around the edge at all times. By adjusting the width of the gap, the inside airflow of the canopy can be controlled to maximize the drag and maintain the stability.

Hyperflo Parachute	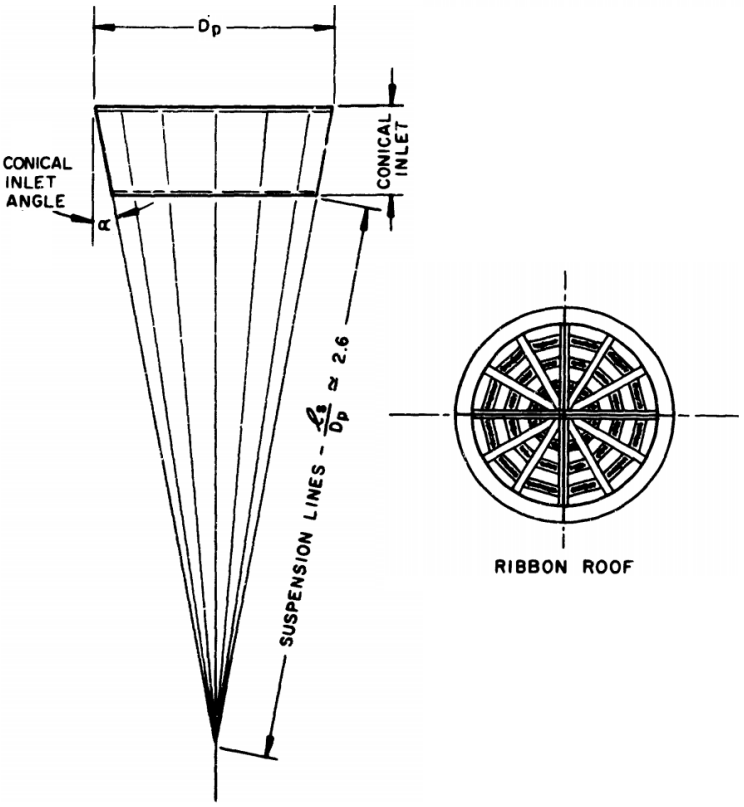	The Hyperflo type parachute is a shaped parachute with a design geometric shape like an inverted right conical frustum. The decrease in drag coefficient in the low supersonic speed regime is somewhat compensated by an increase in the projected canopy area in this regime, giving the effect of essentially constant drag area. This is obviously a desirable characteristic and an indication of satisfactory decelerator performance at an operational combination of low supersonic velocity and dynamic pressures approaching 140 kPa.

Characteristic	Dimensions	Silk	Cotton	Rayon	Nylon	Dracon	Kevlar	Glass fiber
Staple length	mm	400 - 1400 m	120 - 630	Continuous	Continuous	Continuous	Continuous	Continuous
Tensile strength	Kg/cm^2	-	-	-	8300	8400	26000	24500
Tenacity	gr/denier	3,8 - 5,2	2,1 - 6,3	1,5 - 5,0	6 - 9	6 - 9	20 - 22	7,7
Specific weight	gr/cm^3	1,34	1,52	1,5	1,14	1,38	1,44	2,54
Ultimate elongation	%	13 - 31	3 - 7	15 - 25	25 - 40	12 - 20	3 - 5	3
Melting point	^{0} C	150	230	170 - 230	248	252	454	730
Filament diameter	mm	0,0005	$<$ 0,001	0,0005	0,001	0,001	0,0005	0,0005
Wet strength	%	75 - 95	110 - 130	45 - 55	85 - 90	95	100	95 - 100
Resistance to:	P=poor G=good E=excellent	-	-	-	-	-	-	-
Ultraviolet rays		P	G	P	P	G	D	E
Storage, aging		G	G	G	E	E	G	E
Fungus, bacteria		P	P	P	G	G	G	E
Flame		P	Burns	Burns	G	G	G	E

References

[1] National Oceanic and Atmospheric Administration, NASA, U.S. Air Force: "*U.S. Standard Atmosphere*". Documents Stock No. 003-017-00323-0, Washington, D.C. 20402, 1976.

[2] Theo W. Knacke: *"Parachute Recovery Systems Design Manual"*. Naval Weapons Center, China Lake, California NWC TP 6575, 1992.

[3] D. J. Cockrell: *"The Aerodynamics of Parachutes"*. AGARDograph No.295, Universty of Leicester, United Kingdom, July 1987.

[4] E. G. Ewing, H. W. Bixby, and T. W. Knacke, "*Recovery Systems Design Guide*". USAF AFFDL-TR-78-151, December 1978.

[5] R.C. Maydew and C. W. Peterson: *"Design and Testing of High-Performance Parachutes"*. AGARDograph No. 319, Sandia National Laboratories, Albuquerque, New Mexico 87185, U.S. November 1991.

[6] W. L. Garrard, M. L. Konicke, K. S. Wu, and K. K. Muramoto: *"Measured and Calculated Stress in a Ribbon Parachute Canopy"*. AIAA Journal of Aircraft, Vol. 24, No. 2, pp. 65 to 72, February 1987.

[7] W.D. Sundberg: *"A New Solution Method for Steady-State Canopy Structural Loads"*. AIAA Paper. (AIAA 86-2489 CP).

[8] K. E. French: *"A New Correlation of Parachute Weight Data"*. AIAA Journal of Spacecraft and Rockets, Vol. 8, No. 1, pp. 71-72, January 1971.

[9] W. Mueller: *"Parachutes for Aircraft"*. National Advisory Committee for Aeronautics, NACA TM-450, October 1927.

[10] F. N. Scheubel: *"Notes on the Opening Shock of a Parachute"*. Progress Report IRE-65, Foreign Exploitation Section, Intelligence (T-2), April 1946.

[11] K. E. French and Lockheed Aircraft Corp. Proceedings of the 1968 Aerodynamic Deceleration Systems Conference: *"The Initial Phase of Parachute Inflation"*. U.S. Air Force, El Centro, Calif. , USAF Report FTC-69-11, September 1968.

[12] D. L. Schilling and Lockheed Aircraft Corp: *"A Method for Determining Parachute Opening Shock Forces"*. LAC Report 12543, August 1957.

[13] H. F. Freeman and I. Rosenberg: *"High Altitude and High Airspeed Tests of Standard Parachute Canopies"*. U.S. Air Force, USAF Report AFFTC-TR-58-32, October 1958.

[14] W.B. Pepper and J.F. Reed: *"Parachute Study of Pressure Distribution in Wind Tunnel Testing"*. Journal of Aircraft, Vol. 10, No. 11, pp. 895-900, November 1976.

[15] Arnold AFB: "*Aerodynamic Characteristics of Disk-Gap-Band Parachutes in the Wake of Viking Entry Forebodies at Mach Numbers from* 0.2 *to* 2.6*",* AEDC-TR-72-78, Tennessee, 1972.

[16] R. Brendt: *"Supersonic Parachute Research"*. U.S. Air Force, USAF Report ASD-TR-66-236, July 1966.

[17] Barnhardt, Drayna, Nompelis, Candler, and Garrard: "*Detached Eddy Simulations of the MSL Parachute at Supersonic Conditions*", Proceedings of the 19th AIAA Aerodynamic Decelerator Systems Technology Conference, Williamsburg, Virginia, May 2007.

[18] Paul V. Tartabini and Brett R. Starr: *"Ares I-X Separation and Reentry Trajectrory Analyses"*. NASA Langley Research Center, Hampton, VA 23681, 2011.

[19] NASA's Constellation Programm: *"Ares I-X"*. Press kit, October 2009.

[20] Edgar G. Ewing: *"Ringsail Parachute Design"*. Northrop Corporation Ventura Division, Technical Report AFFDL-TR-72-3, pp. 57-58, January 1972.

[21] Daniel P. Raymer: *"Aircraft Design: A Conceptual Approach"*. Second Edition, AIAA, Sylmar, California 1992.

[22] NASA flight test: *"Ares I-X Launch Parachute Failure on Atlantic Ocean"*. Youtube https://www.youtube.com/watch?v=YSTuKzYuQ0Q, November 2009.

[23] Olivier L. de Weck, Sydney Do, Ricardo Robles, Joseph Pellicciotti, Tim Brady: *"An Airbag-Based Crew Impact Attenuation System for the Orion Crew Exploration Vehicle"*. AIAA 2009-6438, California, September 2009.

[24] Perry, J.A.: *"Critical Flow Through Sharp-Edged Orifices"* Transactions of the American Society of Mechanical Engineers, pp. 757-764, October 1949.

[25] M. Cooper, R. Sinclair, J. Sanders: *"Design and Testing of an Airbag Landing Attenuator System for a Generic Crew Return Vehicle"*. AIAA 2005-1616, 18th Aerodynamic Decelerator Systems Technology Conference and Seminar, 2005, Munich, Germany.